UNIVERSITY OF CALIFORNIA SAN DIEGO

Understanding the Importance of Hydride Transfer in Artificial Photosynthesis

A Dissertation submitted in partial satisfaction of the requirements
for the degree Doctor of Philosophy

in

Chemistry

by

Christopher James Miller

Committee in charge:

Professor Clifford P. Kubiak, Chair
Professor Guy Bertrand
Professor Andrew G. Dickson
Professor Francesco Paesani
Professor Jeffrey D. Rinehart

2022

The Dissertation of Christopher James Miller is approved, and it is acceptable in quality and form for publication on microfilm and electronically.

University of California San Diego

2022

DEDICATION

To my parents, Jim and Nancy.

EPIGRAPH

Taking on a challenge is a lot like riding a horse. If you're comfortable while you're doing it, you're probably doing it wrong

- Ted Lasso

TABLE OF CONTENTS

LIST OF FIGURES

LIST OF TABLES

ACKNOWLEDGEMENTS

First and foremost, I would like to thank my advisor Cliff Kubiak for all the support he has given me during my PhD. His leadership and mentorship not only made this work possible but allowed me to explore all my different interests which has led to my dissertation having three very different but connected projects. In addition, he allowed me the space I needed to both grow as a scientist and as a human and his support was invaluable during both the best and hardest times of my PhD.

Before I start down the path of thanking the other people who helped me do the work and helped me complete my PhD in one way or another, I want to thank the doctors and nurses all who helped me during my cancer in graduate school. Without Dr. Michael Kosty, Dr. Jordan Siegal, and Dr. Ramdev Konijeti and their teams and the wonderful nurses that helped, there would be no PhD to celebrate.

I would like to thank my lab mates at UCSD, both past and present. I have been able to work with so many great people who have made this possible. I want to thank some of the past members I did not overlap with but have had the luck to meet and have been helped by, specifically, Dr. Bhupi Kumar, Dr. Charles Machan, Dr. Jesse Froehlich, Dr. Gabe Canzi, and Dr. John Goeltz. I also want to thank past members who I was able to work with and was able to learn so much from, in particular Dr. Kate Waldie, Dr. Mark Reineke, Dr. Alissa Sasayama, Dr. Steven Chabolla, Dr. Tyler Porter, Dr. Alma Zhanaidarova, Dr. Andrew Ostericher, Gavin Heim, Jerry Zhai, Jeff Lampert, Kei Ito, Gwen Lee, Lu Yue Wang, Jonathan Sorbie, Anoushka Shandilya, and Jaden Lara. I also want to thank current members of the lab, Colin Loeb, Joe Palasz, Emily Smith, Nicole Torquato, Mori Taylor, and Lydia Weddle. Also, to Dr. Melissa

Helm, Dr. Felix Brunner, Dr. Daphne Cheung, Thomas Chan, Byunghoon Lee, Saya Okuno, and Dr. Jacob Barrett, I want to say a special thanks for how much of a difference you all have made in my PhD. Melissa for being a great mentor and giving me the start I needed in graduate school, Felix for always being the person I could go to talk science and problem solving with in lab, Daphne for teaching me all the secrets of organic synthesis and for always being there to bounce ideas off of, Thomas for being the wonderful (and maybe reluctant) replacement of Felix when he left, Saya for being a wonderful undergrad mentee, Byunghoon for being eager to learn and for taking up the work I started, and Jacob for being not only a close friend, but setting an example of what scientists can and should be beyond the lab environment.

I also want to thank the chemists that I have gotten to work with while at UCSD. Thank you to my committee, Drs. Bertrand, Dickson, Paesani, and Rinehart for their time and feedback on my research. It has been lovely to have you all on my committee. In addition, I could not have completed as much as I did without help from many people in different groups, from everyone on the 4th floor of Pac Hall, to the Bertrand Lab, to the Yang and Schimpf labs on the 6th floor, to Milan and Arnie in the crystallography lab to the biochemistry labs of the Muller and Zid as well as all the wonderful people I got to work with at EH&S while the area safety officer. I also want to thank my collaborators at Yale, Dr. Victor Batista, Ray Kelly, Jessica Freeze, and Benjamin Rudshteyn, for their computational work and Emory University, Dr. Tim Lian, Aimin Ge, Sarah Gebre, and Laura Keifer for their spectroscopy work and for all their fruitful discussions every week in our meetings together.

I want to thank my former group members from my undergraduate research in the Fisher lab at CSU and the Kemp lab at UNM. Specifically I want to thank Erin Stuckert for being an excellent graduate student mentor who allowed me to pursue my own work and learn new

techniques, Ellen Fisher being a great mentor and being a role model for how to not only be a good scientist but how to advocate for others in science, to Diane Dickie for preparing me not only for graduate school but also as a synthetic organometallic chemists, and Rick Kemp for being a leader, sharing his insights into chemistry, his belief in me, and his help along the way. I also want to thank Richard Finke at CSU as the professor who helped me solidify my feeling that I wanted to work in catalysis and for always reinforcing the rule of "if you want to learn how a reaction goes in one direction, it helps to study the reverse." I also want to thank the members of the Younger Chemists Committee past and present, and in particular Katie Johnson, Stephanie Ramos, Matt Grandbois, Natalie LaFranzo, and Christine Dunne, for being a group of wonderful chemists that I get to work with every year that allow to me travel and present at conferences as well as make a difference within a social setting of chemistry. I also want to thank the Senior Chemists Committee for having me a liaison and particularly Arlene Garrison for being my co-mentor and helping me in my career planning.

I want to thank my friends. First, I want to thank all my friends within chemistry I have not mentioned yet. I want to thank Dr. Michael L. Neville for being just across the hall ever since undergrad. You have done so much for me, the best I can sum it all up is by saying this: I do not know how I will survive my next job without you being a short walk away me so that I can talk to you about anything and everything. That is the thing I will miss the most from grad and undergrad. Thank you to Kerrick Rees for being my guy when it comes to any questions I have about organic chemistry or being there just to chat for 4 hours. I want to thank Ujwal Chadha for setting the standard extremely high on how to be an excellent co-worker during undergrad and being a great friend now. I want to thank Christian Seitz for being a chemist who I can always play soccer with or just go grab a bite to eat with. I want to thank Josh Arriola for

being a wonderful friend, someone who could drive me to chemo, a good soccer player, and a biochemist who has taught me most of the biochemistry that I know. I want to thank Dr. Anna Guzikowski for also being a wonderful friend and teaching me the rest of the biochemistry that I know. I want to thank Joseph Schiavini for supporting me as much as I probably supported him during undergrad chemistry classes, it has always been a pleasure to talk with you. To Dr. Frank Van Swol, thank you for having me part of your lunches with my dad over the years, it is one of the reasons that made me decide I wanted to be a chemist and not an engineer. To Dr. Debra Hunka, who always reminded me that sometimes recovery from cancer/surgeries and grad school are hard, but that even if when it was hard that I would always make it through.

I also want to thank my non-chemistry friends for their support throughout graduate school. To Paula, Henry, Na, Josh, Jacob, Sofie, Eric, Ian, and Dr. Katie, I have so many great memories of grad school with you all. I feel so lucky to have been able to have you all be so close (both figuratively and literally) in graduate school and I cannot wait to visit you all in Boston (or whatever city you end up in for Eric, Jacob, and Sofie) soon. To Dom Sanchez, here's to continuing our use of our free time to watch, play, and travel for soccer. To Cole Campbell, for being there for everything since we were just 3. To Josh North for being a friend and a future of living near each other again. To Nina Mascheroni for being who has always reminded me to be my best and to take time to enjoy art and music.

I also want to thank my family. I have been lucky to have a bunch of uncles, aunts, grandparents, and cousins and second cousins and great aunts and uncles and a whole list of family that have been there in the challenging times during my PhD and I cannot thank them enough. I want to specifically thank my twin brother, Jackson, who is also currently in a PhD

program at UNC Chapel Hill. He has been a rock throughout my life, and I cannot believe how lucky I am to have such a smart, thoughtful, kind, and caring brother.

I want to give a special thank you to Hayley Hirsh. I am incredibly lucky to have met and spent so much time with Hayley (and her two cats, Tonks and Toothless) during my PhD. She cheered me on, helped me through the challenging times, and was there for all the fun times in graduate school. I am very lucky to be marrying her. And I want to thank her parents, Sandy and Jay Hirsh, as well, as they have welcomed me into their family and have also been a big support during the last few years of my PhD.

Lastly, I want to thank my parents, Nancy Jackson and Jim Miller. I became a chemist because of my mom, as that is what she had studied in undergrad, but I focused my work on solar fuel and artificial photosynthesis as that is what I saw my dad do when I was growing up. It is not always easy to have parents that know your professors personally. It is not always easy to feel like you have certain expectations placed on you due to your family, but I would not change a thing. My parents gave me the confidence and the support I needed going into graduate school and they gave everything they could when I was there. They came to visit, they took me to chemo, they read some of my proposals and exam materials. They did all they could for as long as they could. To my mom, I love you, I miss you, rest in peace. And to my dad, I love you and I cannot wait to share where Arsenal, the Timbers, my research, and life goes with you.

Chapter 2, in full, is being prepared for submission for publication of the material entitled Miller, C.J.; Barrett, J.A.; Chan, T.; Shandilya, A.; Lee, B.; Kubiak, C.P. "A Reexamination of CO_2 Reduction with a Fe_2S_2 Hydrogenase Mimic: Unexpected Role of Mononuclear and Trinuclear Species," *Manuscript in Preparation.* The dissertation author is the primary author of this material. We acknowledge Dr. Michael Neville for invaluable

disccusions. This work is supported by the Air Force Office of Scientific Research under Award No. FA9550-17-0198.

Chapter 3, in full, is being prepared for submission for publication of the material entitled Miller, C.J.; Okuno, S.; Brunner, F.M.; Waldie, K.M.; Weddle, L.R.; Lee, B.; Kubiak, C.P. Hydricity as a Guide in H_2 Evolution, Formic Acid Decomposition, and Transfer Hydrogenation: A Case Study with Ir(Cp*)(2-phenylpyridine)H. The dissertation author was the primary researcher and author of this paper. We also acknowledge the Dr. Michael L. Neville and Joseph Palasz for invaluable discussion and the Kubiak group members for their feedback. This work is supported by the Air Force Office of Scientific Research under Award No. FA9550-17-0198.

Chapter 4, in full has been published in the material entitled, Miller, C.J.; Brunner, F.M.; Kelly, H.R.; Cheung, P.L.; Torquato, N. Gembicky, M.; Okuno, S.; Chan, T.; Bastista, V.S.; Kubiak, C.P. PM-IRRAS and DFT investigation of the surface orientation of new Ir piano-stool complexes attached to Au (111). *Dalton Trans.* Advanced Article. The dissertation author is the primary author of this material. We acknowledge Joseph Palasz, Sarah Tyler, Dr. Michael Neville, and Prof. Tianquan (Tim) Lian for invaluable discussions and the UCSD Molecular Mass Spectrometry Facility for HRMS sample analysis. This work was supported by the Air Force Office of Scientific Research under Award No. FA9550-17-0198. The authors acknowledge Dr. Ich Tran and the use of facilities and instrumentation at the UC Irvine Materials Research Institute (IMRI), which is supported in part by the National Science Foundation through the UC Irvine Materials Research Science and Engineering Center (DMR-2011967). XPS was performed using

instrumentation funded in part by the National Science Foundation Major Research Instrumentation Program under grant no. CHE-1338173.

VITA

2016 Bachelor of Science in Chemistry, Colorado State University

2018 Master of Science in Chemistry, University of California San Diego

2022 Doctor of Philosophy in Chemistry, University of California San Diego

PUBLICATIONS

Miller, C.J.; Okuno, S.; Waldie, K.M.; Brunner, F.M.; Kubiak, C.P. Hydricity as a guide in formate oxidation, H_2 generation, and transfer hydrogenation: A case study with of Ir(Cp*)(ppy)H. *Manuscript in prep.*

Miller, C.J.; Barrett, J.A.; Chan, T.; Shandilya, A.; Lee, B.; Kubiak, C.P. CO_2 Reduction with a Fe_2S_2 Hydrogenase Mimic: The Unexpected Role of Mononuclear Species. *Manuscript in prep*

Miller, C.J.; Brunner, F.M.; Kelly, H.R.; Cheung, P.L.; Torquato, N. Gembicky, M.; Okuno, S.; Chan, T.; Bastista, V.S.; Kubiak, C.P. PM-IRRAS and DFT investigation of the surface orientation of new Ir piano-stool complexes attached to Au (111). *Dalton Trans.* Advance Article

Barrett, J. A.; **Miller, C. J.;** Kubiak, C. P., Electrochemical Reduction of CO2 Using Group VII Metal Catalysts. *Trends in Chemistry* **2021**.

Barrett, J. A.; Brunner, F. M.; Cheung, P. L.; Kubiak, C. P.; Lee, G. L.; **Miller, C. J.;** Waldie, K. M.; Zhanaidarova, A., Chapter 1 Approaches to Controlling Homogeneous Electrochemical Reduction of Carbon Dioxide. In *Carbon Dioxide Electrochemistry: Homogeneous and Heterogeneous Catalysis*, The Royal Society of Chemistry: 2021; pp. 1-66.

Ge. A.; Rudshteyn, B.; Videla, P.E.; **Miller, C.J.**; Kubiak, C.P.; Batista, V.S.; Lian, T. Heterogenized Molecular Catalysts: Vibrational Sum-Frequency Spectroscopic, Electrochemical, and Theoretical Investigations. *Acc. Chem. Res.* **2019**, *52*, 1289-1300.

Zhanaidarova, A.; Ostericher A.L.; **Miller, C.J**.; Jones, S.C.; Kubiak, C.P. Selective Reduction of CO_2 to CO by a Molecular Re(ethynyl-bpy)$(CO)_3$Cl Catalyst and Attachment to Carbon Electrode Surfaces. *Organometallics.* **2019**, *38*1204-1207.

Clark, M.L.; Ge, A.; Videla, P.E.; Rudshteyn, B.; **Miller, C.J**.; Song, J.; Batista, V.S.; Lian, T.; Kubiak, C.P. CO_2 Reduction Catalysts on Gold Electrode Surfaces Influenced by Large Electric Fields. *J. Am. Chem. Soc.* **2018**, *140*, 17643-17655.

ABSTRACT OF THE DISSERTATION

Understanding the Importance of Hydride Transfer in Artificial Photosynthesis

by

Christopher James Miller

Doctor of Philosophy in Chemistry

University of California San Diego, 2022

Professor Clifford P. Kubiak, Chair

Our dependence on the burning of fossil fuels for energy, leading to the rise in global temperatures and climate change, has sparked increased research into the utilization of carbon dioxide (CO_2) as a renewable starting material for the synthesis of new fuel sources.

Heterogenous catalysts are often employed for these reactions as they tend to have higher stability, activity, lower catalyst loadings, and scalability. However, selective heterogenous catalyst discovery is often hindered by the lack of understanding and often relies on high-throughput screening. In contrast, homogeneous catalysts have active sites that are well understood, are highly tunable, uniform, and thus selective. By using homogeneous catalyst, fundamental understanding of the elementary steps involved in product selectivity can be achieved, allowing for improved catalyst design.

The conversion of CO_2 to value-added carbon products for fuel requires multi-electron and proton steps. One elementary step that can lower the entropic barrier of this process is the transfer of a hydride from a metal catalyst to CO_2 to yield formate (HCO_2^-), the two-electron reduction product. The investigation of the structural, thermodynamic, and kinetic barriers that allow this transformation is the first step in designing novel, selective catalytic systems.

The metal-metal cooperativity in [FeFe] hydrogenase mimics, which allows for the formation of highly reducing hydrides from weak acids, has been hypothesized as a key step in the electrochemical reduction of CO_2 to formate. However, there were little mechanistic and structural insights that lead to the selectivity for formate in these systems. Briefly, using the [FeFe] hydrogenase mimic [Fe_2(μ-pdt)$(CO)_6$, where pdt = propane-1,3-dithiolate] as the precatalyst, it was found that the main product formed under catalytic conditions, was H_2 (FE_{max}= 56 ±4%), with CO (FE_{max}= 16 ±6%) and HCO_2^- (FE_{max}= 20%) being minor products. Interestingly, it was determined that the formation of HCO_2^- was potential dependent, with the Faradaic efficiency increasing from 2.4% to 20% upon the third reduction of the catalyst. In addition, in the absence of a proton source, CO_2 underwent disproportionation to CO and CO_3^{2-}. Finally, by combining experimental and computational methods, it was determined that the

selectivity of the catalytic system was hindered due to the formation of multiple compounds, with mononuclear $[Fe(CO)_4]^{2-}$ and a trinuclear Fe likely playing active roles in catalysis.

The thermodynamic ability of a substrate to donate a hydride, known as hydricity, is an important parameter for predicting the reactivity of a catalyst in artificial photosynthetic systems. Tools that allow us to measure the hydride donor ability are critical not only to predicting reactivity but can be used to understand and optimize catalytic systems with a metal hydride of choice. Using Ir(Cp*)(ppy)X (where X is H or Cl), hydrogen evolution, formic acid decomposition, and transfer hydrogenation are optimized and understood using hydricity and thermodynamics as a guide.

Finally, immobilization of homogeneous catalysts onto surfaces, allows for insight into the mechanisms that affect heterogenous electrochemistry. Previous studies showed that the electric field effects on the $Re(bpy\text{-}X)(CO)_3Cl$ bound to Au surfaces changed the electron density at the metal. These field effects, as seen in the $\nu(CO)$ frequency shift of greater than 25 cm^{-1}, is three to four times larger than those achieved through synthetic efforts of modifying the bipyridine for electron donating or accepting groups via Hammett parameters. Additionally, hydricity is highly dependent on the electronic properties of the substrate. Computational results show that electric fields stabilize the transfer of a hydride from Ir(Cp*)(bpy)H, making Ir a better hydride donor. Two new Ir catalysts with surface-immobilizable disulfides were synthesized for attachment to Au. However, reactivity studies showed that the rate of simple ligand separation was significantly slower. Combined DFT and surface sensitive spectroscopic studies showed that the monolayers formed from these complexes are a mix of molecular orientations, likely leading to a range of reaction rates on the surface.

CHAPTER 1. Artificial Photosynthesis: Challenges and Mechanistic Insights

1.1 Introduction

Over the past 100 years, all descriptors that define quality of life, from life expectancy to literacy, to incomes, have improved.[1] The driving force behind this movement was the Industrial Revolution and, in particular, the development and use of fossil fuels as primary energy sources.[2] The development of large-scale industry, transportation, and efficient production of materials have all been buoyed by the refinement and use of the energy-dense hydrocarbons found in crude oil.[3] In addition to our fuels, crude oil is a main source for many of our other commonly used chemicals, being a major feedstock for our plastics and medicines.[4] However, the ubiquitous use of fossil fuels has a price.

First, the distribution of fossil fuels is not equal over the world. Instead, it is concentrated in a few places. This unequal distribution, in addition to our reliance on it, has led to large scale geo-political conflicts, such as the current war in Ukraine.[5-6] Furthermore, the continued use of fossil fuels has led to the ever-increasing amounts of atmospheric carbon dioxide (CO_2).[7] The concentration of CO_2 in the atmosphere has remained above 400 ppm since August 2016,[8] which is almost double the average concentration of the past 10,000 years (Figure 1.1).[7] The continual rise has also led to 45 consecutive years of global average temperatures above the 20th century average.[9] Without immediate change, the predicted concentration of atmospheric CO_2 is predicted to reach 800 ppm by the year 2100, coinciding with a 4° C increasing in the average global

temperature.[10] This increase in temperature will have catastrophic impacts to life on earth. Therefore, the search for clean, alternative, and renewable fuels is critical.

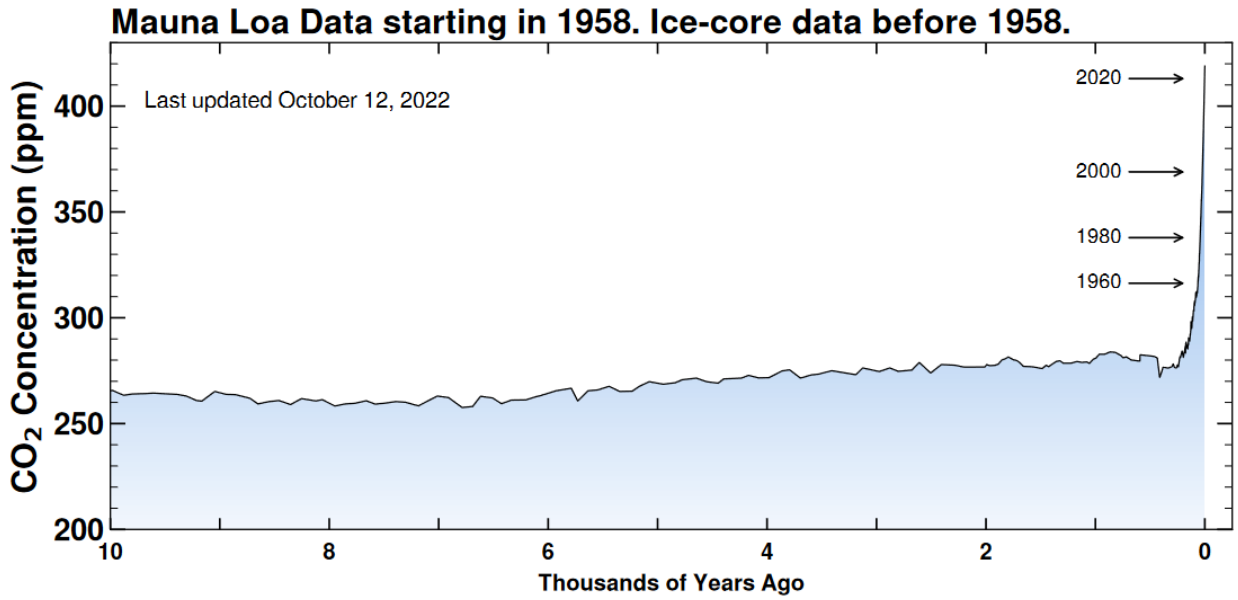

Figure 1.1. The atmospheric CO_2 concentrations for the last 10,000 years. Reproduced in full, with permission from reference 8.

While fossil fuels currently make up about 78.5% of the share of total energy consumption,[11] that share has been decreasing as the implementation of a range of different renewable energy sources have become more economically viable. In California, the share of energy coming from solar panels and wind farms has been increasing steadily.[12] However, the intermittent nature of these combined with high percentages of installed renewable capacity has led to over-production in the day followed by a sharp increase in capacity needed at the end of the day.[13] This phenomenon, named the "duck curve" after the shape of the graph it produces, leads to negative electricity prices or shut down of the capacity during solar production peak hours.[13]

To address the problem of overproduction, there have been increased interest in storage capacity. While the current method for energy storage is pumped hydro, the process of using the cheap energy to pump water uphill and letting it fall and turn turbines to release the energy when

needed, it has limited scalability and requires specific geographic conditions.[14] Additionally, the implementation of large-scale batteries for grid storage has been one of the most readily available methods to combat energy demand.[15] However, batteries have several drawbacks. Their chemical stability and the time scale of their charge and discharging make them ideal for short-term storage, making them currently unable to compensate for seasonal fluctuations.[16-17] Additionally, their energy density is fundamentally limited and pale in comparison to liquid fuels.[4, 18] For this reason, the access to cheap, renewable energy has opened the door to the use of electrochemical

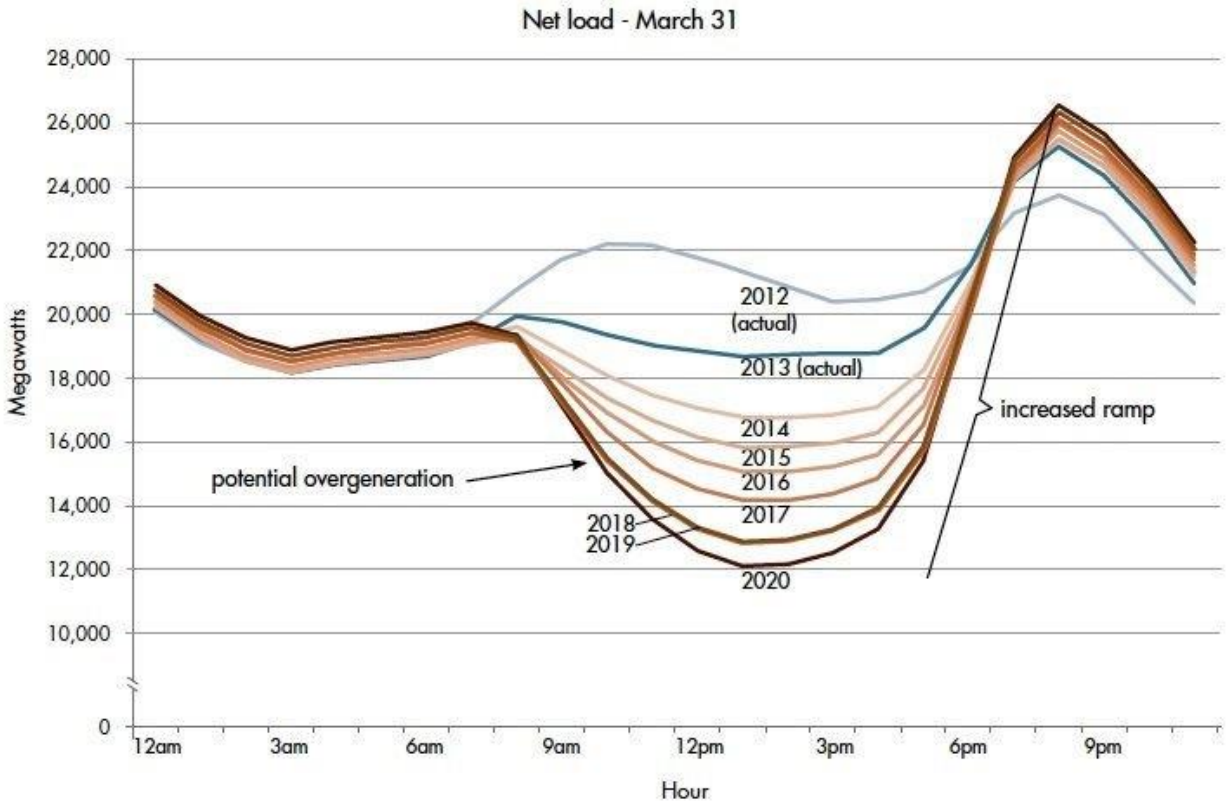

Figure 1.2. The "duck curve" showing the net load, in MW, equal to the normal load minus the energy generated via wind farms and photovoltaics. Reproduced in full, from reference 13.

transformations for the storage of energy in liquid fuels.[19] A reaction that has sustained a continued interest of research is the electrochemical utilization of CO_2 for liquid fuel production.[20-23]

1.2 Artificial Photosynthetic Catalysts

The conversion of CO_2 into liquid fuels, also known as artificial photosynthesis, has been a challenge for chemists for over 100 years.[24] The first reports of the electrocatalytic conversion, or reduction, of CO_2 into higher-value products appeared in the 1900s.[25-26] Thermodynamically, the reduction of CO_2 into value added products is an uphill, energy consuming reaction.[27] Due to the strong bonds and the need for multiple equivalents of protons and electrons, the reduction of CO_2 requires a catalyst. These barriers can be lowered and overcome by multistep pathways that couple protons and electrons to generate value added products such as formic acid, methanol, ethane, and even ethanol.[20, 28] Yet, these reactions have their own drawbacks and succumb to the kinetic difficulties of coupling multiple protons and electrons. Therefore, studies to optimize these systems have focused on catalysts and their mechanisms of operation.

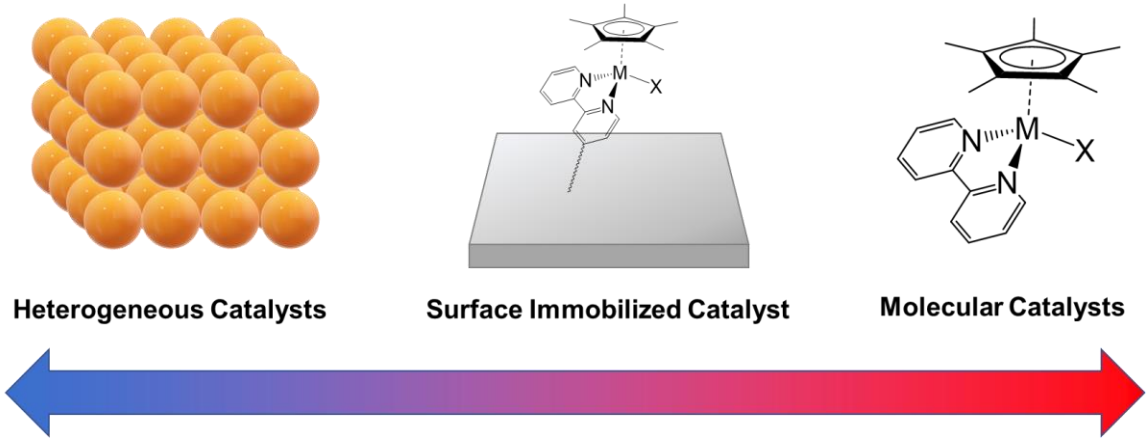

Figure 1.3. The type of catalyst used in artificial photosynthetic systems.

The catalysts studied in artificial photosynthetic systems have been molecular (or homogeneous), heterogeneous, and a combination of the two, immobilized catalysts.[20-21, 29-30] Heterogeneous catalysts, generally consisting of extended solid and metal electrodes, have been of particular interest due to their stability, ease of separation of products, and their range of active

sites and reactivities allowing for facile implementation into CO_2 electrolyzers.[31] In addition, the stability of these catalysts allows for implementation in a range of electrochemical environments, with particular interest on the use of aqueous environments.[31]

Current interest in heterogeneous reduction of CO_2 has focused on using Cu electrodes in various aqueous environments due to the ability of the surface to couple C-C bonds and transfer protons and electrons to catalytically relevant intermediates, allowing for the formation of C2+

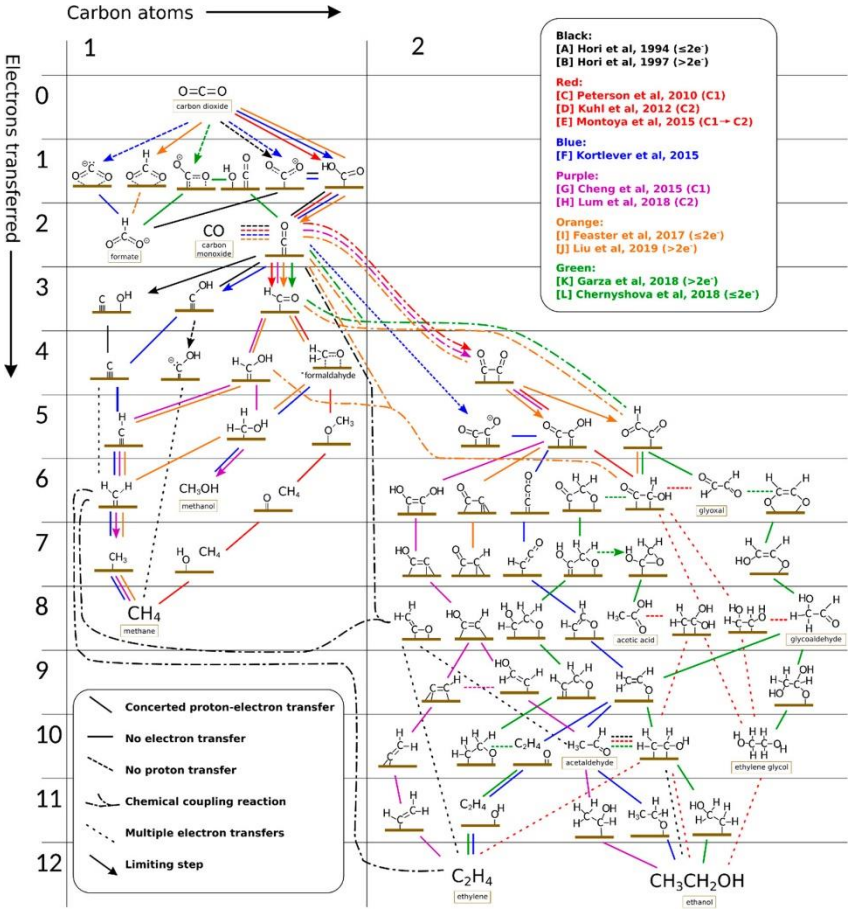

Figure 1.4. Proposed mechanistic pathways for the reduction of CO_2 on polycrystalline copper electrodes. Reproduced in full, with the permission of 20.

products.[20, 31] By combining electrochemical, spectroscopic, and computational techniques, several mechanisms have been proposed for this process (Figure 1.4).[20] However, while several potential pathways have been proposed, the mechanisms that lead to these pathways are experimentally difficult to determine. Therefore, selective heterogeneous catalyst discovery is

hindered by this lack of understanding and often relies on high-throughput screening.[32] Therefore, to gain an understanding of the microenvironment and mechanisms at play in artificial photosynthesis, chemists have also relied on molecular catalysts as a proxy.

Molecular electrocatalysts are small molecules, generally inorganic or organometallic compounds, that participate in the electron transfer (at an electrode) and accelerate the rate of reaction for the conversion of CO_2 to products.[33] These catalysts both supply charge and perform inner sphere chemical reduction of the kinetically stable substrate. Additionally, the redox potential of these electrocatalysts should match the thermodynamic potential needed to perform these transformations.[34] A particular advantage to molecular catalysts is the degree to which these parameters can be controlled through the optimization of the ligand, metal of choice, and electronic configuration.[35] This degree of control has led to a high degree of understanding of artificial photosynthetic systems.

1.3 Learning from Molecular Catalysts for CO_2 Conversion

The first molecular electrocatalysts for the reduction of CO_2 were reported in the 1970s and 1980s. These reports included metal phthalocyanine,[36-37] metal tetraaza-macrocycles,[38-39] late transition metal phosphine,[40] and Re bipyridyl carbonyl complexes.[41] Since these initial reports, the field has identified new dimensions for the optimization of these systems, including solvent, electrolyte, and applied bias.[21] However, due to the kinetic challenges of multiple electron and proton steps required to convert CO_2 to products such as methanol, molecular catalysts in artificial photosynthetic systems convert CO_2 into the more kinetically viable two-electron reduction products, CO and formic acid.[21]

Both reduction products represent not only economically interesting targets, but crucial artificial photosynthetic intermediates. First, the production of clean, renewable CO allows for

direct implementation of in Fischer-Tropsch technology, allowing for conversion to liquid fuels.[42] Additionally, CO is a key intermediate in the electrochemical reduction of CO_2 to higher order products, particularly on Cu electrodes.[20, 31] Consequentially, formic acid and its conjugate base, formate, is a catalytic dead end in the electrochemical reduction of CO_2 on heterogeneous electrodes.[20] However, formic acid itself is of interest because of its use in fuel cells,[32] use as a hydrogen storage carrier,[43-44] or implementation in tandem catalysis as a pathway to form more reduced fuels.[45-46]

1.4 Mechanistic Insights

While the aim of this thesis is to understand the mechanisms responsible for hydride transfer in artificial photosynthetic systems, it is important to also understand the mechanistic insights that lead to the formation of the other reduction product, CO. Importantly, the two products are formed via two distinct mechanistic pathways (Figure 1.5). Where formate is made via the initial protonation of the active site followed by direct transfer of a hydride to CO_2, reduction to CO requires the direct addition of CO_2 to the active site followed either by subsequent protonation of the adduct to form a hydroxycarbonyl,[47-49] follow by subsequent protonation and reduction for form CO and H_2O or by deoxygenation of the reduced CO_2 intermediate in multi-metallic[50-52] or Lewis acid assisted pathway.[53-55] to produce CO and CO_3^{2-}. Due to this, the active site and microenvironment play a critical role in product selectivity.

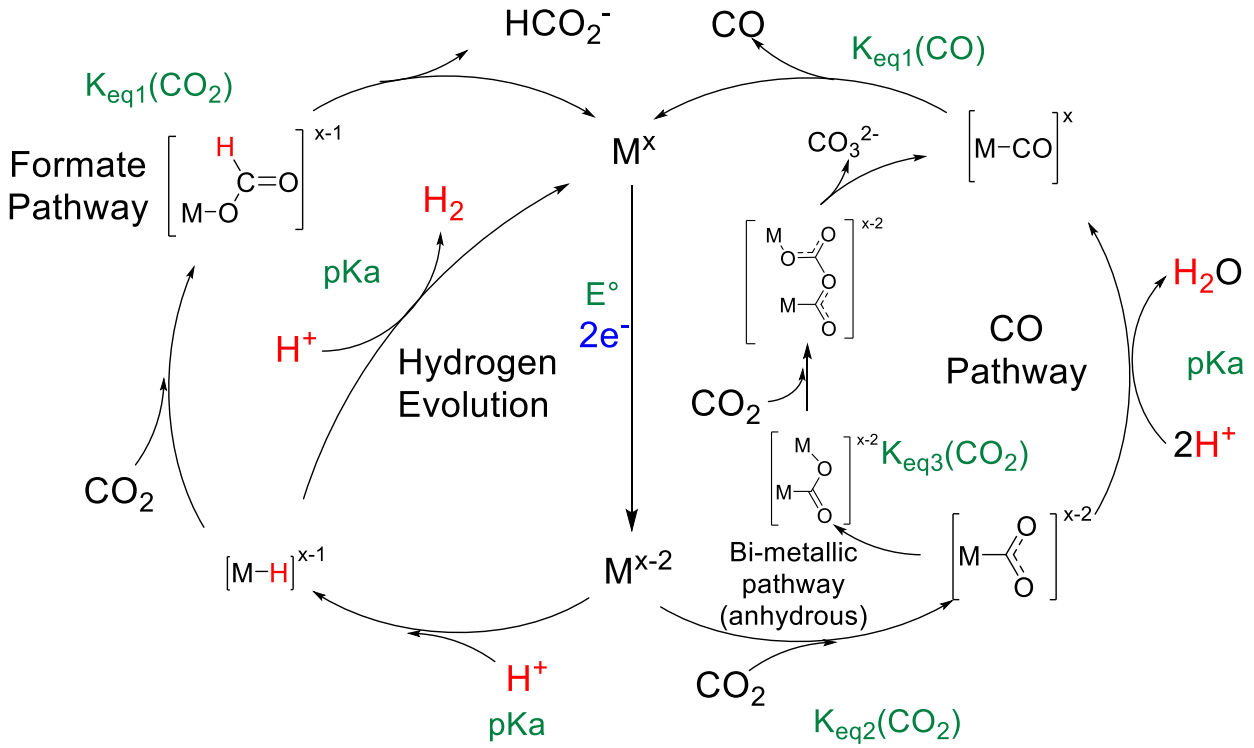

Figure 1.5. The possible mechanistic pathways for the two-electron reduction products of CO_2 or hydrogen evolution at a single metal active site.

First, the metal center and ligand architecture play a huge role in the selectivity of CO_2 reduction.[21] As stated previously, the redox potential of these electrocatalysts must match the thermodynamics the chemical potential needed to perform CO_2 reduction. Practically, this results in the vast majority of the molecular electrocatalysts being late-transition (Group 6 or later) metal inorganic or organometallic complexes with stable, low oxidation states[21]. Additionally, the use of σ-donating ligands, such as imines, amines, and phosphines, play a crucial role in allowing for the increased electron density on the metal center.[21] Furthermore, π-accepting carbonyl ligands or redox active bipyridines, porphyrins, or other aromatic ligands are commonly used to stabilize low oxidation state metal centers.[21] The combination of metal center and ligands allows for the fine tuning of the molecular orbitals involved in reduction of CO_2. Importantly, the formation of a metal

hydride requires the electron density to be localized in the d_{z2} orbital, whereas selective CO_2 binding can be achieved by the involvement of both σ and π interactions in the active site.[56-58]

Second, the optimization of the microenvironment around the catalytic active site, including the solvent, proton source, and electrolyte, play a crucial role the product selectivity.[21] Thus, the strength of the proton source in the selected medium for catalysis is consequential. For the formate pathway, the proton source must be strong enough to protonate the reduced metal center.[59] The second step requires the insertion of CO_2 into the metal hydride bond. However, this tends to be the slow step in the catalysis.[49, 59-60] Consequently, if the proton source is too strong, the kinetics of CO_2 insertion will be beat out by the protonation of the hydride to form H_2.[59, 61] However, if the proton source is too weak, it will not protonate the metal center, leading to the catalyst going down the CO pathway.[56, 62] Specifically, for the CO and H_2O pathway, the second step requires the strength of the acid to be strong enough not only to protonate the adduct to form a hydroxycarbonyl, but to further provide another proton to form water and a carbonyl. Too weak of an acid to protonate the intermediates and the catalyst must proceed down the entropically less favored bi-metallic pathway.[63]

Chapter 2 discusses these effects in detail, discussing how the microenvironment and multiple catalysts formed upon the reduction of a hydrogenase mimic lead to an array of reduction products. In addition, it discusses how the combination of spectroscopy, electrochemistry, and density functional theory are used to narrow down the specific compounds that are likely intermediates in the catalytic cycle.

Chapter 3 focuses on understanding the formate pathway, in this case, by using the reverse reaction (formic acid decomposition), and transfer hydrogenation to understand the kinetics, thermodynamics, and role of metal hydrides in artificial photosynthetic systems. This work is

specifically aimed at understanding how the thermodynamic ability of a substrate to transfer a hydride, known as hydricity, can be used to understand the energetics of different steps of the catalytic cycle and can be applied to new systems such as transfer hydrogenation.

Finally, Chapter 4 discusses how the immobilization of well-understood molecular catalysts on conducting surfaces provides insight into the microenvironment at heterogenous surfaces. Specifically, by the combination of synthetic technique, surface sensitive spectroscopy, and computational chemistry, a descriptive picture of the surface can be made. From this, future reactivity is speculated, with addition insights into other immobilized systems.

1.5 References

1. Riley, J. C., Estimates of Regional and Global Life Expectancy, 1800–2001. *Population and Development Review* **2005,** *31* (3), 537-543.

2. Wrigley, E. A., Energy and the English Industrial Revolution. *Philosophical Transactions of the Royal Society A: Mathematical, Physical and Engineering Sciences* **2013,** *371* (1986), 20110568.

3. Del Rio, M.; Hargrove, W. L.; Tomaka, J.; Korc, M., Transportation Matters: A Health Impact Assessment in Rural New Mexico. *International Journal of Environmental Research and Public Health* **2017,** *14* (6), 629.

4. De Luna, P.; Hahn, C.; Higgins, D.; Jaffer, S. A.; Jaramillo, T. F.; Sargent, E. H., What would it take for renewably powered electrosynthesis to displace petrochemical processes? *Science* **2019,** *364* (6438), eaav3506.

5. Su, C. W.; Qin, M.; Tao, R.; Moldovan, N. C., Is Oil Political? From the Perspective of Geopolitical Risk. *Defence and Peace Economics* **2021,** *32* (4), 451-467.

6. Froese, R.; Schilling, J., The Nexus of Climate Change, Land Use, and Conflicts. *Current Climate Change Reports* **2019,** *5* (1), 24-35.

7. Lüthi, D.; Le Floch, M.; Bereiter, B.; Blunier, T.; Barnola, J.-M.; Siegenthaler, U.; Raynaud, D.; Jouzel, J.; Fischer, H.; Kawamura, K.; Stocker, T. F., High-resolution carbon dioxide concentration record 650,000–800,000 years before present. *Nature* **2008,** *453* (7193), 379-382.

8. Keeling, R. F.; Keeling, C. D., Atmospheric Monthly In Situ CO2 Data - Mauna Loa Observatory, Hawaii In *In Scripps CO2 Program Data.*, UC San Diego Library Digital Collections., 2017.

9. Information, N. N. C. f. E. *State of the Climate: Monthly Global Climate Report for Annual 2021*; 2022.

10. Cheng, W.; Dan, L.; Deng, X.; Feng, J.; Wang, Y.; Peng, J.; Tian, J.; Qi, W.; Liu, Z.; Zheng, X.; Zhou, D.; Jiang, S.; Zhao, H.; Wang, X., Global monthly gridded atmospheric carbon dioxide concentrations under the historical and future scenarios. *Scientific Data* **2022,** *9* (1), 83.

11. *Renewables 2022 Global Status Report (GSR)*.

12. Ybarra;, C. E.; Broughton;, J. B.; Nyer;, P. U., Trends in the Installation of Residential Solar Panelsin California. *Low Carbon Economy* **2021,** *12*, 63-72.

13. Denholm, P.; O'Connell, M.; Brinkman, G.; Jorgenson, J. *Overgeneration from Solar Energy in California. A Field Guide to the Duck Chart*; United States, 2015-11-01, 2015.

14. Ali, S.; Stewart, R. A.; Sahin, O., Drivers and barriers to the deployment of pumped hydro energy storage applications: Systematic literature review. *Cleaner Engineering and Technology* **2021,** *5*, 100281.

15. Hirsh, H. S.; Li, Y.; Tan, D. H. S.; Zhang, M.; Zhao, E.; Meng, Y. S., Sodium-Ion Batteries Paving the Way for Grid Energy Storage. *Adv. Energy Mater.* **2020,** *10* (32), 2001274.

16. Schmidt, O.; Melchior, S.; Hawkes, A.; Staffell, I., Projecting the Future Levelized Cost of Electricity Storage Technologies. *Joule* **2019,** *3* (1), 81-100.

17. Denholm, P.; Mai, T., Timescales of energy storage needed for reducing renewable energy curtailment. *Renewable Energy* **2019,** *130*, 388-399.

18. Dijkman, T. J.; Benders, R. M. J., Comparison of renewable fuels based on their land use using energy densities. *Renewable and Sustainable Energy Reviews* **2010,** *14* (9), 3148-3155.

19. Lewis, N. S., Research opportunities to advance solar energy utilization. *Science* **2016,** *351* (6271), aad1920.

20. Nitopi, S.; Bertheussen, E.; Scott, S. B.; Liu, X.; Engstfeld, A. K.; Horch, S.; Seger, B.; Stephens, I. E. L.; Chan, K.; Hahn, C.; Nørskov, J. K.; Jaramillo, T. F.; Chorkendorff, I., Progress and Perspectives of Electrochemical CO2 Reduction on Copper in Aqueous Electrolyte. *Chem. Rev.* **2019,** *119* (12), 7610-7672.

21. Barrett, A. J. A.; Brunner, B. F. M.; Cheung, C. P. L.; Kubiak, D. C. P.; Lee, E. G. L.; Miller, F. C. J.; Waldie, G. K. M.; Zhanaidarova, H. A., Chapter 1 Approaches to Controlling Homogeneous Electrochemical Reduction of Carbon Dioxide. In *Carbon Dioxide Electrochemistry: Homogeneous and Heterogeneous Catalysis*, The Royal Society of Chemistry: 2021; pp 1-66.

22. Barrett, J. A.; Miller, C. J.; Kubiak, C. P., Electrochemical Reduction of CO₂ Using Group VII Metal Catalysts. *Trends in Chemistry* **2021,** *3* (3), 176-187.

23. Deronzier, A.; Chardon-Noblat, S., Electrocatalytic reduction of carbon dioxide: a future solution for sustainable chemistry? *Actual. Chim.* **2013,** *371-372*, 84-88.

24. Rakowski Dubois, M.; Dubois, D. L., Development of Molecular Electrocatalysts for CO2 Reduction and H2 Production/Oxidation. *Acc. Chem. Res.* **2009,** *42* (12), 1974-1982.

25. Coehn, A.; Jahn, S., Electrolytic reduction of carbon dioxide. *Berichte der Deutschen Chemischen Gesellschaft* **1904,** *37*, 2836.

26. Fischer, F.; Prziza, O., Über die elektrolytische Reduktion von unter Druck gelöstem Kohlendioxyd und Kohlenoxyd. *Berichte der deutschen chemischen Gesellschaft* **1914,** *47* (1), 256-260.

27. Kumar, B.; Llorente, M.; Froehlich, J.; Dang, T.; Sathrum, A.; Kubiak, C. P., Photochemical and Photoelectrochemical Reduction of CO_2. *Annu. Rev. Phys. Chem.* **2012**.

28. Benson, E. E.; Kubiak, C. P.; Sathrum, A. J.; Smieja, J. M., Electrocatalytic and homogeneous approaches to conversion of CO2 to liquid fuels. *Chem. Soc. Rev.* **2009,** *38* (1), 89-99.

29. Appel, A. M.; Bercaw, J. E.; Bocarsly, A. B.; Dobbek, H.; DuBois, D. L.; Dupuis, M.; Ferry, J. G.; Fujita, E.; Hille, R.; Kenis, P. J. A.; Kerfeld, C. A.; Morris, R. H.; Peden, C. H. F.; Portis, A. R.; Ragsdale, S. W.; Rauchfuss, T. B.; Reek, J. N. H.; Seefeldt, L. C.; Thauer, R. K.; Waldrop, G. L., Frontiers, Opportunities, and Challenges in Biochemical and Chemical Catalysis of CO2 Fixation. *Chem. Rev. (Washington, DC, U. S.)* **2013,** *113* (8), 6621-6658.

30. Bullock, R. M.; Das, A. K.; Appel, A. M., Surface Immobilization of Molecular Electrocatalysts for Energy Conversion. *Chem. Eur. J.* **2017,** *23* (32), 7626-7641.

31. Clark, E. L.; Bell, A. T., Chapter 3 Heterogeneous Electrochemical CO2 Reduction. In *Carbon Dioxide Electrochemistry: Homogeneous and Heterogeneous Catalysis*, The Royal Society of Chemistry: 2021; pp 98-150.

32. An, L.; Chen, R., Direct formate fuel cells: A review. *J. Power Sources* **2016,** *320*, 127-139.

33. Costentin, C.; Saveant, J.-M., Multielectron, multistep molecular catalysis of electrochemical reactions. Benchmarking of homogeneous catalysts. *ChemElectroChem* **2014,** *1* (7), 1226-1236.

34. Schneider, J.; Jia, H.; Muckerman, J. T.; Fujita, E., Thermodynamics and kinetics of CO2, CO, and H+ binding to the metal center of CO2 reduction catalysts. *Chem. Soc. Rev.* **2012,** *41* (6), 2036-2051.

35. DuBois, D. L., Development of Molecular Electrocatalysts for Energy Storage. *Inorg. Chem.* **2014,** *53* (8), 3935-3960.

36. Meshitsuka, S.; Ichikawa, M.; Tamaru, K., Electrocatalysis by metal phthalocyanines in the reduction of carbon dioxide. *J. Chem. Soc., Chem. Commun.* **1974,** (5), 158-9.

37. Kazuya, H.; Katsuhiro, T.; Hideo, S.; Shinobu, T., ELECTROCATALYTIC BEHAVIOR OF TETRASULFONATED METAL PHTHALOCYANINES IN THE REDUCTION OF CARBON DIOXIDE. *Chem. Lett.* **1977,** *6* (10), 1137-1140.

38. Fisher, B. J.; Eisenberg, R., Electrocatalytic reduction of carbon dioxide by using macrocycles of nickel and cobalt. *J. Am. Chem. Soc.* **1980,** *102* (24), 7361-3.

39. Beley, M.; Collin, J. P.; Ruppert, R.; Sauvage, J. P., Nickel(II)-cyclam: an extremely selective electrocatalyst for reduction of carbon dioxide in water. *J. Chem. Soc., Chem. Commun.* **1984,** (19), 1315-16.

40. Slater, S.; Wagenknecht, J. H., Electrochemical reduction of carbon dioxide catalyzed by Rh(diphos)2Cl. *J. Am. Chem. Soc.* **1984,** *106* (18), 5367-8.

41. Hawecker, J.; Lehn, J. M.; Ziessel, R., Electrocatalytic reduction of carbon dioxide mediated by Re(bipy)(CO)3Cl (bipy = 2,2'-bipyridine). *J. Chem. Soc., Chem. Commun.* **1984,** (6), 328-30.

42. Jahangiri, H.; Bennett, J.; Mahjoubi, P.; Wilson, K.; Gu, S., A review of advanced catalyst development for Fischer–Tropsch synthesis of hydrocarbons from biomass derived syn-gas. *Catalysis Science & Technology* **2014,** *4* (8), 2210-2229.

43. Waldie, K. M.; Brunner, F. M.; Kubiak, C. P., Transition Metal Hydride Catalysts for Sustainable Interconversion of CO2 and Formate: Thermodynamic and Mechanistic Considerations. *ACS Sustainable Chemistry & Engineering* **2018,** *6* (5), 6841-6848.

44. Wang, D.; Astruc, D., The Golden Age of Transfer Hydrogenation. *Chem. Rev.* **2015,** *115* (13), 6621-6686.

45. Chu, W.-Y.; Culakova, Z.; Wang, B. T.; Goldberg, K. I., Acid-Assisted Hydrogenation of CO2 to Methanol in a Homogeneous Catalytic Cascade System. *ACS Catal.* **2019,** *9* (10), 9317-9326.

46. Miller, A. J. M.; Heinekey, D. M.; Mayer, J. M.; Goldberg, K. I., Catalytic Disproportionation of Formic Acid to Generate Methanol. *Angew. Chem. Int. Ed.* **2013,** *52* (14), 3981-3984.

47. Machan, C. W.; Sampson, M. D.; Kubiak, C. P., A Molecular Ruthenium Electrocatalyst for the Reduction of Carbon Dioxide to CO and Formate. *J. Am. Chem. Soc.* **2015,** *137* (26), 8564-8571.

48. Barlow, J. M.; Yang, J. Y., Thermodynamic Considerations for Optimizing Selective CO2 Reduction by Molecular Catalysts. *ACS Central Science* **2019,** *5* (4), 580-588.

49. Ceballos, B. M.; Yang, J. Y., Highly Selective Electrocatalytic CO2 Reduction by [Pt(dmpe)2]2+ through Kinetic and Thermodynamic Control. *Organometallics* **2020,** *39* (9), 1491-1496.

50. Dubois, M. R.; Dubois, D. L., Development of Molecular Electrocatalysts for CO2 Reduction and H-2 Production/Oxidation. *Acc. Chem. Res.* **2009,** *42* (12), 1974-1982.

51. Jeoung, J.-H.; Dobbek, H., Carbon Dioxide Activation at the Ni,Fe-Cluster of Anaerobic Carbon Monoxide Dehydrogenase. *Science* **2007,** *318* (5855), 1461-1464.

52. Raebiger, J. W.; Turner, J. W.; Noll, B. C.; Curtis, C. J.; Miedaner, A.; Cox, B.; DuBois, D. L., Electrochemical Reduction of CO2 to CO Catalyzed by a Bimetallic Palladium Complex. *Organometallics* **2006,** *25* (14), 3345-3351.

53. Sampson, M. D.; Kubiak, C. P., Manganese Electrocatalysts with Bulky Bipyridine Ligands: Utilizing Lewis Acids To Promote Carbon Dioxide Reduction at Low Overpotentials. *J. Am. Chem. Soc.* **2016,** *138* (4), 1386-1393.

54. Hammouche, M.; Lexa, D.; Momenteau, M.; Saveant, J. M., Chemical catalysis of electrochemical reactions. Homogeneous catalysis of the electrochemical reduction of carbon dioxide by iron("0") porphyrins. Role of the addition of magnesium cations. *J. Am. Chem. Soc.* **1991,** *113* (22), 8455-66.

55. Zhanaidarova, A.; Steger, H.; Reineke, M. H.; Kubiak, C. P., Chelated [Zn(cyclam)]2+ Lewis acid improves the reactivity of the electrochemical reduction of CO2 by Mn catalysts with bulky bipyridine ligands. *Dalton Trans.* **2017,** *46* (37), 12413-12416.

56. Riplinger, C.; Carter, E. A., Influence of Weak Bronsted Acids on Electrocatalytic CO2 Reduction by Manganese and Rhenium Bipyridine Catalysts. *ACS Catal.* **2015,** *5* (2), 900-908.

57. Riplinger, C.; Sampson, M. D.; Ritzmann, A. M.; Kubiak, C. P.; Carter, E. A., Mechanistic Contrasts between Manganese and Rhenium Bipyridine Electrocatalysts for the Reduction of Carbon Dioxide. *J. Am. Chem. Soc.* **2014,** *136* (46), 16285-16298.

58. Azcarate, I.; Costentin, C.; Robert, M.; Saveant, J.-M., Through-Space Charge Interaction Substituent Effects in Molecular Catalysis Leading to the Design of the Most Efficient Catalyst of CO2-to-CO Electrochemical Conversion. *J. Am. Chem. Soc.* **2016,** *138* (51), 16639-16644.

59. Waldie, K. M.; Ostericher, A. L.; Reineke, M. H.; Sasayama, A. F.; Kubiak, C. P., Hydricity of Transition-Metal Hydrides: Thermodynamic Considerations for CO2 Reduction. *ACS Catal.* **2018,** *8* (2), 1313-1324.

60. Yang, J. Y.; Kerr, T. A.; Wang, X. S.; Barlow, J. M., Reducing CO2 to HCO2– at Mild Potentials: Lessons from Formate Dehydrogenase. *J. Am. Chem. Soc.* **2020,** *142* (46), 19438-19445.

61. Ostericher, A. L.; Porter, T. M.; Reineke, M. H.; Kubiak, C. P., Thermodynamic targeting of electrocatalytic CO2 reduction: advantages, limitations, and insights for catalyst design. *Dalton Trans.* **2019,** *48* (42), 15841-15848.

62. Clark, M. L.; Cheung, P. L.; Lessio, M.; Carter, E. A.; Kubiak, C. P., Kinetic and mechanistic effects of bipyridine (bpy) substituent, labile ligand, and Bronsted acid on electrocatalytic CO2 reduction by Re(bpy) complexes. *ACS Catal.* **2018,** *8*, 2021-2029.

63. Machan, C. W.; Chabolla, S. A.; Kubiak, C. P., Reductive Disproportionation of Carbon Dioxide by an Alkyl-Functionalized Pyridine Monoimine Re(I) fac-Tricarbonyl Electrocatalyst. *Organometallics* **2015,** *34* (19), 4678-4683.

CHAPTER 2. A Reexamination of CO_2 Reduction with Fe_2S_2 Hydrogenase Mimics: Unexpected Role of Mono and Trinuclear Species

2.1 Introduction

The continued increase in atmospheric CO_2 and the eventual depletion of petrochemical feedstocks have sustained a continued interest in the utilization of CO_2 as a C1 source for liquid fuels.[1-3] A viable route for this process is the electrocatalytic reduction of CO_2 using homogeneous catalysts.[4-8] To this end, transition metal catalysts containing earth abundant metals such as Mn[9-18], Ni[19-27], Co,[23, 28-32] and Fe[33-40] have been extensively studied in recent years. The two simplest transformations, the two electron, two proton reduction of CO_2 to CO or formic acid are of considerable interest for further utilization in Fischer-Tropsch chemistry and formic acid fuel cells, respectively.[41-43] The selectivity between the two products relies on two distinct initial reactions (Figure 2.1). Where formate is made via the initial protonation of the active site followed by direct transfer of a hydride to CO_2, reduction to CO requires the direct addition of CO_2 to the active metal site followed either by subsequent protonation of the adduct to form a hydroxycarbonyl,[44-46] or by deoxygenation of the reduced CO_2 intermediate in multi-metallic[47-49] and Lewis acid assisted systems.[15, 34, 50] Due to this, the active site and proton source play a critical role in product selectivity. Therefore, understanding the mechanisms that lead to selectivity of one product over the other allows for rational design of new catalysts and systems that are optimized for high product selectivity.

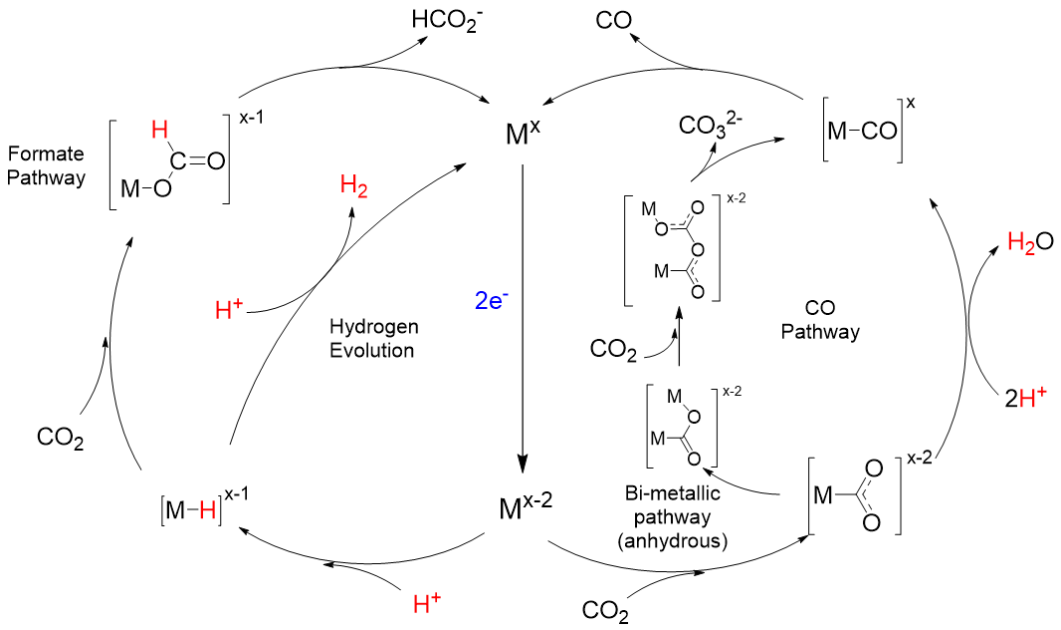

Figure 2.1. The multiple competing pathways that arise in CO_2 reduction catalysis. Following the two-electron reduction of the active site (M), there are two distinct pathways that can lead to different product selection. If M is protonated, then the products that arise can be H_2 from HER or HCO_2^- from CO_2 insertion. However, if CO_2 binds, CO is formed either from the subsequent protonation and formation of H_2O or from the anhydrous route of CO_2 disproportionation where CO and CO_3^{2-} are formed, usually through a bimetallic pathway.

One type of catalyst of interest for these types of reactions are the [FeFe] hydrogenase mimics. These catalysts have been shown to have multiple protonation and reduction pathways for the hydrogen evolution reaction (HER) that involves Fe-Fe cooperativity.[51-53] FeFe hydrogenase mimics have been shown to catalyze (HER) with both strong and weak acids.[54-55] Due to its selectivity with protons, it has been shown that, using a weak acid, $Fe_2(\mu\text{-bdt})(CO)_6$ (where bdt = benzene-1,2-dithiolate) was able to reduce CO_2 to formate as the major product.[38, 56] However, the mechanism for this pathway is poorly understood and it is unclear if this reactivity is mimicked using other bridging dithiolate ligands. Herein, we describe the electrochemical behavior of $Fe_2(\mu\text{-pdt})(CO)_6$, **1**, [where pdt = propane-1,3-dithiolate] for CO_2 reduction.

2.2 Results

2.2.1 Cyclic Voltammetry

The electrochemical properties of **1** have been previously reported in acetonitrile.[52, 57-59] The complex exhibits a one electron quasi-reversible reduction at -1.65 V vs $Fc^{+/0}$ followed by

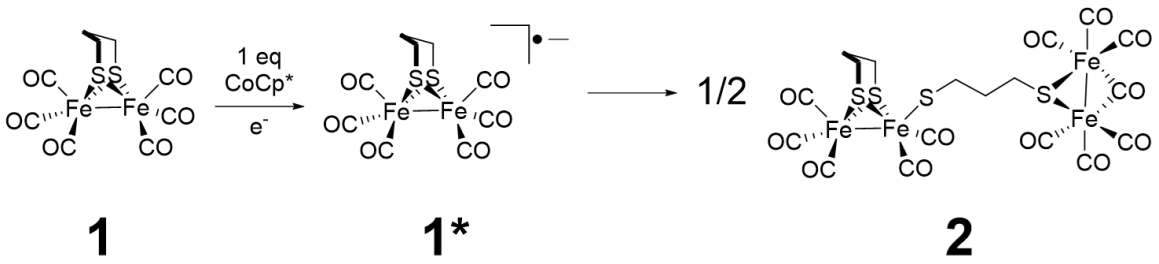

Figure 2.2. The previously reported electrochemical behavior of **1** in acetonitrile showing the dimerization of the complex following the one electron reduction.

two smaller, irreversible one-electron reductions at -2.18 and -2.33 V vs $Fc^{+/0}$ and one oxidation at -0.69 V vs $Fc^{+/0}$ (Figure 2.3A). The irreversibility of the reductions reveals that each reduction is followed by a chemical change of the compound. The first reduction of **1** has been shown to be a single electron reduction to **1*** followed by dimerization of the radical species to form **2** (Figure 2.2).[58, 60] This is confirmed by infrared spectroelectrochemistry (IR-SEC, *vide infra*), showing the formation of **2** at potentials negative of the first reduction (Figure 2.4 A). By increasing the scan rate, the first reduction becomes more reversible and the oxidation at -0.69 V vs $Fc^{+/0}$ disappears, confirming they are part of the diffusion limited dimerization process (Figure 2.7). At higher scan rates, the second and third reduction become a single, irreversible reduction at -2.16 V vs $Fc^{+/0}$ confirming that the second and third reductions are from the dimer that is formed (Figure 2.8).

Under CO_2 and in the absence of a proton source, CV shows catalytic current onset at second reduction (Figure 2.3A). To suppress H_2 evolution, the weak acid, MeOH (pK_a of 29.0 in DMSO)[61], was used as the proton source in this study. An increase in catalytic current is observed with increasing acid concentration, with i_{cat}/i_p= 25.1 in 1 M MeOH compared to i_{cat}/i_p= 17.5

without added MeOH (when the second reduction is used for i_p). This relationship indicates a proton dependence (Figure 2.3B). In addition, when 1 M CD_3OD is used, the i_{cat}/i_p decreases to

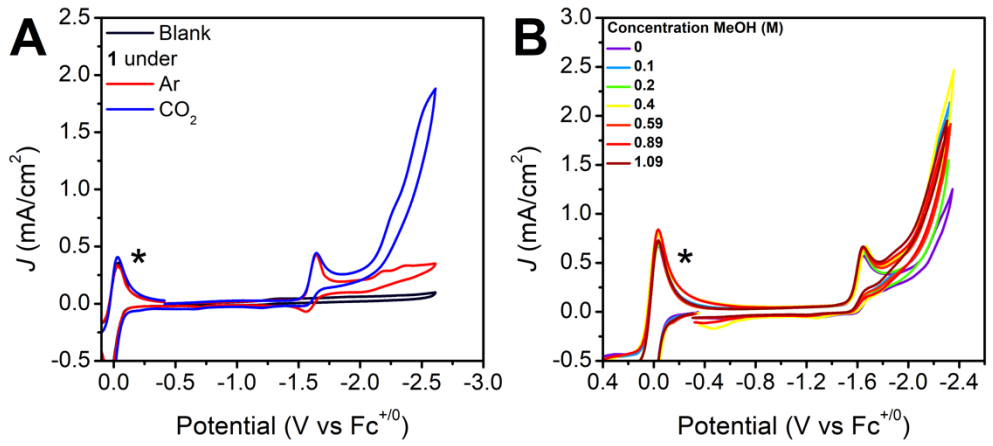

Figure 2.3. CV of 1 mM of **1** in dry MeCN with 100 mM $TBAPF_6$ purged with **A**. Ar (red) and CO_2 (blue) and **B**. purged with CO_2 with added MeOH with a Ag/AgCl reference electrode, graphite counter electrode and glassy carbon working electrode and ferrocene (*) as an internal reference. Scan rate = 100 mV/s.

15.1 (Figure 2.10), indicating a kinetic isotope effect and further confirming that protons participate in a rate limiting step. However, in the presence of CO_2 both with and without an added proton source, the CV (Figure 2.3) and IR-SEC (Figure 2.4A) at the first reduction remain unchanged. This indicates that neither CO_2 nor MeOH reacts with the radical species formed after the first reduction and that the catalytic species comes from the reduction of the dimer, **2.**

2.2.2 Controlled Potential Electrolysis

Controlled potential electrolysis (CPE) experiments under CO_2 in the presence and absence of MeOH reveal that three products are made during catalysis. Electrolysis at the second reduction (-1.8 V vs Ag/AgCl, ~ -2.2 V vs $Fc^{+/0}$) confirms that this system is catalytic for the reduction of CO_2 with an added weak acid. The Faradaic efficiency (FE) for CO and H_2 production was determined via gas chromatography. At the second reduction, the FE for CO is 16 ± 6% with H_2 accounting for of 56 ± 4% of the electrons passed. In addition, HCOOH was observed by NMR with a determined FE of 2.4% (Figure 2.13) through 3.8 turnovers relative to moles of **1** in solution.

When the bulk electrolysis is run at the third reduction (-2.0 V vs Ag/AgCl, ~ 2.4 V vs $Fc^{+/0}$), product distribution changes. While the major product, H_2 (FE = 46 ± 14) and CO (12 ± 3%) remaining within error of the results obtained at the lower potential, HCOOH production (FE=12%) increases significantly, with 3.52 turnovers relative to the moles of **1** in solution. The increase in FE for HCOOH demonstrates that the product distribution in the presence of MeOH is dependent on applied potential and that the product formed after the third reduction is likely responsible for the formate formation.

In the absence of proton source, the FE for CO decreases. The bulk electrolysis at the second reduction (-1.8 V vs Ag/AgCl, ~ -2.2 V vs $Fc^{+/0}$) produced CO with a FE of 12 ± 3% with 3.38 turnovers relative to the moles of **1** in solution. The major product remains H_2 (FE = 86 ± 1%) with HCOOH (FE = 3%) detectable by NMR. However, in this case, the presence of H_2 and HCOOH formation indicates that the active catalyst must scavenge protons from "adventitious water" in the solution, electrolyte ($TBAPF_6$) or the CH_3CN solvent.[62] When bulk electrolysis is run at the third reduction (-2.0 V vs Ag/AgCl, ~ -2.4 V vs $Fc^{+/0}$) with no added proton source, the

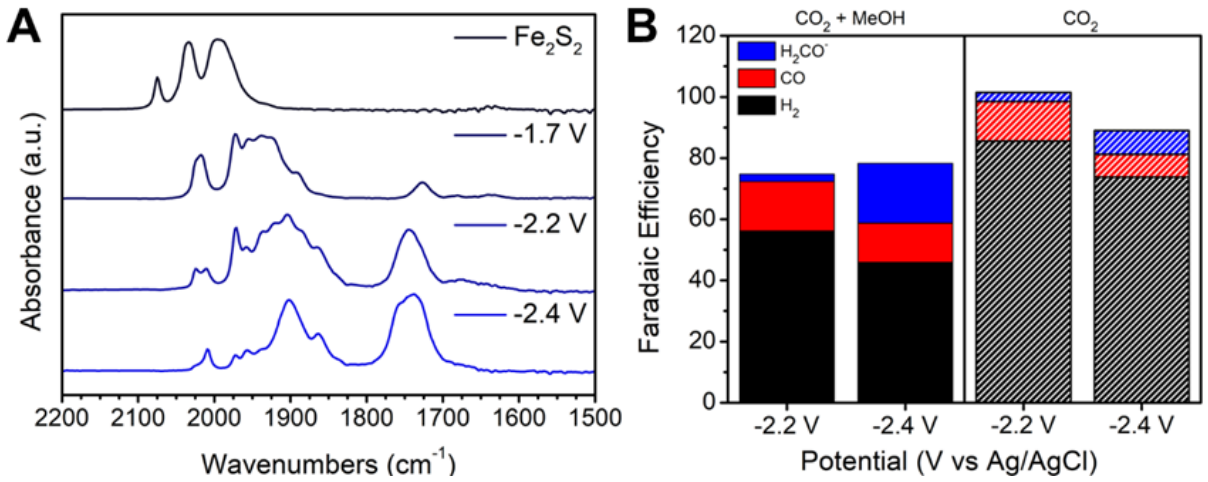

Figure 2.4. A) IR-SEC of 5 mM of 1 in dry MeCN with 100 mM TBAPF6 purged with N_2. Potentials are reported vs $Fc^{+/0}$ **B)** Total faradaic efficiency and selectivity from 60 min CPE experiments with 1 (2 mM) under CO_2 in the presence of 1 M MeOH (solid bars) and absence of MeOH (striped).

production of CO (FE = 7 ± 3) and H_2 (FE= 74 ± 9%) remain the same within error of the catalysis at the second reduction. However, HCOOH production increases to 8%, confirming that HCOOH production is dependent on applied potential. This further demonstrates that the active species for HCOOH product is most likely formed after the third reduction. When the electrolysis is run without CO_2 in 1 M MeOH in MeCN, H_2 is made with a FE of 99 ±24% and CO is made with a FE of 10 ±1% for CO production with a total of 2.23 turnovers relative to moles of **1** in solution. This reveals that while under catalytic conditions, catalyst degradation accounts for some of the CO formed during electrolysis.

2.2.3 Infrared Spectroelectrochemistry

Infrared spectroelectrochemistry was employed to provide insight into the active species formed under applied potentials needed for catalysis. IR-SEC confirms the formation of the dimer, **2**, upon the first reduction, even in the presence of CO_2 and weak acid. When the applied potential is increased beyond the second reduction (-1.8 V vs Ag/AgCl, ~ -2.2 V vs $Fc^{+/0}$), the bands associated with the dimer persist, and IR-SEC reveals there is partial conversion of two new

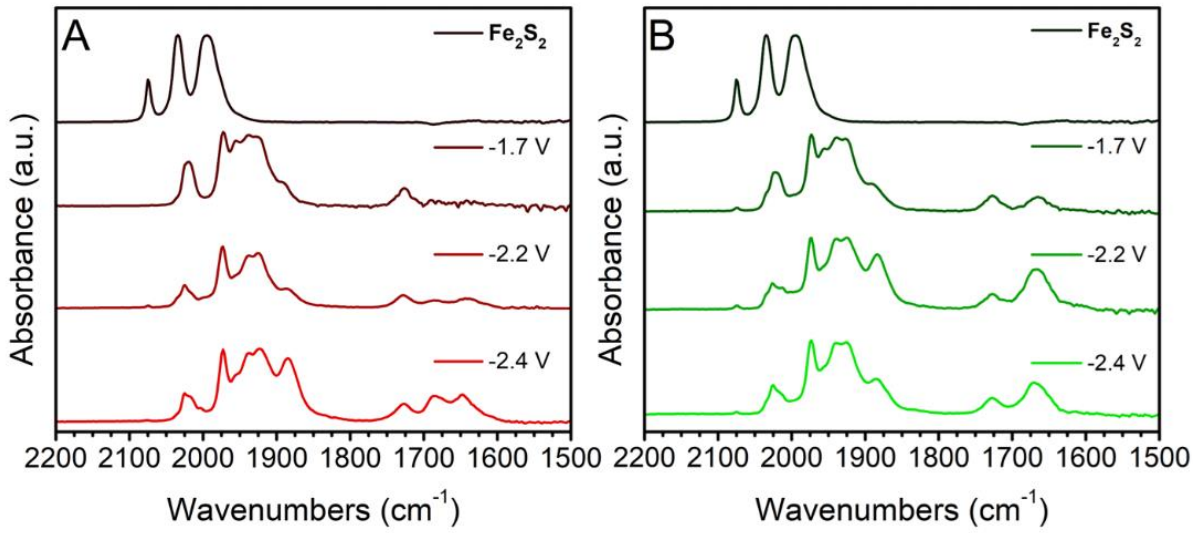

Figure 2.5. IR-SEC of 5 mM of 1 in dry MeCN with 100 mM TBAPF6 purged with CO_2 **A)** without added MeOH B) and with 1 M MeOH.

species, with the presence of an intense band at 1741 cm^{-1} in the spectra and a further increase in intensity of broad bands at 1901 cm^{-1} and 1861 cm^{-1} (Figure 2.4A). The strong intensity of the band at 1741 cm^{-1} is not consistent with a bridging CO ligand. In accordance with literature and our DFT analysis (*see Chapter Appendix*), we assign this band as the characteristic peak for **3**, $[Fe(CO)_4]^{2-}$, generally known as "Collman's reagent."[63] This has also been shown to be a side product formed from the reduction of similar [FeFe] hydrogenase mimics.[58] Upon further increase in applied potential to the third reduction (-2.0 V vs Ag/AgCl, ~ -2.4 V vs $Fc^{+/0}$), the spectrum is dominated by bands at 2007 cm^{-1}, 1889 cm^{-1}, 1861 cm^{-1}, 1757 cm^{-1}, and 1741 cm^{-1} (as well as some minor species). Using a DFT (TPSSH functional[64] with the Def2-TZVP basis set and utilizing a polarizable continuum model with acetonitrile as the solvent.[65-66]) scan of possible products (*see Appendix)*and previous literature reports,[67] we determine that the other peaks correspond to the trinuclear Fe species, **4**.

When IR-SEC is done under a CO_2 atmosphere, it allows for the determination of the kinetically slow steps or unreactive side products made in-situ during catalysis. When the applied potential is held past the second reduction in the absence of MeOH (-1.8 V vs Ag/AgCl, ~ -2.2 V vs $Fc^{+/0}$), there is a decrease in the intensity (with respect to the spectra of **2**) of the bands at 2017 cm^{-1} and 1954 cm^{-1} as well as the appearance of two new bands at 1685 cm^{-1} and 1647 cm^{-1} (Figure 2.5A). We assign these lower energy peaks as CO_3^{2-}. This suggests an anhydrous mechanism involving the conversion of two equivalents of CO_2 to CO and CO_3^{2-}, similar to observation with other CO_2 reduction catalysts.[68-70] Utilizing DFT, independent synthesis (*see Chapter Appendix*), and literature precedents,[58-59] the decrease in intensity of the two higher energy bands is assigned as the formation of **5** (Figure 2.6), from the single-electron reduction of **1** in the presence of CO gas produced during catalysis or the breaking of the dimer, **2**. As a result of the coordinately

saturated nature of **5**, it is likely that **5** is either off the catalytic cycle, or a slow step in the reduction of CO_2. When the potential is increased to the third reduction (-2.0 V vs Ag/AgCl, ~ -2.4 V vs $Fc^{+/0}$), there is an increase in the intensity of the bands corresponding to CO_3^{2-} as well as the formation of a new band at 1884 cm^{-1} (Figure 2.5A). DFT and previous literature precedent reveals that this is due to the formation of **3-H**, $[Fe(CO)_4H]^-$,[71] from the protonation of **3**.

When the applied potential is held past the second reduction in the presence of CO_2 and 1 M MeOH, the bands at 1685 cm^{-1} and 1647 cm^{-1} do not form, confirming the anhydrous route (Figure 2.5B). Instead, there is a single peak that forms at 1667 cm^{-1}, which we assign to water,[44] a byproduct formed during CO_2 reduction in the presence of protons. In addition, the band at 1884 cm^{-1} corresponding to $[Fe(CO)_4H]^-$, **3-H**, appears after the second reduction compared to the third in anhydrous conditions, revealing that the presence of a proton source allows for protonation of **3** to form **6** at lower potentials. Like the product distribution between the second and third reduction in the presence of MeOH, there is little change in the spectra when the applied potential is beyond the third reduction (-2.0 V vs Ag/AgCl, ~ -2.4 V vs $Fc^{+/0}$). The intensity of the band at 1884 cm^{-1} corresponding to **6** slightly decreases and the intensity of the band at 1667 cm^{-1} corresponding to water slightly increases in intensity.

2.3 Discussion

While the starting material, **1**, is a precursor to the electrochemical reduction of CO_2 to CO and HCOOH, the combined electrochemical, spectroscopic, and DFT analysis provides insight into the product selectivity and barriers to catalysis, especially when compared to similar compounds and systems. While the $Fe_2(\mu\text{-bdt})(CO)_6$ reported by Cheng[38] undergoes a two-electron reduction at the -1.30 V vs $Fc^{+/0}$, **1** undergoes only a single electron reduction at -1.65 V vs $Fc^{+/0}$.

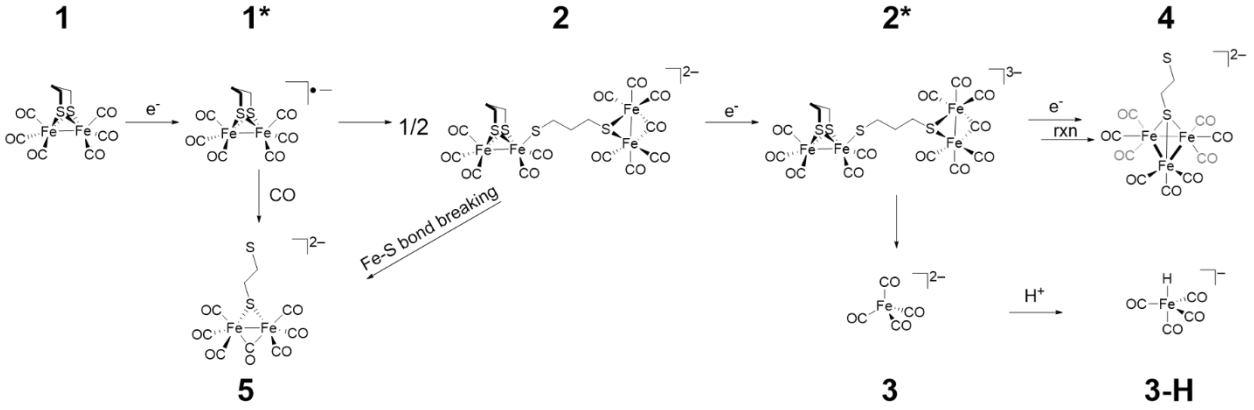

Figure 2.6. The electrochemical behavior of **1** determined via cyclic voltammetry, infrared spectroelectrochemistry, and density functional theory. **1** undergoes an ECECEC pathway, first forming a radical (**1***), followed by dimerization to form **2**. The reduction of **2** slowly converts to **3** at -2.18 V vs $Fc^{+/0}$ and **4** at potentials greater than -2.33 V vs $Fc^{+/0}$. Under catalytic conditions, **3** is protonated to form **3-H**. Additionally, **5** is formed either from the reduction of **1** in the presence CO or from the Fe-S bond breaking in **2**.

Literature precedent shows that using a stronger acid, such as acetic acid (pK_a in MeCN = 22.6)[72], is strong enough to react with the singly-reduced **1*** to form a hydride species instead of dimerizing to form **2**.[52, 55] However, as determined by IR-SEC and CV the weak acid, MeOH, is not strong enough to protonate **1*** prior to the formation of **2**, indicating an electrochemical (E) process followed a chemical process (C) prior to catalysis. The dimer, **2**, needs a further reduction to convert to the active species.

As the potential is scanned negative of the first reduction of **1**, the onset of catalytic potential corresponds to the formation of the bands associated with **2*** and **3**, as revealed in the in the IR-SEC study (Figure 2.16). The formation of **3** is a result of the labilization of the thiolate ligands due to the low formal oxidation state of the Fe upon the second reduction followed by decomposition. The catalysis in the presence of **2*** and **3** produces syngas, as H_2 and CO are formed in a roughly 3:1 mixture. The presence of CO_3^{2-} in the IR-SEC indicates a change in mechanism for CO_2 reduction like the one proposed in Figure 2.1, involving an anhydrous reduction/disproportionation of CO_2. The drop in the yield of CO production under these conditions is likely due to the added barriers introduced from the need for a second equivalent of

CO_2 in the reduction/disproportionation mechanisms. Interestingly, H_2 is still produced under these conditions, suggesting that the "adventitious water" is strong enough to protonate the hydride that is formed, but not strong enough to protonate the COOH-adduct to produce CO and water.

Another previously unobserved step in the di-iron complexes reported here is that the third reduction of **1** leads to the formation of **4**, a trinuclear iron species which coincides with the increase of HCOOH production. The structure of **4** was determined via combined IR-SEC and DFT analyses. Several possible structures for the product were screened for their FTIR spectra using TPSSH functional[64] with the Def2-TZVP basis set. The DFT determined FTIR spectra of **4** matches the bands that are formed upon the third reduction of **1**. This reactivity is similar to that determined upon the reduction of similar FeFe hydrogenase mimics, with one bridging thiol.[67] Work by Berben and coworkers have shown that similar iron carbonyl clusters are selective for CO_2 reduction to HCOOH.[35-36, 73-75] Interestingly, they showed that there is an increase in selectivity for HCOOH with a weak proton shuttle.[35] Further studies will be needed to determine if the thiolate in **4** can mimic this reactivity.

2.4 Conclusion

In conclusion, reduction of CO_2 by **1** with and without weak acid was explored. By a combination of CV, IR-SEC, and DFT efforts, it was determined that the active catalyst is formed after the formation of the dimer, **2**, in solution. The reduction of this dimer leads to the formation of the catalytically active species. IR-SEC indicates that at potentials needed for the onset of catalytic current, reduction of the dimer occurs, forming **2*** and the mononuclear species, $[Fe(CO)_4]^{2-}$ (**3**). In the presence of these compounds, the system is selective for H_2 evolution and CO production with traces of HCOOH produced. However, upon the formation of trinuclear Fe species **4**, there is an increase in the formation of HCOOH. The formation of three distinct species,

each with different activities for CO_2 reduction and HER is the cause for the range of products formed during catalysis. Additionally, two other products were determined to be formed during catalysis. IR-SEC under catalytic conditions revealed that coordinatively saturated **5** forms, either due to the breaking in a Fe-S bond in **2** or from the reaction of **1*** with CO. In addition, **3-H** is formed by the protonation of **3**. It is determined that **3-H** and **5** are likely to be measured as they are formed during a slow step in catalysis or as a decomposition product.

2.5 Methods and Materials

2.5.1 General Considerations

Complexes **1**, **2**, and **5** were prepared via literature reports. Reactions were performed using standard Schlenk-line and glove box techniques under an atmosphere of nitrogen. Flash column chromatography was performed on a Teledyneisco CombiFlash Rf200 using SiO_2 or neutral alumina loaded columns. All reagents were purchased from commercial sources and were used without further purification unless otherwise noted. Acetonitrile was stored under argon and dried on a custom dry solvent system over alumina columns and stories over molecular sieves before use. Tetrabutylammonium hexafluorophosphate (TBAPF6, Aldrich, 98%) was twice recrystallized from methanol and dried under vacuum at 90 °C for 16 h before use.

2.5.2 Instrumentation

1H NMR spectra were recorded on a JOEL 400 MHz spectrometer. 1H NMR chemical shifts are reported relative to TMS (δ=0) and referenced to residual solvent proton peaks. FTIR spectra were recorded on a Thermo Scientific Nicolet 6700. Acquired spectra were averaged over 32 scans at a 4 cm^{-1} resolution. Gas samples were analyzed on a Hewlett-Packard 7890A Series Gas Chromatogram with two molsieve columns (30m × 0.53 mm i.d. × 25 μm film).

2.5.3 Cyclic Voltammetry (CV)

Electrochemical experiments were performed in 0.1 M tetra-*n*-butylammonium hexafluorophosphate solution in 5 mL acetonitrile with 1mM catalyst using a BAS Epsilon potentiostat. Ferrocene was used as an internal standard (1 mM) for all scans. A scintillation vial with a custom fitted top was used, utilizing a 3 mm diameter glassy carbon electrode (from BASi) as the working electrode. The counter electrode was a Pt wire, and the pseudoreference electrode was a Ag/AgCl electrode that was separated from solution by a Vycor tip and a glass tube that was filled with 0.1 M $TBAPF_6$ solution in MeCN. The Pt wire was flame-treated with a butane torch before use. The glass carbon electrode was polished on 15-, 3-, and 1-micron diamond paste, rinsed with methanol and dried under a stream of nitrogen prior to use. To minimize the amount of solvent loss and adventitious water buildup, for all experiments, argon and "bone dry" CO_2 were first run through their own Drierite columns then through a sealed vial of dry MeCN filled with 3 Å sieves. An oven-dried cannula was used to transfer the MeCN-saturated, dry gas to the electrochemical set up. Electrochemical solutions were sparged for at least 10 minutes prior to the start of data collection and kept under a blanket of gas during experiments. Ohmic drop was corrected using the potentiostat's iR-compensation tool, correcting for 90-100% of the measured resistance.

2.5.4 Infrared Spectroelectrochemistry (IR-SEC)

Infrared Spectroelectrochemistry (IR-SEC) was preformed using a custom-built IR-SEC cell consisting of a 1 cm diameter glassy carbon working electrode, a Pt counter electrode, and a Ag pseudo-reference electrode that have been polished to a mirror finish. Under an atmosphere of either Ar or CO_2, the cell was loaded with an acetonitrile solution consisting of **1** (5 mM) and $TBAPF_6$ (0.1 M) and, when applicable, 0.1 M MeOH. The potential of the IR-SEC cell was controlled using a BAS Epsilon potentiostat. Thin-layer controlled electrolysis was monitored

via reflectance spectroscopy off the polished glassy carbon working electrode and infrared spectra were collected on a Thermo Scientific Nicolet 6700. All the potentials were in reference to a pseudoreference electrode, Ag/Ag+ (~ +400 mV from the Fc/Fc+ couple).

2.5.5 Computational Benchmarking

All Calculations were run in Gaussian 16.[76] The method used was tested by benchmarking functionals and basis sets against the experimental spectrum of **5** in acetonitrile, arriving at the following method which required no scaling factor for good agreeance with the empirical infrared spectra. The final optimizations and frequency calculations were ran with the TPSSH functional[64] with the Def2-TZVP basis set[77] utilizing a polarizable continuum model (PCM) with acetonitrile as the solvent.[65-66] When possible initial geometries were set using available crystallographic data, and otherwise drawn in Avogadro[78] and preliminarily optimized using the UFF force field.[79] The resulting vibrational spectra were visualized using Gabedit.[80]

2.5.6 Synthesis of 1

The synthesis of **1** followed previously published literature precedent.[81] Briefly, in a round bottom flask, 0.600 mg (1.19 mmol, 1 eq) of $Fe_3(CO)_{12}$ was added to 100 mL toluene. The solution was sparged with nitrogen and 0.258 g of 1,3-propanedithiol (2.38 mmol, 2 eq, 0.239 mL) was added via a syringe. The resulting solution was put under N_2 and heated to reflux for 2 hrs. The solution was then removed to heat allowed to cool for 30 minutes. The solvent was then removed via rotary evaporation and the resulting solid was purified via column chromatography to give a red solid. The solid was recrystallized by slow evaporation of hexane to give analytically pure product. (63% yield)

IR (FTIR) in MeCN ν_{max}(CO) [cm^{-1}]: 2074, 2034, 1995.

^{1}H NMR (500 MHz, MeCN-d_3) δ /ppm 1.75-1.80 (m, 2H), 2.18 (t, 4H, *J*=5.9 Hz)

2.5.7 Synthesis of 5

The synthesis of **5** followed previously published literature precedent.[59] Briefly, in a Schlenk flask containing a stir bar and ~10 mL of dry tetrahydrofuran, **1** (50 mg, 0.130 mmol, 1 eq) and 18-crown-6 (34.2 mg, 0.130 mmol, 1 eq) was added. In a separate Schlenk flask containing ~5 mL tetrahydrofuran, $NaBH_4$ (9.80 mg, 0.260 mmol, 2 eq) was added. Using Schlenk line techniques, both solutions were degassed via the freeze-pump-thaw method followed by the addition of CO the flasks. Using a canula, the solution of NaBH4 was slowly added dropwise. The solution was allowed to stir for 30 min to give a dark-green solution. The solvent was removed under vacuum the flask was moved to a N_2-filled glovebox. The green oily substance was washed with diethyl ether and toluene and further dried under vacuum to give a green solid.

IR (FTIR) in THF ν_{max}(CO) [cm^{-1}]: 2023, 1969, 1936, 1920, 1742.

2.5 Acknowledgements

Chapter 2, in part, is being prepared for submission for publication of the material entitled Miller, C.J.; Barrett, J.A.; Chan, T.; Shandilya, A.; Lee, B.; Kubiak, C.P. "A Reexamination of CO_2 Reduction with a Fe_2S_2 Hydrogenase Mimic: Unexpected Role of Mononuclear and Trinuclear Species," *Manuscript in Preparation.* The dissertation author is the primary author of this material. We acknowledge Dr. Michael Neville for invaluable disccusions. This work is support by the Air Force Office of Scientific Research under Award No. FA9550-17-0198.

2.6 References

1. Kumar, B.; Llorente, M.; Froehlich, J.; Dang, T.; Sathrum, A.; Kubiak, C. P., Photochemical and Photoelectrochemical Reduction of CO_2. *Annu. Rev. Phys. Chem.* **2012**.

2. Lewis, N. S., Research opportunities to advance solar energy utilization. *Science* **2016,** *351* (6271), aad1920.

3. Nitopi, S.; Bertheussen, E.; Scott, S. B.; Liu, X.; Engstfeld, A. K.; Horch, S.; Seger, B.; Stephens, I. E. L.; Chan, K.; Hahn, C.; Nørskov, J. K.; Jaramillo, T. F.; Chorkendorff, I., Progress and Perspectives of Electrochemical CO2 Reduction on Copper in Aqueous Electrolyte. *Chem. Rev.* **2019,** *119* (12), 7610-7672.

4. Barrett, J. A.; Miller, C. J.; Kubiak, C. P., Electrochemical Reduction of CO₂ Using Group VII Metal Catalysts. *Trends in Chemistry* **2021,** *3* (3), 176-187.

5. Barrett, A. J. A.; Brunner, B. F. M.; Cheung, C. P. L.; Kubiak, D. C. P.; Lee, E. G. L.; Miller, F. C. J.; Waldie, G. K. M.; Zhanaidarova, H. A., Chapter 1 Approaches to Controlling Homogeneous Electrochemical Reduction of Carbon Dioxide. In *Carbon Dioxide Electrochemistry: Homogeneous and Heterogeneous Catalysis*, The Royal Society of Chemistry: 2021; pp 1-66.

6. Rakowski Dubois, M.; Dubois, D. L., Development of Molecular Electrocatalysts for CO2 Reduction and H2 Production/Oxidation. *Acc. Chem. Res.* **2009,** *42* (12), 1974-1982.

7. Appel, A. M.; Bercaw, J. E.; Bocarsly, A. B.; Dobbek, H.; DuBois, D. L.; Dupuis, M.; Ferry, J. G.; Fujita, E.; Hille, R.; Kenis, P. J. A.; Kerfeld, C. A.; Morris, R. H.; Peden, C. H. F.; Portis, A. R.; Ragsdale, S. W.; Rauchfuss, T. B.; Reek, J. N. H.; Seefeldt, L. C.; Thauer, R. K.; Waldrop, G. L., Frontiers, Opportunities, and Challenges in Biochemical and Chemical Catalysis of CO2 Fixation. *Chem. Rev.* **2013,** *113* (8), 6621-6658.

8. Francke, R.; Schille, B.; Roemelt, M., Homogeneously Catalyzed Electroreduction of Carbon Dioxide—Methods, Mechanisms, and Catalysts. *Chem. Rev.* **2018,** *118* (9), 4631-4701.

9. Agarwal, J.; Shaw, T. W.; Schaefer, H. F., III; Bocarsly, A. B., Design of a Catalytic Active Site for Electrochemical CO2 Reduction with Mn(I)-Tricarbonyl Species. *Inorg. Chem.* **2015,** *54* (11), 5285-5294.

10. Bourrez, M.; Molton, F.; Chardon-Noblat, S.; Deronzier, A., [Mn(bipyridyl)CO3Br]: An Abundant Metal Carbonyl Complex as Efficient Electrocatalyst for CO2 Reduction. *Angew. Chem., Int. Ed.* **2011,** *50* (42), 9903-9906, S9903/1-S9903/9.

11. Franco, F.; Cometto, C.; Nencini, L.; Barolo, C.; Sordello, F.; Minero, C.; Fiedler, J.; Robert, M.; Gobetto, R.; Nervi, C., Local Proton Source in Electrocatalytic CO2 Reduction with [Mn(bpy-R)(CO)(3)Br] Complexes. *Chemistry-a European Journal* **2017,** *23* (20), 4782-4793.

12. Grice, K. A.; Kubiak, C. P., Recent studies of rhenium and manganese bipyridine carbonyl catalysts for the electrochemical reduction of CO2. *Adv. Inorg. Chem.* **2014,** *66*, 163-188.

13. Machan, C. W.; Kubiak, C. P., Electrocatalytic reduction of carbon dioxide with Mn(terpyridine) carbonyl complexes. *Dalton Trans.* **2016,** *45* (43), 17179-17186.

14. Machan, C. W.; Stanton, C. J., III; Vandezande, J. E.; Majetich, G. F.; Schaefer, H. F., III; Kubiak, C. P.; Agarwal, J., Electrocatalytic Reduction of Carbon Dioxide by Mn(CN)(2,2'-bipyridine)(CO)3: CN Coordination Alters Mechanism. *Inorg. Chem.* **2015,** *54* (17), 8849-8856.

15. Sampson, M. D.; Kubiak, C. P., Manganese Electrocatalysts with Bulky Bipyridine Ligands: Utilizing Lewis Acids To Promote Carbon Dioxide Reduction at Low Overpotentials. *J. Am. Chem. Soc.* **2016,** *138* (4), 1386-1393.

16. Sampson, M. D.; Nguyen, A. D.; Grice, K. A.; Moore, C. E.; Rheingold, A. L.; Kubiak, C. P., Manganese catalysts with bulky bipyridine ligands for the electrocatalytic reduction of carbon dioxide: Eliminating dimerization and altering catalysis. *J. Am. Chem. Soc.* **2014,** *136* (14), 5460-5471.

17. Smieja, J. M.; Sampson, M. D.; Grice, K. A.; Benson, E. E.; Froehlich, J. D.; Kubiak, C. P., Manganese as a Substitute for Rhenium in CO2 Reduction Catalysts: The Importance of Acids. *Inorg. Chem.* **2013,** *52* (5), 2484-2491.

18. Walsh, J. J.; Neri, G.; Smith, C. L.; Cowan, A. J., Electrocatalytic CO2 reduction with a membrane supported manganese catalyst in aqueous solution. *Chem. Commun. (Cambridge, U. K.)* **2014,** *50* (84), 12698-12701.

19. Beley, M.; Collin, J. P.; Ruppert, R.; Sauvage, J. P., Nickel(II)-cyclam: an extremely selective electrocatalyst for reduction of carbon dioxide in water. *J. Chem. Soc., Chem. Commun.* **1984,** (19), 1315-16.

20. Bujno, K.; Bilewicz, R.; Siegfried, L.; Kaden, T. A., Effects of ligand structure on the adsorption of nickel tetraazamacrocyclic complexes and electrocatalytic CO2 reduction. *J. Electroanal. Chem.* **1998,** *445*, 47-53.

21. Collin, J. P.; Jouaiti, A.; Sauvage, J. P., Electrocatalytic properties of (tetraazacyclotetradecane)nickel(2+) and Ni2(biscyclam)4+ with respect to carbon dioxide and water reduction. *Inorg. Chem.* **1988,** *27* (11), 1986-90.

22. Cope, J. D.; Liyanage, N. P.; Kelley, P. J.; Denny, J. A.; Valente, E. J.; Webster, C. E.; Delcamp, J. H.; Hollis, T. K., Electrocatalytic reduction of CO2 with CCC-NHC pincer nickel complexes. *Chem. Commun. (Cambridge, U. K.)* **2017,** *53* (68), 9442-9445.

23. Fisher, B. J.; Eisenberg, R., Electrocatalytic reduction of carbon dioxide by using macrocycles of nickel and cobalt. *J. Am. Chem. Soc.* **1980,** *102* (24), 7361-3.

24. Froehlich, J. D.; Kubiak, C. P., Homogeneous CO2 Reduction by Ni(cyclam) at a Glassy Carbon Electrode. *Inorg. Chem.* **2012,** *51* (7), 3932-3934.

25. Froehlich, J. D.; Kubiak, C. P., The Homogeneous Reduction of CO2 by [Ni(cyclam)]+: Increased Catalytic Rates with the Addition of a CO Scavenger. *J. Am. Chem. Soc.* **2015,** *137* (10), 3565-3573.

26. Neri, G.; Aldous, I. M.; Walsh, J. J.; Hardwick, L. J.; Cowan, A. J., A highly active nickel electrocatalyst shows excellent selectivity for CO2 reduction in acidic media. *Chem. Sci.* **2016,** *7*, 1521-1526.

27. Thoi, V. S.; Chang, C. J., Nickel N-heterocyclic carbene-pyridine complexes that exhibit selectivity for electrocatalytic reduction of carbon dioxide over water. *Chem. Commun. (Cambridge, U. K.)* **2011,** *47* (23), 6578-6580.

28. Bonin, J.; Maurin, A.; Robert, M., Molecular catalysis of the electrochemical and photochemical reduction of CO2 with Fe and Co metal based complexes. Recent advances. *Coord. Chem. Rev.* **2017,** *334*, 184-198.

29. Chapovetsky, A.; Do, T. H.; Haiges, R.; Takase, M. K.; Marinescu, S. C., Proton-Assisted Reduction of CO2 by Cobalt Aminopyridine Macrocycles. *J. Am. Chem. Soc.* **2016,** *138* (18), 5765-5768.

30. Grodkowski, J.; Neta, P.; Fujita, E.; Mahammed, A.; Simkhovich, L.; Gross, Z., Reduction of Cobalt and Iron Corroles and Catalyzed Reduction of CO2. *J. Phys. Chem. A* **2002,** *106* (18), 4772-4778.

31. Lacy, D. C.; McCrory, C. C. L.; Peters, J. C., Studies of Cobalt-Mediated Electrocatalytic CO2 Reduction Using a Redox-Active Ligand. *Inorg. Chem.* **2014,** *53* (10), 4980-4988.

32. Roy, S.; Sharma, B.; Pecaut, J.; Simon, P.; Fontecave, M.; Tran, P. D.; Derat, E.; Artero, V., Molecular Cobalt Complexes with Pendant Amines for Selective Electrocatalytic Reduction of Carbon Dioxide to Formic Acid. *J. Am. Chem. Soc.* **2017,** *139* (10), 3685-3696.

33. Bhugun, I.; Lexa, D.; Saveant, J.-M., Catalysis of the Electrochemical Reduction of Carbon Dioxide by Iron(0) Porphyrins: Synergistic Effect of Weak Broensted Acids. *J. Am. Chem. Soc.* **1996,** *118* (7), 1769-76.

34. Hammouche, M.; Lexa, D.; Momenteau, M.; Saveant, J. M., Chemical catalysis of electrochemical reactions. Homogeneous catalysis of the electrochemical reduction of carbon dioxide by iron("0") porphyrins. Role of the addition of magnesium cations. *J. Am. Chem. Soc.* **1991,** *113* (22), 8455-66.

35. Loewen, N. D.; Thompson, E. J.; Kagan, M.; Banales, C. L.; Myers, T. W.; Fettinger, J. C.; Berben, L. A., A pendant proton shuttle on [Fe4N(CO)12]- alters product selectivity in formate vs. H2 production via the hydride [H-Fe4N(CO)12]-. *Chem. Sci.* **2016,** *7*, 2728-2735.

36. Rail, M. D.; Berben, L. A., Directing the reactivity of [HFe4N(CO)12]- toward H+ or CO2 reduction by understanding the electrocatalytic mechanism. *J. Am. Chem. Soc.* **2011,** *133* (46), 18577-18579.

37. Taheri, A.; Berben, L. A., Making C-H bonds with CO2: production of formate by molecular electrocatalysts. *Chem. Commun. (Cambridge, U. K.)* **2016,** *52* (9), 1768-1777.

38. Cheng, M.; Yu, Y.; Zhou, X.; Luo, Y.; Wang, M., Chemical Versatility of [FeFe]-Hydrogenase Models: Distinctive Activity of [μ-C6H4-1,2-(κ2-S)2][Fe2(CO)6] for Electrocatalytic CO2 Reduction. *ACS Catal.* **2019,** *9* (1), 768-774.

39. Wang, L.; Fan, F.; Liu, J.; Cheng, M., Homogeneous electrocatalytic CO2 reduction by hexacarbonyl diiron dithiolate complex bearing hydroquinone. *J. Organomet. Chem.* **2021,** *954-955*, 122094.

40. Berben, L. A.; Loewen, N. D., 5.12 - Group 7 and 8 Catalysts for Electrocatalytic CO2 Conversion. In *Comprehensive Coordination Chemistry III*, Constable, E. C.; Parkin, G.; Que Jr, L., Eds. Elsevier: Oxford, 2021; pp 742-773.

41. Lu, S.; Shi, Y.; Meng, N.; Lu, S.; Yu, Y.; Zhang, B., Electrosynthesis of Syngas via the Co-Reduction of CO2 and H2O. *Cell Reports Physical Science* **2020,** *1* (11), 100237.

42. Waldie, K. M.; Ostericher, A. L.; Reineke, M. H.; Sasayama, A. F.; Kubiak, C. P., Hydricity of Transition-Metal Hydrides: Thermodynamic Considerations for CO2 Reduction. *ACS Catal.* **2018,** *8* (2), 1313-1324.

43. Waldie, K. M.; Brunner, F. M.; Kubiak, C. P., Transition Metal Hydride Catalysts for Sustainable Interconversion of CO2 and Formate: Thermodynamic and Mechanistic Considerations. *ACS Sustainable Chemistry & Engineering* **2018,** *6* (5), 6841-6848.

44. Machan, C. W.; Sampson, M. D.; Kubiak, C. P., A Molecular Ruthenium Electrocatalyst for the Reduction of Carbon Dioxide to CO and Formate. *J. Am. Chem. Soc.* **2015,** *137* (26), 8564-8571.

45. Barlow, J. M.; Yang, J. Y., Thermodynamic Considerations for Optimizing Selective CO2 Reduction by Molecular Catalysts. *ACS Central Science* **2019,** *5* (4), 580-588.

46. Ceballos, B. M.; Yang, J. Y., Highly Selective Electrocatalytic CO2 Reduction by [Pt(dmpe)2]2+ through Kinetic and Thermodynamic Control. *Organometallics* **2020,** *39* (9), 1491-1496.

47. Dubois, M. R.; Dubois, D. L., Development of Molecular Electrocatalysts for CO2 Reduction and H-2 Production/Oxidation. *Acc. Chem. Res.* **2009,** *42* (12), 1974-1982.

48. Jeoung, J.-H.; Dobbek, H., Carbon Dioxide Activation at the Ni,Fe-Cluster of Anaerobic Carbon Monoxide Dehydrogenase. *Science* **2007,** *318* (5855), 1461-1464.

49. Raebiger, J. W.; Turner, J. W.; Noll, B. C.; Curtis, C. J.; Miedaner, A.; Cox, B.; DuBois, D. L., Electrochemical Reduction of CO2 to CO Catalyzed by a Bimetallic Palladium Complex. *Organometallics* **2006,** *25* (14), 3345-3351.

50. Zhanaidarova, A.; Steger, H.; Reineke, M. H.; Kubiak, C. P., Chelated [Zn(cyclam)]2+ Lewis acid improves the reactivity of the electrochemical reduction of CO2 by Mn catalysts with bulky bipyridine ligands. *Dalton Trans.* **2017,** *46* (37), 12413-12416.

51. Schilter, D.; Camara, J. M.; Huynh, M. T.; Hammes-Schiffer, S.; Rauchfuss, T. B., Hydrogenase Enzymes and Their Synthetic Models: The Role of Metal Hydrides. *Chem. Rev.* **2016,** *116* (15), 8693-8749.

52. Chong, D.; Georgakaki, I. P.; Mejia-Rodriguez, R.; Sanabria-Chinchilla, J.; Soriaga, M. P.; Darensbourg, M. Y., Electrocatalysis of hydrogen production by active site analogues of the iron hydrogenase enzyme: structure/function relationships. *Dalton Trans.* **2003,** (21), 4158-4163.

53. Borg, S. J.; Bondin, M. I.; Best, S. P.; Razavet, M.; Liu, X.; Pickett, C. J., Electrocatalytic proton reduction by dithiolate-bridged diiron carbonyl complexes: a connection to the H-cluster? *Biochem. Soc. Trans.* **2005,** *33* (1), 3-6.

54. Duan, L.; Wang, M.; Li, P.; Na, Y.; Wang, N.; Sun, L., Carbene–pyridine chelating 2Fe2S hydrogenase model complexes as highly active catalysts for the electrochemical reduction of protons from weak acid (HOAc). *Dalton Trans.* **2007,** (13), 1277-1283.

55. Greco, C.; Zampella, G.; Bertini, L.; Bruschi, M.; Fantucci, P.; De Gioia, L., Insights into the Mechanism of Electrocatalytic Hydrogen Evolution Mediated by Fe2(S2C3H6)(CO)6: The Simplest Functional Model of the Fe-Hydrogenase Active Site. *Inorg. Chem.* **2007,** *46* (1), 108-116.

56. Gao, S.; Liu, Y.; Shao, Y.; Jiang, D.; Duan, Q., Iron carbonyl compounds with aromatic dithiolate bridges as organometallic mimics of [FeFe] hydrogenases. *Coord. Chem. Rev.* **2020,** *402*, 213081.

57. Mejia-Rodriguez, R.; Chong, D.; Reibenspies, J. H.; Soriaga, M. P.; Darensbourg, M. Y., The Hydrophilic Phosphatriazaadamantane Ligand in the Development of H2 Production Electrocatalysts: Iron Hydrogenase Model Complexes. *J. Am. Chem. Soc.* **2004,** *126* (38), 12004-12014.

58. Borg, S. J.; Tye, J. W.; Hall, M. B.; Best, S. P., Assignment of Molecular Structures to the Electrochemical Reduction Products of Diiron Compounds Related to [Fe−Fe] Hydrogenase: A Combined Experimental and Density Functional Theory Study. *Inorg. Chem.* **2007,** *46* (2), 384-394.

59. Borg, S. J.; Behrsing, T.; Best, S. P.; Razavet, M.; Liu, X.; Pickett, C. J., Electron Transfer at a Dithiolate-Bridged Diiron Assembly: Electrocatalytic Hydrogen Evolution. *J. Am. Chem. Soc.* **2004,** *126* (51), 16988-16999.

60. Aguirre de Carcer, I.; DiPasquale, A.; Rheingold, A. L.; Heinekey, D. M., Active-Site Models for Iron Hydrogenases: Reduction Chemistry of Dinuclear Iron Complexes. *Inorg. Chem.* **2006,** *45* (20), 8000-8002.

61. Olmstead, W. N.; Margolin, Z.; Bordwell, F. G., Acidities of water and simple alcohols in dimethyl sulfoxide solution. *The Journal of Organic Chemistry* **1980,** *45* (16), 3295-3299.

62. Clark, M. L.; Cheung, P. L.; Lessio, M.; Carter, E. A.; Kubiak, C. P., Kinetic and mechanistic effects of bipyridine (bpy) substituent, labile ligand, and Bronsted acid on electrocatalytic CO2 reduction by Re(bpy) complexes. *ACS Catal.* **2018,** *8*, 2021-2029.

63. Collman, J. P.; Finke, R. G.; Cawse, J. N.; Brauman, J. I., Oxidative-addition reactions of the disodium tetracarbonylferrate supernucleophile. *J. Am. Chem. Soc.* **1977,** *99* (8), 2515-2526.

64. Tao, J.; Perdew, J. P.; Staroverov, V. N.; Scuseria, G. E., Climbing the Density Functional Ladder: Nonempirical Meta--Generalized Gradient Approximation Designed for Molecules and Solids. *Phys. Rev. Lett.* **2003,** *91* (14), 146401.

65. Tomasi, J.; Mennucci, B.; Cammi, R., Quantum Mechanical Continuum Solvation Models. *Chem. Rev.* **2005,** *105* (8), 2999-3094.

66. Miertuš, S.; Scrocco, E.; Tomasi, J., Electrostatic interaction of a solute with a continuum. A direct utilizaion of AB initio molecular potentials for the prevision of solvent effects. *Chem. Phys.* **1981,** *55* (1), 117-129.

67. Shupp, J. P.; Rose, A. R.; Rose, M. J., Synthesis and interconversions of reduced, alkali–metal supported iron–sulfur–carbonyl complexes. *Dalton Trans.* **2017,** *46* (28), 9163-9171.

68. Machan, C. W.; Chabolla, S. A.; Kubiak, C. P., Reductive Disproportionation of Carbon Dioxide by an Alkyl-Functionalized Pyridine Monoimine Re(I) fac-Tricarbonyl Electrocatalyst. *Organometallics* **2015,** *34* (19), 4678-4683.

69. Ramakrishnan, S.; Chidsey, C. E. D., Initiation of the Electrochemical Reduction of CO2 by a Singly Reduced Ruthenium(II) Bipyridine Complex. *Inorg. Chem.* **2017,** *56* (14), 8326-8333.

70. Chen, Z.; Chen, C.; Weinberg, D. R.; Kang, P.; Concepcion, J. J.; Harrison, D. P.; Brookhart, M. S.; Meyer, T. J., Electrocatalytic reduction of CO2 to CO by polypyridyl ruthenium complexes. *Chem. Commun. (Cambridge, U. K.)* **2011,** *47* (47), 12607-12609.

71. Darensbourg, M. Y.; Darensbourg, D. J.; Barros, H. L. C., Solution structure and reactivity of hydridoiron tetracarbonyl anion, [HFe(CO)4]. *Inorg. Chem.* **1978,** *17* (2), 297-301.

72. Izutsu, K., *Acid-base dissociation constants in dipolar aprotic solvents*. Blackwell Scientific Publications: Oxford, 1990.

73. Taheri, A.; Thompson, E. J.; Fettinger, J. C.; Berben, L. A., An Iron Electrocatalyst for Selective Reduction of CO2 to Formate in Water: Including Thermochemical Insights. *ACS Catal.* **2015,** *5* (12), 7140-7151.

74. Loewen, N. D.; Neelakantan, T. V.; Berben, L. A., Renewable Formate from C-H Bond Formation with CO2: Using Iron Carbonyl Clusters as Electrocatalysts. *Acc. Chem. Res.* **2017,** *50* (9), 2362-2370.

75. Taheri, A.; Berben, L. A., Tailoring Electrocatalysts for Selective CO2 or H+ Reduction: Iron Carbonyl Clusters as a Case Study. *Inorg. Chem.* **2016,** *55* (2), 378-385.

76. Frisch, M. J.; Trucks, G. W.; Schlegel, H. B.; Scuseria, G. E.; Robb, M. A.; Cheeseman, J. R.; Scalmani, G.; Barone, V.; Petersson, G. A.; Nakatsuji, H.; Li, X.; Caricato, M.; Marenich, A. V.; Bloino, J.; Janesko, B. G.; Gomperts, R.; Mennucci, B.; Hratchian, H. P.; Ortiz, J. V.; Izmaylov, A. F.; Sonnenberg, J. L.; Williams; Ding, F.; Lipparini, F.; Egidi, F.; Goings, J.; Peng, B.; Petrone, A.; Henderson, T.; Ranasinghe, D.; Zakrzewski, V. G.; Gao, J.; Rega, N.; Zheng, G.; Liang, W.; Hada, M.; Ehara, M.; Toyota, K.; Fukuda, R.; Hasegawa, J.; Ishida, M.; Nakajima, T.;

Honda, Y.; Kitao, O.; Nakai, H.; Vreven, T.; Throssell, K.; Montgomery Jr., J. A.; Peralta, J. E.; Ogliaro, F.; Bearpark, M. J.; Heyd, J. J.; Brothers, E. N.; Kudin, K. N.; Staroverov, V. N.; Keith, T. A.; Kobayashi, R.; Normand, J.; Raghavachari, K.; Rendell, A. P.; Burant, J. C.; Iyengar, S. S.; Tomasi, J.; Cossi, M.; Millam, J. M.; Klene, M.; Adamo, C.; Cammi, R.; Ochterski, J. W.; Martin, R. L.; Morokuma, K.; Farkas, O.; Foresman, J. B.; Fox, D. J. *Gaussian 16 Rev. C.01*, Wallingford, CT, 2016.

77. Weigend, F.; Ahlrichs, R., Balanced basis sets of split valence, triple zeta valence and quadruple zeta valence quality for H to Rn: Design and assessment of accuracy. *PCCP* **2005,** *7* (18), 3297-3305.

78. Hanwell, M. D.; Curtis, D. E.; Lonie, D. C.; Vandermeersch, T.; Zurek, E.; Hutchison, G. R., Avogadro: an advanced semantic chemical editor, visualization, and analysis platform. *Journal of Cheminformatics* **2012,** *4* (1), 17.

79. Rappe, A. K.; Casewit, C. J.; Colwell, K. S.; Goddard, W. A.; Skiff, W. M., UFF, a full periodic table force field for molecular mechanics and molecular dynamics simulations. *J. Am. Chem. Soc.* **1992,** *114* (25), 10024-10035.

80. Allouche, A.-R., Gabedit—A graphical user interface for computational chemistry softwares. *J. Comput. Chem.* **2011,** *32* (1), 174-182.

81. Lyon, E. J.; Georgakaki, I. P.; Reibenspies, J. H.; Darensbourg, M. Y., Coordination Sphere Flexibility of Active-Site Models for Fe-Only Hydrogenase: Studies in Intra- and Intermolecular Diatomic Ligand Exchange. *J. Am. Chem. Soc.* **2001,** *123* (14), 3268-3278.

2.7 Appendix

2.7.1 Scan Rate Studies

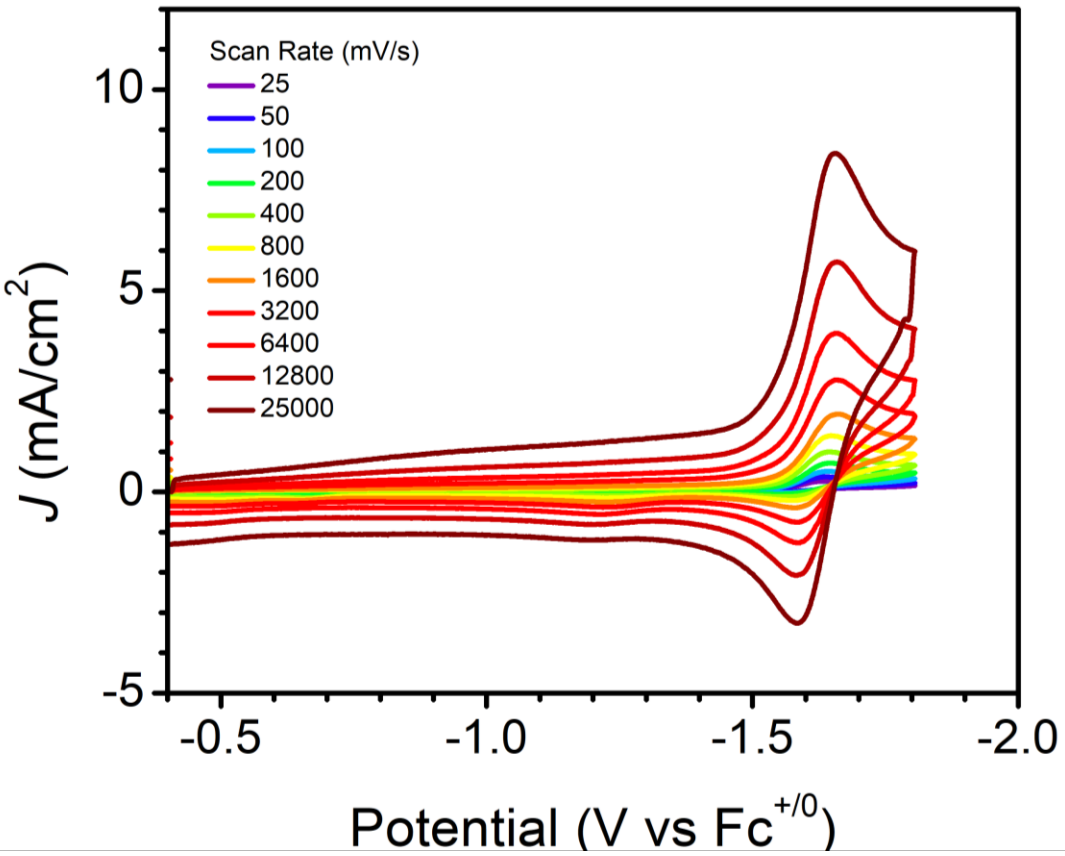

Figure 2.7. CVs of 1mM **1** showing the scan rate dependence of the first reduction. CVs in dry MeCN with 0.1 M $TBAPF_6$ purged with N_2 with a glassy carbon working electrode, Pt wire counter electrode and Ag/AgCl pseudoreference electrode and $Fe(Cp)_2$ as an internal reference.

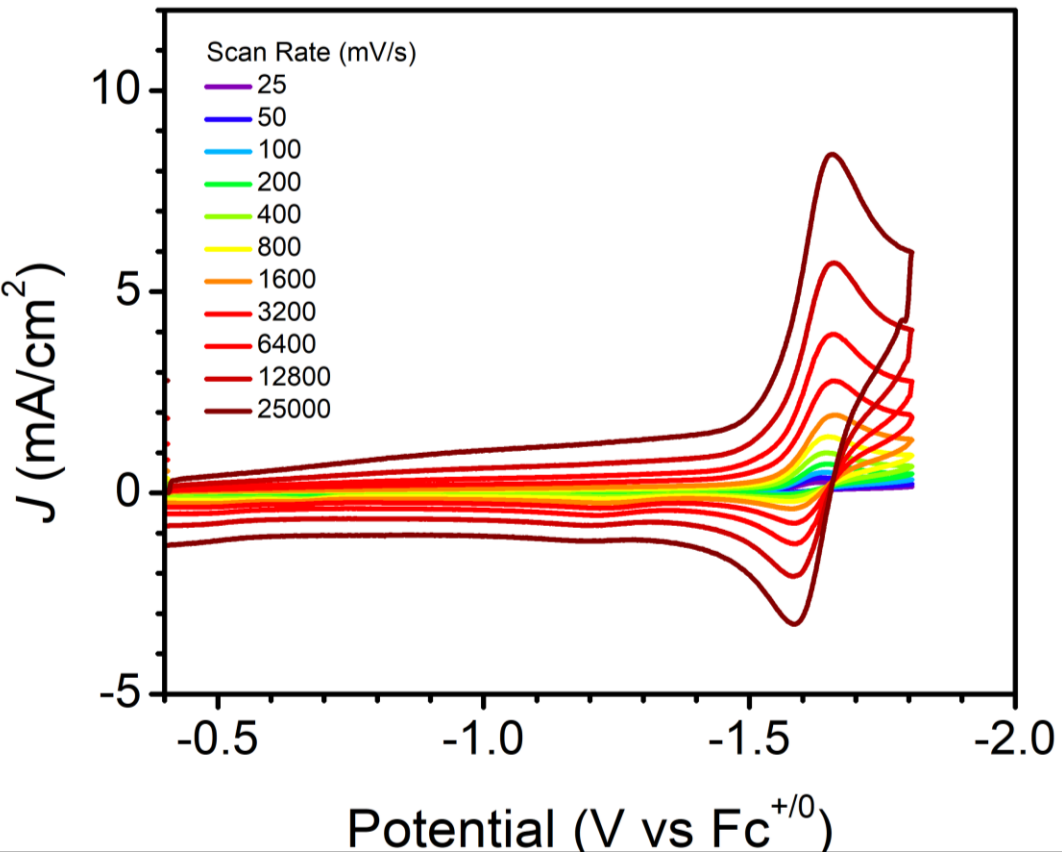

Figure 2.8. CVs of 1mM **1** showing the scan rate dependence of the second and third reduction. CVs in dry MeCN with 0.1 M $TBAPF_6$ purged with N_2 with a glassy carbon working electrode, Pt wire counter electrode and Ag/AgCl pseudoreference electrode and $Fe(Cp)_2$ as an internal reference.

2.7.2 Proton Dependence on CO_2 Reduction

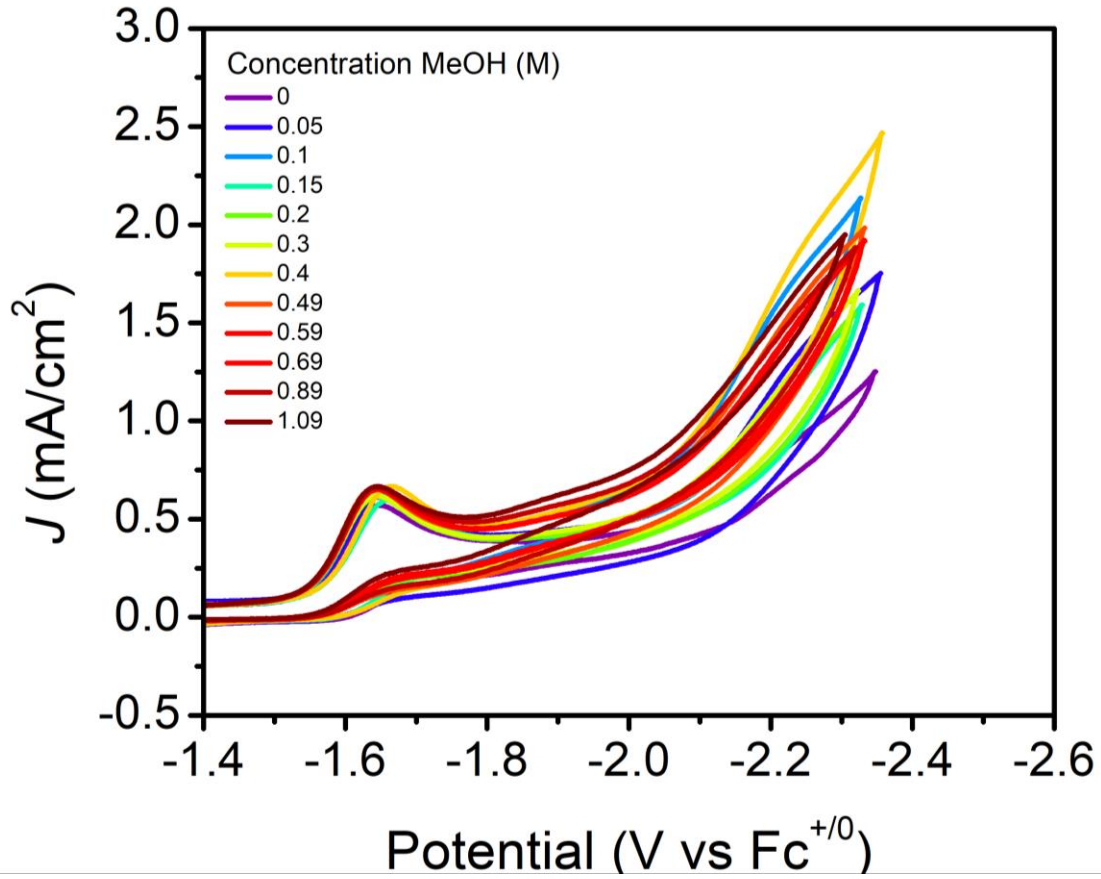

Figure 2.9. CVs of 1mM **1** in dry MeCN with 0.1 M $TBAPF_6$ purged with CO_2 with a glassy carbon working electrode, Pt wire counter electrode and Ag/AgCl pseudoreference electrode and $Fe(Cp)_2$ as an internal reference. MeOH is titrated in between scans, showing a proton dependence

2.7.3 Isotope Dependence on CO_2 Reduction in CV

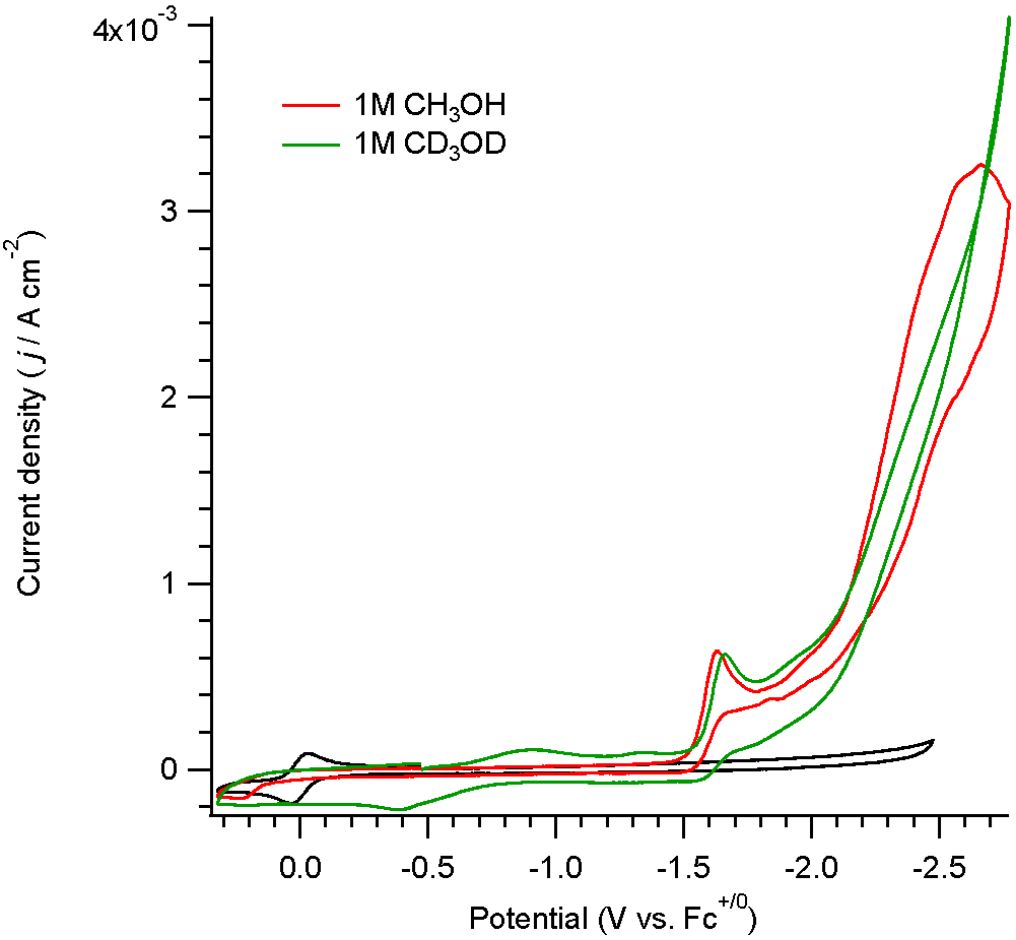

Figure 2.10. CV of 1 mM $Fe_2(pdt)(CO)_6$ in dry MeCN with 1 M MeOH (red) and 1 M CD_3OD (green) in 100 mM $TBAPF_6$ purged with CO_2 with a Ag/AgCl reference electrode, graphite counter electrode and glassy carbon working electrode. Scan rate = 100 mV/s.

2.7.4 Controlled Potential Electrolysis

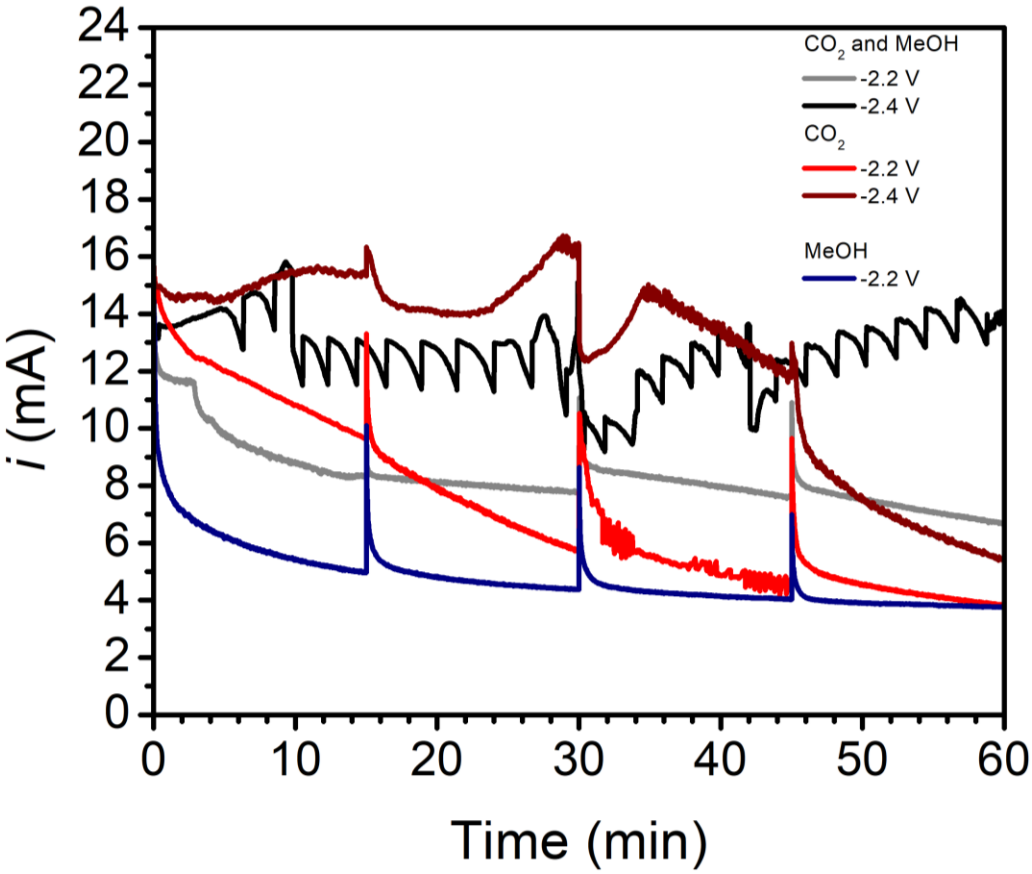

Figure 2.11. CPE of 2 mM $Fe_2(pdt)(CO)_6$ in dry MeCN under CO_2 (red and maroon) with 1 M MeOH (grey and black) and under Ar (blue) with 100 mM $TBAPF_6$ with a Ag/AgCl reference electrode, graphite counter electrode and glassy carbon working electrode. Potentials are reported to versus $Fc^{+/0}$.

2.7.5 Product Analysis of Controlled Potential Analysis

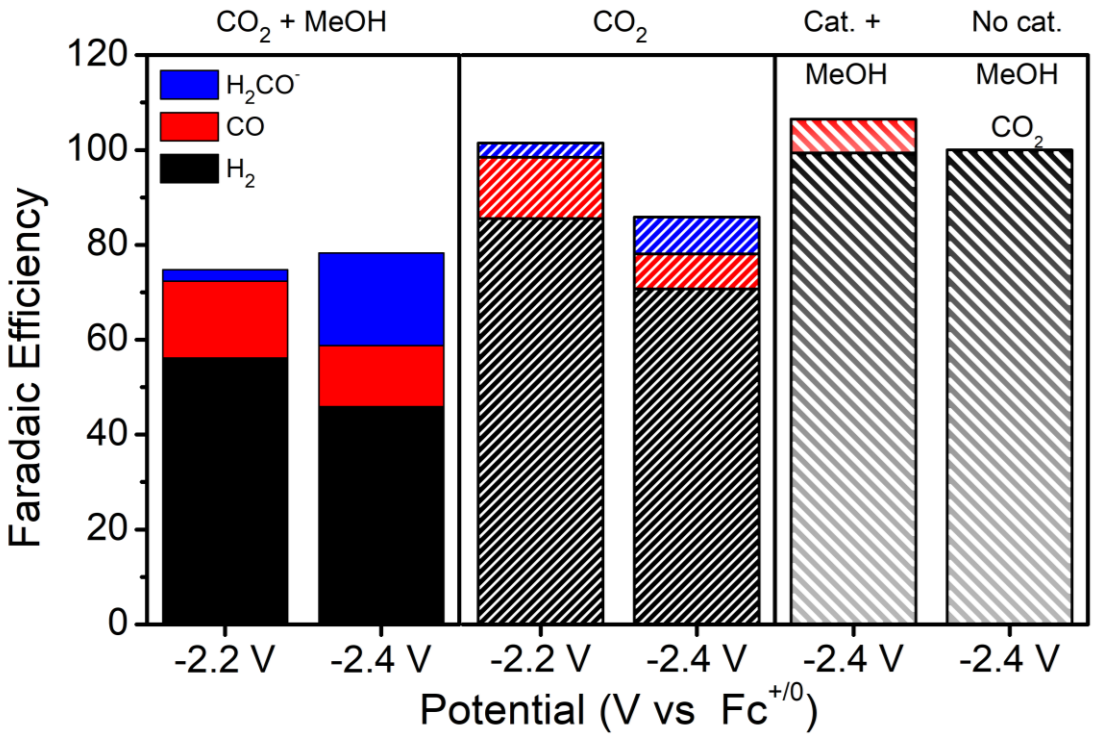

Figure 2.12. Total faradaic yield and selectivity of the products obtained from CPE experiments shown in **Figure 2.11.**

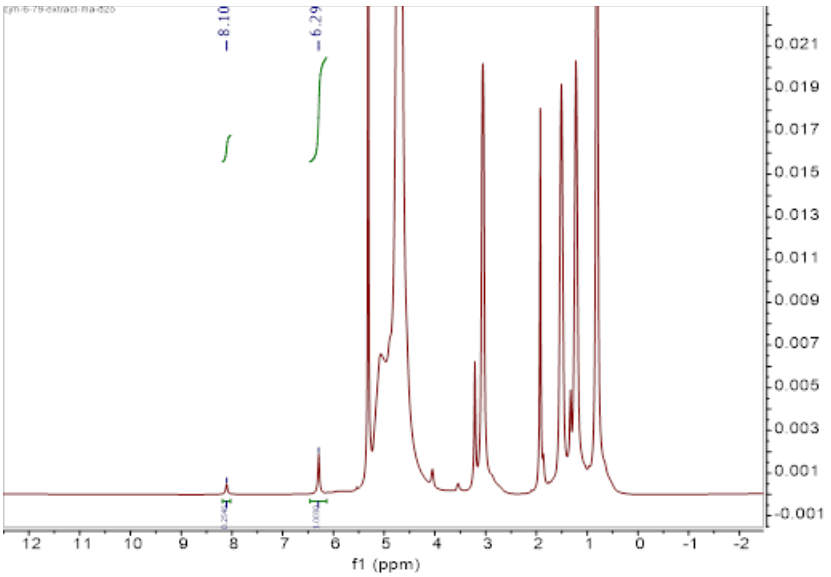

Figure 2.13. 1H NMR following extraction of soluble products formed during NMR. Maleic acid (internal standard) at 6.29 ppm and formic acid at 8.10 ppm are identified.

2.7.6 NMR of products made during CPE

2.7.7 GC trace of CPE headspace

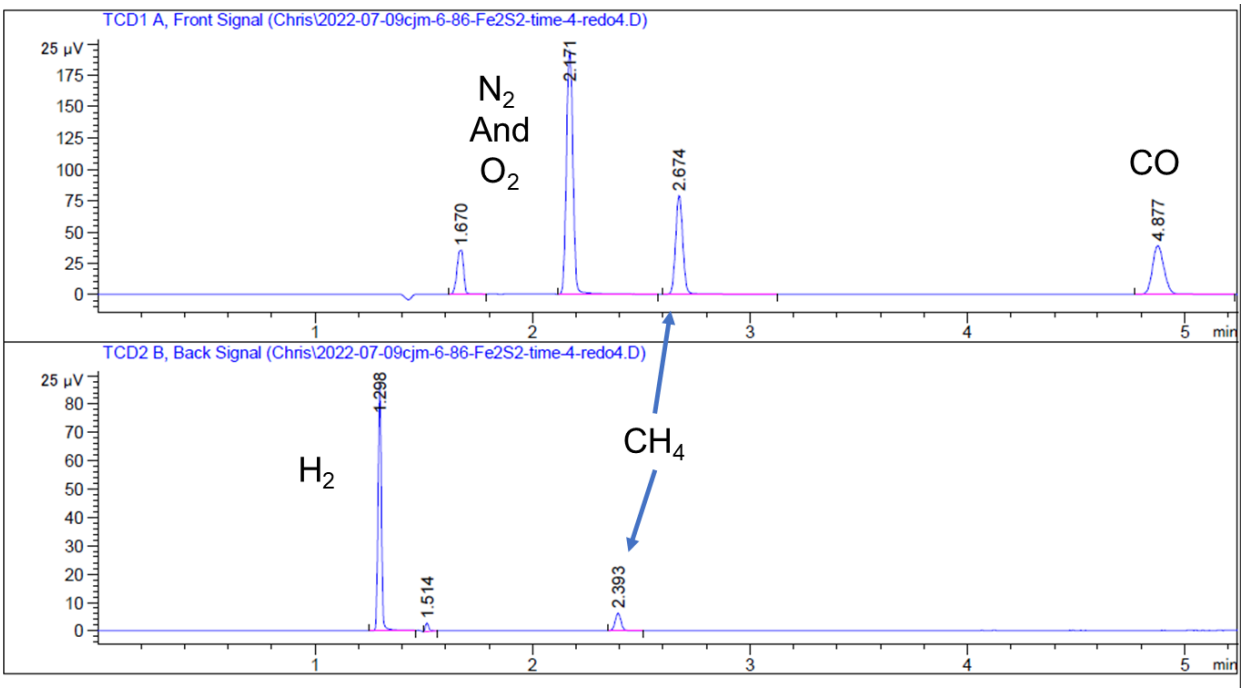

Figure 2.14. Gas chromatogram of headspace during a CPE run of **1** (2 mM) in dry acetonitrile with added MeOH (1 M) sparged with CO_2. The upper trace shows the formation of CO while the bottom shows the formation of H_2. Both traces show CH_4, the internal standard.

2.7.8 General Procedure for Chemical Reductions

In a N_2 filled glovebox, to a solution of **1** (25 mg, 64.8 μmol) in THF (3 mL), a suspension of a slight excess of equivalents of KC8 was added at -40 °C. The mixture was stirred and allowed to warm to room temperature. The mixture was then filtered through celite. The resulting solution was placed in an air-tight IR cell and the resulting spectra was recorded.

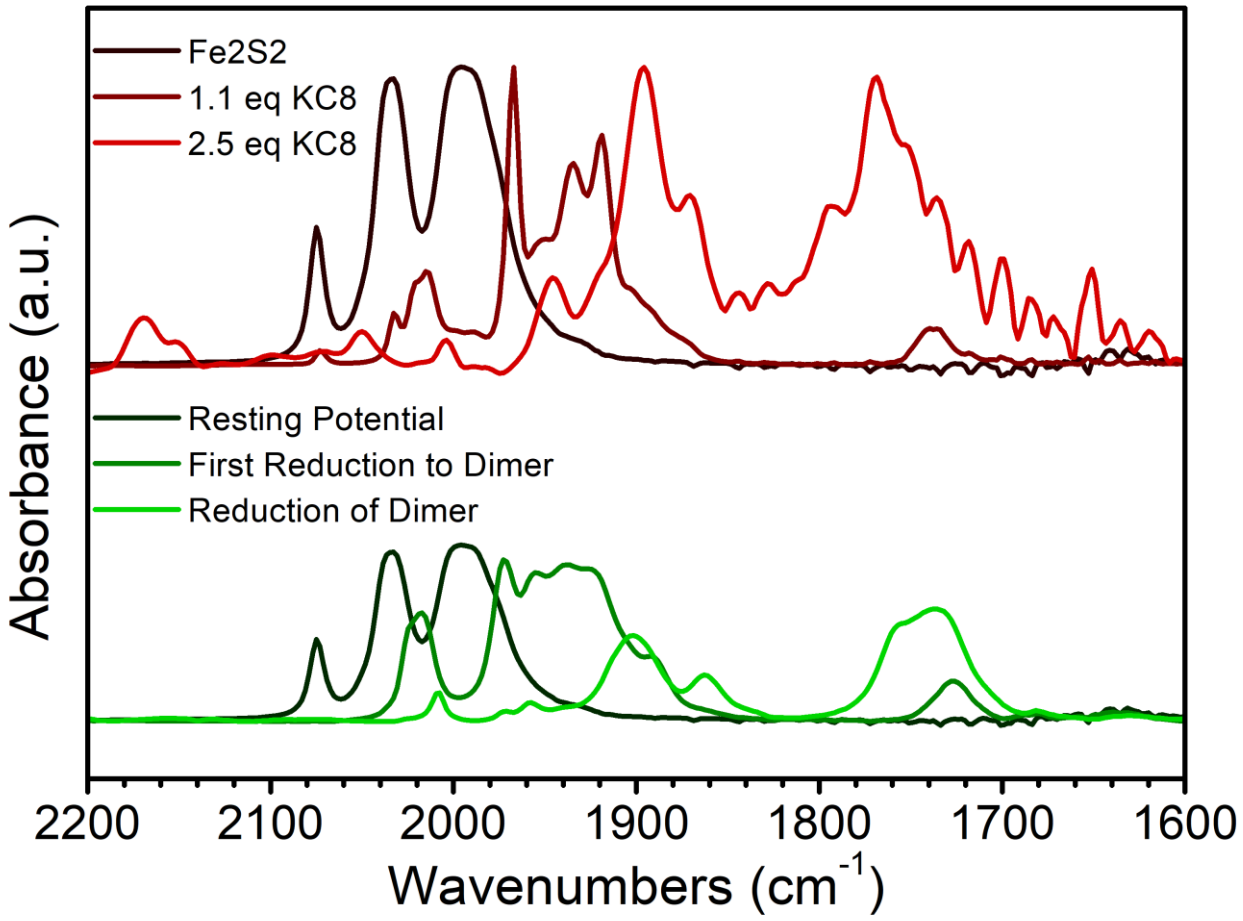

Figure 2.15. FTIR comparing the products made during chemical reductions of **1** with KC8 (red, top) and the products made during electrochemical reductions of **1** (5 mM) in dry acetonitrile with 0.1 M $TBAPF_6$

2.7.9 Scan of different potentials using IR-SEC

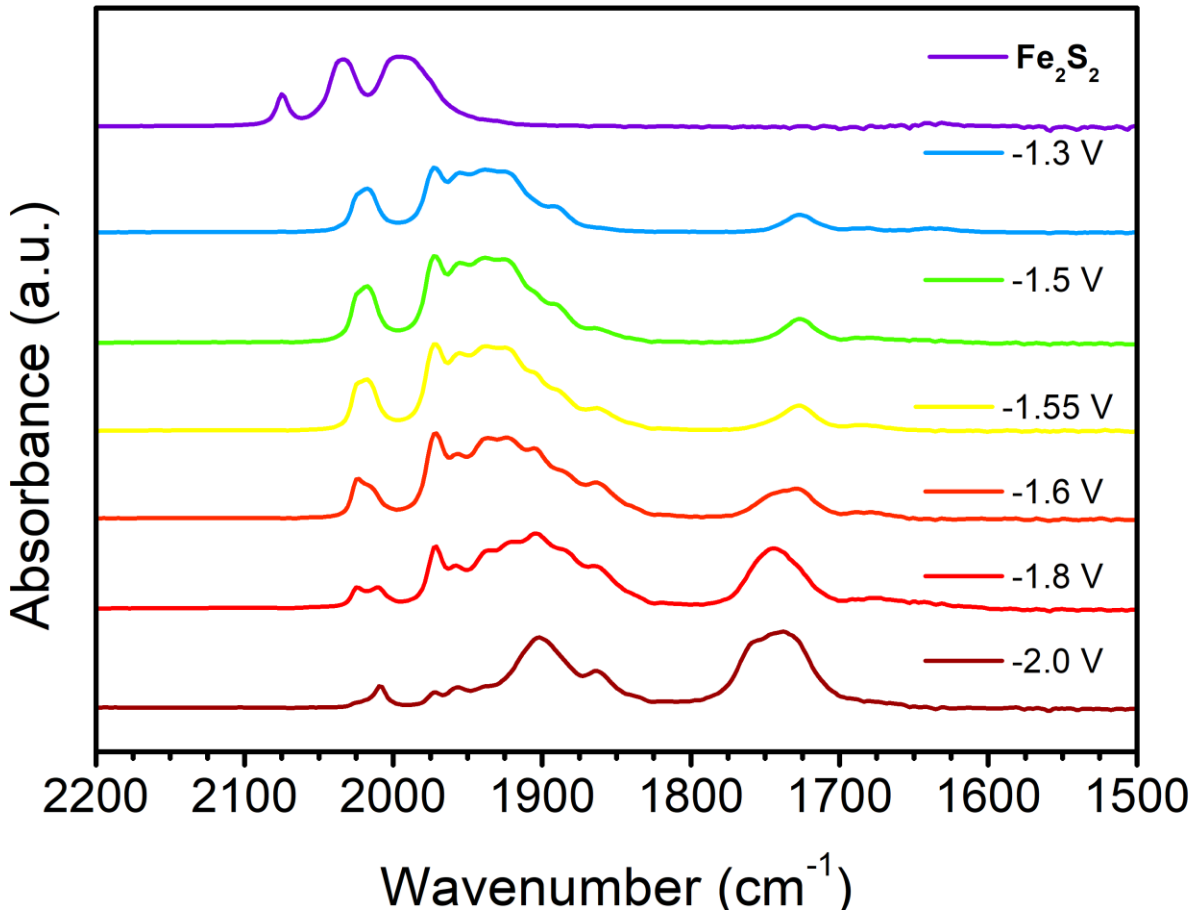

Figure 2.16. IR-SEC of **1** (5 mM) in dry acetonitrile with 0.1 M $TBAPF_6$ at different applied potentials (vs Ag/AgCl). The graph shows the formation of the peak at 1735 cm^{-1}, identified as $[Fe(CO)_4]^{2-}$ begins at -1.6 V vs Ag/AgCl and grows as more applied potential is applied.

2.7.10 Time dependence on IR-SEC

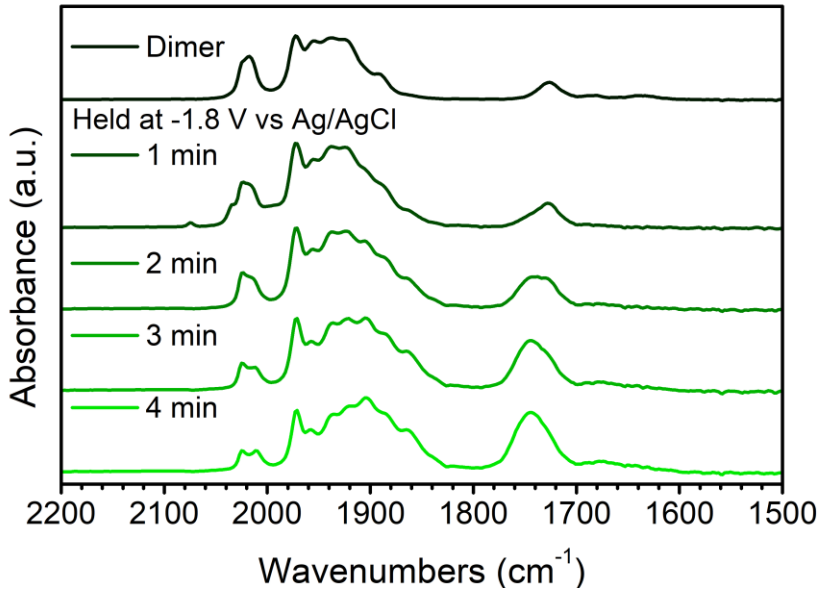

Figure 2.17. Time dependence on the conversion of the dimer, **2** (5 mM in dry acetonitrile with 0.1 M $TBAPF_6$), to products **2***, **3**, and **4** at -1.8 V vs Ag/AgCl via IR-SEC.

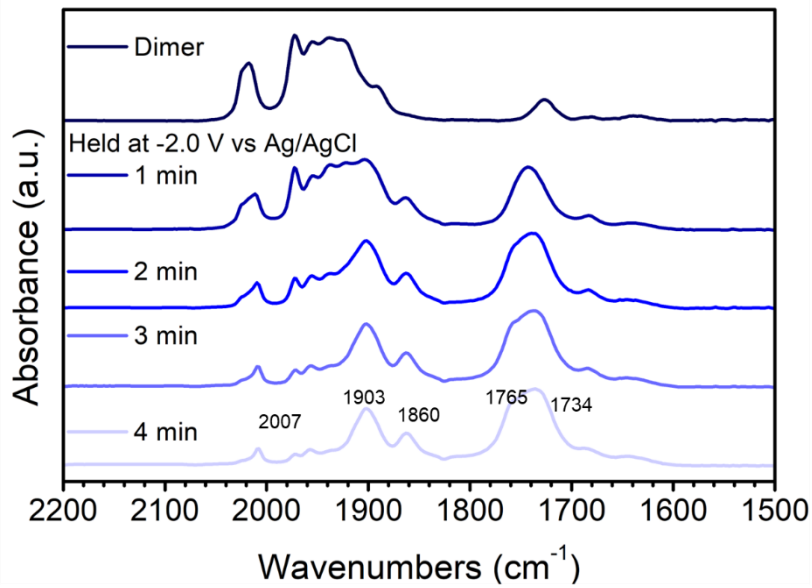

Figure 2.18. Time dependence on the conversion of the dimer, **2** (5 mM in dry acetonitrile with 0.1 M $TBAPF_6$), to products **2***, **3**, and **4** at -2.0 V vs Ag/AgCl via IR-SEC.

2.7.11 IR-SEC under Ar with 1 M MeOH

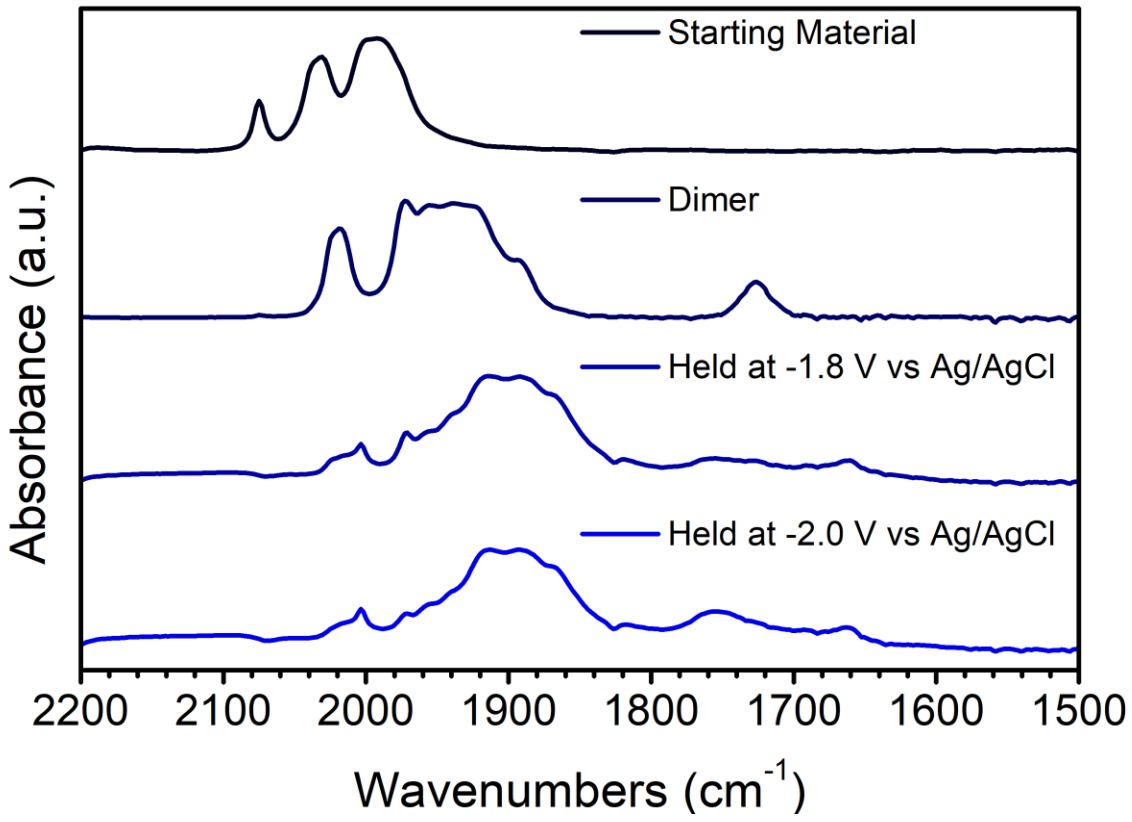

Figure 2.19. IR-SEC of 5 mM of 1 in dry MeCN with 0.1 M TBAPF6 and 1 M MeOH purged with Ar.

When MeOH is added, the bands formed after the second and third reduction due to the onset of catalytic activity. When the applied potential is held just past the second reduction (-1.8 V vs Ag/AgCl, ~ -2.2 V vs $Fc^{+/0}$), there are minor bands that are formed at 2003 cm^{-1}, 1889 cm^{-1}, 1867 cm^{-1}, 1752 cm^{-1}, and 1662 cm^{-1} (Figure 2.19). The first four of these bands are similar to those found in the after the third reduction (-2.0 V vs Ag/AgCl, ~ -2.4 V vs $Fc^{+/0}$) in the absence of proton source. As this is a bulk technique, it is likely that the compound corresponding to these bands are either the slow step in the reactivity with MeOH or inactive towards methanol and the peak at 1741 cm^{-1} corresponds to a compound that reacts with MeOH. When the applied potential

is increased beyond the third reduction, the band at 1970 cm^{-1} decreases in intensity as the band at 1752 cm^{-1} increases. The increase in intensity of the band at 1752 cm^{-1} matches that of the increase in intensity of the band formed after the third reduction of **1** in the absence of proton source.

2.7.12 Possible Intermediates Used in DFT Study

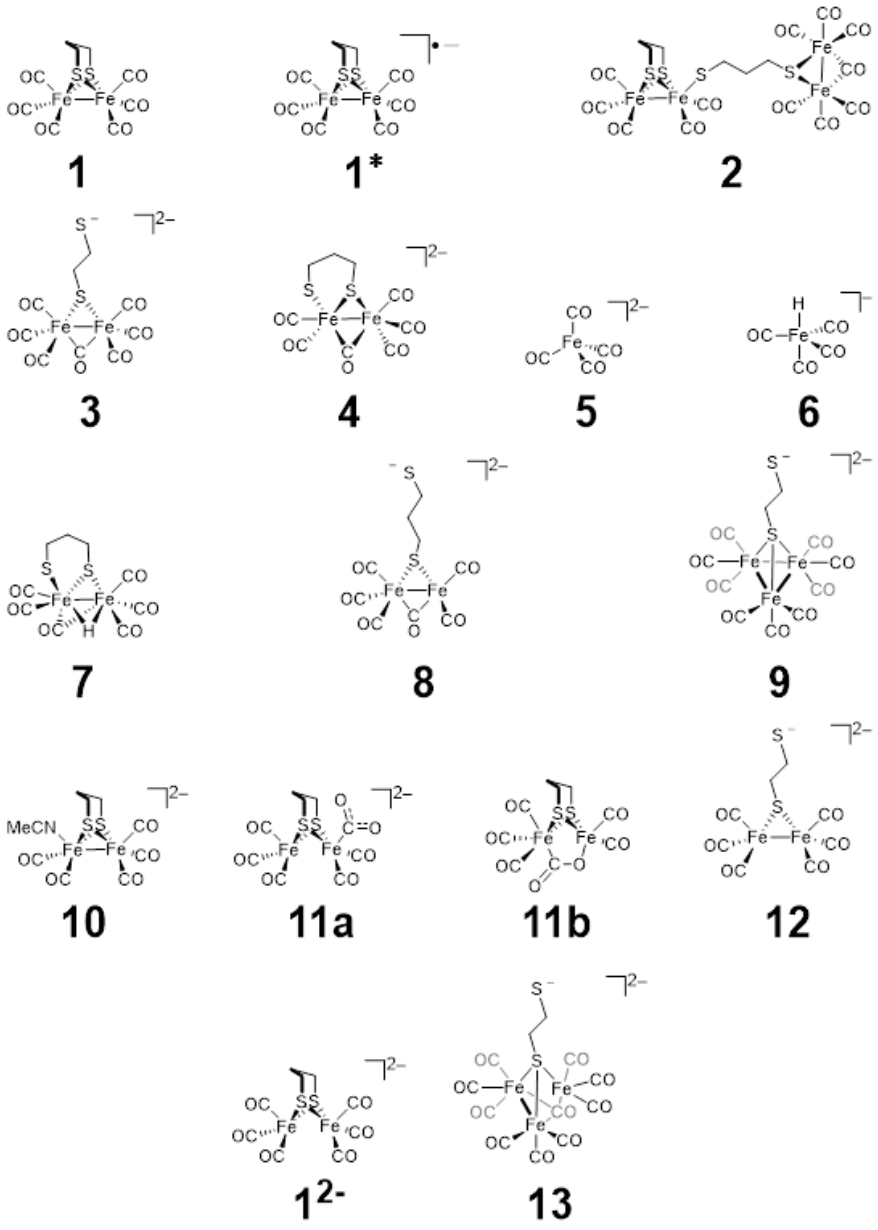

Figure 2.20. The hypothesized structures of the compounds formed under catalytic conditions that were used in the initial DFT screening.

2.7.13 DFT Computed FTIR of Potential Structures

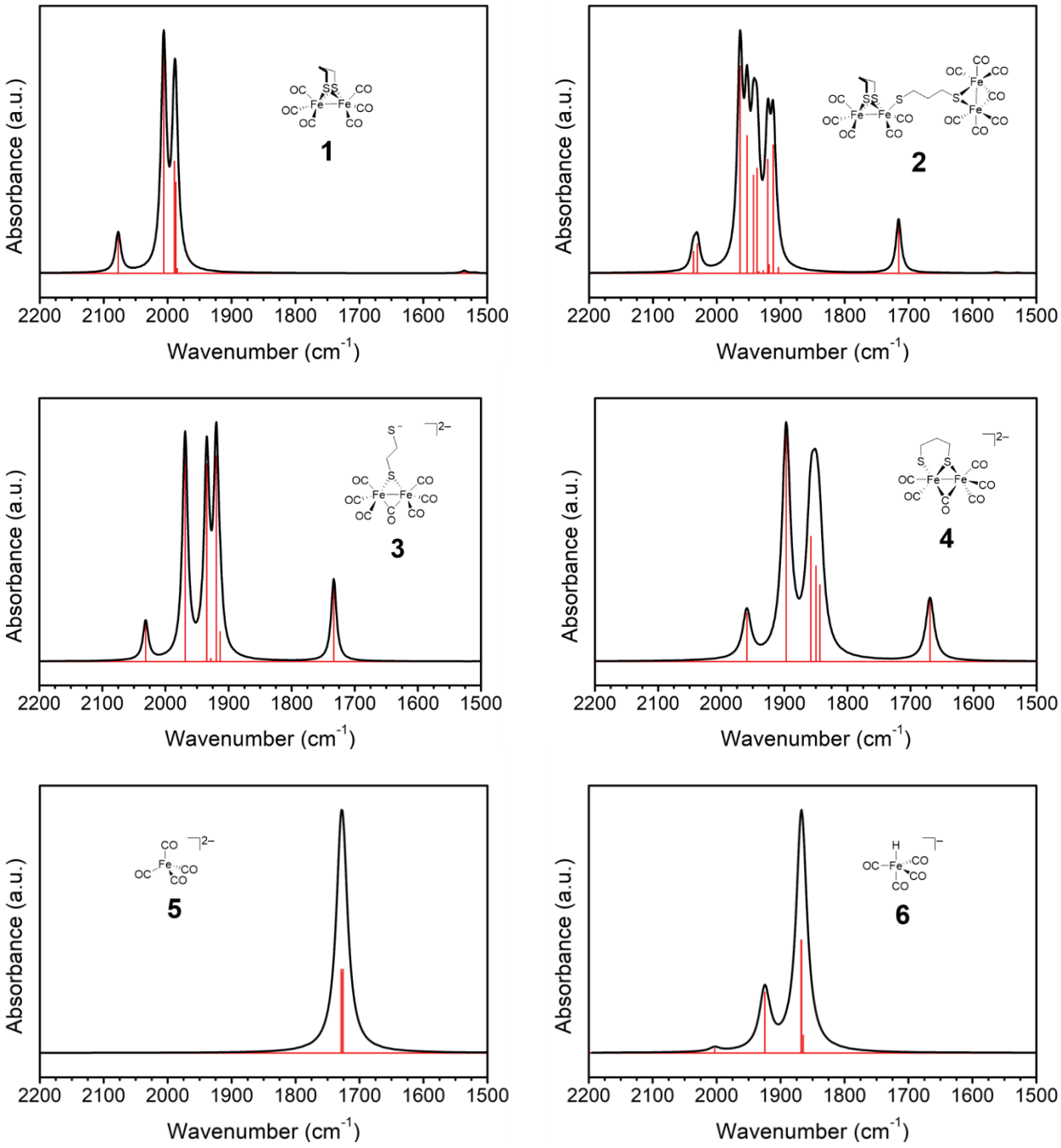

Figure 2.21. DFT determined structures of 1-6 TPSSH functional with the Def2-TZVP basis set utilizing a polarizable continuum model (PCM) with acetonitrile as the solvent.

CHAPTER 3. Hydricity as a Guide in H_2 Evolution, Formic Acid Decomposition, and Transfer Hydrogenation: A Case Study with Ir(Cp*)(2-phenylpyridine)H

3.1 Introduction

Transfer hydrogenation (TH) is one of the fundamental catalytic transformations in organometallic chemistry with applications ranging to pharmaceuticals to fuels to food.[1-3] This reaction can be run in the absence of H_2 gas, using safe, readily available, and inexpensive sources.[1] There is a wide scope to the reaction, with catalysts optimized to reducing ketones,[4-9] imines,[10-13] olefins,[14-16] and CO_2,[17] with low loadings and high turnover frequencies.

The mechanism of TH involves three key steps (Figure 3.1). First, a hydride is transferred from the hydrogen carrier, (e.g. as formate), to the organometallic catalyst. From this point, the reaction can proceed in one of two ways. To complete the TH catalytic cycle, the metal hydride

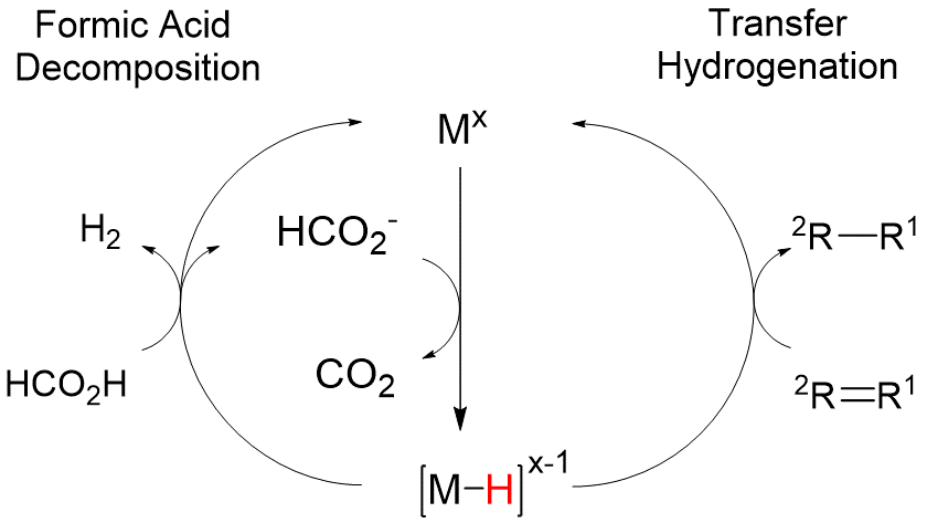

Figure 3.1. The generic mechanistic steps for formic acid decomposition and transfer hydrogenation.

will transfer to the substrate, such as an olefin. This transfer is quickly followed by protonation of the substrate to produce the reduced, hydrogenated product.[18] However, the metal hydride may instead react directly with the proton source, forming H_2 gas, and thus completing a separate reaction pathway known as formic acid decomposition.[19-21] The thermodynamic ability for a substrate to donate a hydride, known as hydricity, gives chemists a tool to understand and predict these transformations and can provide insights into new catalytic designs.[22-23]

Herein, we determine the hydricity of Ir(Cp*)(ppy)(X) (where X = Cl, H) in MeCN and predict the subsequent reactivity in the transfer hydrogenation of cyclohex-2-en-1-one using tetrabutylammonium formate formic acid ($[Bu_4N][HCO_2^-]_2H$) as the hydrogen source. The kinetics and selectivity of these processes are then explored. This work provides a thermodynamic bases for transfer hydrogenation and formic acid decompositions and provides insights into future catalyst design.

3.2 Results and Discussion

3.2.1 Thermodynamics of Cl^- Dissociation

A general method in transfer hydrogenation literature is the use of a precatalyst.[1, 3] For improved stability in air and ease of handling, the use of a labile ligand, such as a halide, in transfer hydrogenation, precatalysts are ubiquitous. While it is rarely mentioned, the use of a precatalyst has an energetic cost associated with it, that may have consequential effects on the catalytic activity. To determine the thermodynamic penalty for this catalyst, the equilibrium of Cl^- binding was determined. This was done by the titration of **Ir-MeCN** in dry MeCN-d_3 with $[Bu_4N][Cl]$, with the equilibrium determined by ^1H NMR. Using the $[Bu_4N]^+$ hydrogen atoms as an indirect measurement for the total Cl^- added to the solution and the Cp* signals to determine the ratio of **Ir-Cl** and **Ir-MeCN**. The conversion of **Ir-MeCN** to **Ir-Cl** was immediate in the presence of added

[Cl^-]. Following the determination of **Ir-MeCN** to **Ir-Cl** concentrations at seven different concentrations of added Cl, the $\Delta G°_{Cl\ dissocn.}$ was determined to be 1.6 ± 0.5 kcal/mol.

3.2.2 Thermodynamic Hydricity of Ir(Cp*)(ppy)H

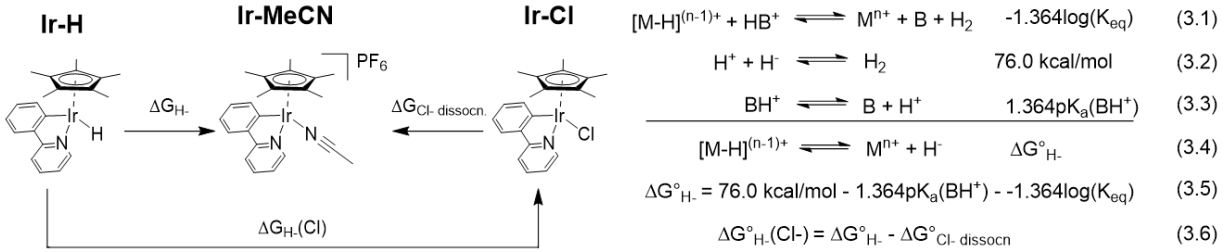

Figure 3.2. The structure of Ir-H, Ir-MeCN, and Ir-Cl as well as the relevant reactions between them (left). The relevant equations for the determination of the thermodynamic hydricity of **Ir-H** and apparent hydricity of **Ir-Cl** through the H_2 heterolysis method.

The key steps in TH and formic acid decomposition depend on the ability of the catalyst to donate a hydride. The thermodynamic ability of a substrate to donate a hydride, known as hydricity ($\Delta G°_{H-}$), is essential for understanding this step. To accurately determine the energetics to enter the TH cycle, both the hydricity (Equation 3.4) and apparent hydricity (Equation 3.6) must be determined. This can be done via several methods. The potential-pK_a method proved inconclusive, as **Ir-H** was stable in MeCN, even upon the addition of the strong base, NaOMe, dissolved in *t*-BuOH. Instead, hydricity was determined via the H_2 heterolysis method, utilizing Et_3N as the base. Due to previous reports of the **Ir-H** reacting with Ag^+ to from a trimetallic-dihydride species,[24] the chloride in **1-Cl** was extracted using an excess of $NaPF_6$ in dry $MeCNd_3$ under N_2 to form **Ir-MeCN-d$_3$**. The resulting NaCl was filtered off prior to hydricity determination. To determine the equilibrium of H_2 heterolysis, a total of four reactions were run in parallel with varying mixtures of Et_3N:[Et_3NH][PF_6] added to an NMR tube containing **Ir-MeCN-d$_3$** in dry MeCN-d_3. Following the addition of 1 atm of H_2, ^{1}H NMR determined the equilibrium was achieved after 48 h. The ratio of **Ir-H** and **Ir-MeCN** was determined via integration of the Cp* signals in the NMR. The equilibrium constant was determined to be 15±8 atm. By substituting this value into Equation 3.1,

with the pK_a of Et3N in MeCN (18.83),[25] and value obtained in Equation 3.5, the hydricity of **Ir-H** was determined to be 48.8 ± 0.2 kcal/mol. In context, **Ir-H** is more hydridic than [Ir(Cp*)(2,2'-bipyridine)H]$^+$ (62.0 kcal/mol). The difference of 13.2 kcal/mol shows the relative difference the change in ligand and overall charge of the complex can make on the hydricity. In addition, the complex is slightly more hydridic ($\Delta\Delta G°_{H-} = 0.8$ kcal/mol) than the isoelectric Rh(Cp*)(ppy)H. When the binding of Cl is considered, the apparent hydricity for **Ir-H** going to **Ir-Cl** can be determined. By combining $\Delta G°_{Cl\text{- dissocn}}$ with the determined hydricity, the apparent hydricity, $\Delta G°_{H-}$(Cl), was determined to be 47.2 kcal/mol.

3.2.3 Formic Acid Decomposition

The determination of the two hydricity values of **Ir-H** allows for the prediction of the reactivity of catalyst with the hydrogen source, $[Bu_4N][HCO_2]_2H$ for the formic acid decomposition pathway. First, both $\Delta G°_{H-}$(MeCN) and $\Delta G°_{H-}$(Cl) are less hydridic than formate ($\Delta G°_{H-} = 44$ kcal/mol in MeCN),[26] therefore, the transfer of the hydride from formate to the catalyst is favored (Figure 3.2). Experimentally, when either **Ir-MeCN** or **Ir-Cl** is added to a solution containing $[Bu_4N][HCO_2]_2H$ in dry MeCN-d_3 at room temperature, the formation of **Ir-H** can be detected by NMR in less than 1 hr. However, at this temperature, the reaction is slow, and the yield is minimal. When the reaction is run at 80°C, there is significant detection of CO_2 in the headspace via FTIR after 2 h.

Once **Ir-H** is formed, the next step in the catalytic cycle is the subsequent protonation of the **Ir-H** to form H_2. This step is not only dependent on the hydricity of the metal hydride but the strength of the acid in solution. For this experiment, the pK_a of HCOOH is 20.9 in MeCN.[27] Using Equation 3.1, the driving force for the protonation of **Ir-H** to form H_2 is unfavorable, with $\Delta G°_{H2\text{ formation}} = 1.5$ kcal/mol. When this reaction is tracked by NMR at room temperature using either the

Ir-Cl or **Ir-H**, there is some formation of H_2 gas after 24 h. Interestingly, when starting with the **Ir-Cl**, only the starting material and **Ir-H** are detected, with no detectable **Ir-MeCN**. When the starting material is **Ir-H**, the only change in the NMR over the reaction is the production of a H_2

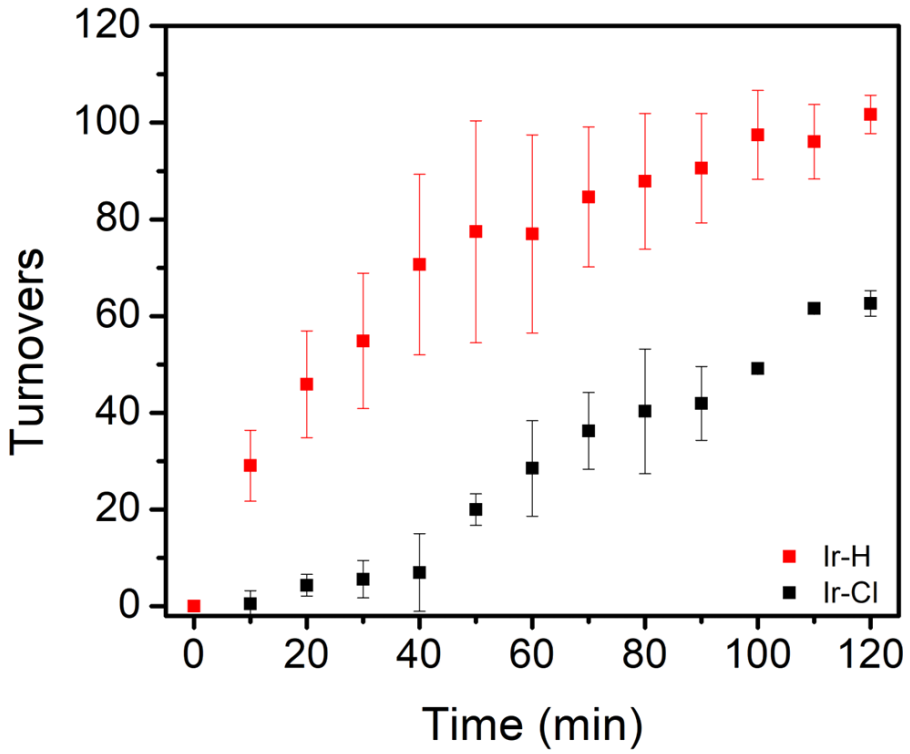

Figure 3.3. The turnover number over time of the decomposition of formic acid to CO_2 and H_2 using **Ir-H** (red) and **Ir-Cl** (black).

peak at 4.4 ppm. This indicates things about the kinetics for formic acid decomposition. First, the presence of **Ir-Cl** after 24 h, indicates that, in addition to thermodynamic barrier of Cl^- dissociation, there is also a kinetic barrier that hinders the overall turnover rate of the catalyst. Second, the buildup of **Ir-H** with no detectable **Ir-MeCN** indicates that the rate limiting step in the turnover of the catalyst for formic acid decomposition is the protonation of the **Ir-H** rather than the transfer of the hydride from formate to Ir.

To further investigate the change in rate the addition of the Cl had on the catalyst, the formic acid decomposition was studied at 80°C and the turnover frequency was determined via gas measurement (Figure 3.3). Using 1% catalyst loading of **Ir-Cl**, the turnover frequency (TOF)

for the formic acid decomposition after 2 h was determined to 28 h^{-1}. When the experiment is rerun starting with **Ir-H**, the turnover frequency almost doubles (TOF = 50 h^{-1}) (Figure 3.3). By using a combination of GC and FTIR, it was determined that the Ir catalyst was selective for formic acid decomposition, with no detection of any dehydration products (CO and H_2O). Additionally, for the **Ir-Cl** catalyst, the turnover number (TON) over time is not linear. There appears to be an onset time due to the TON after 30 minutes being only 6.2 ± 3.9, which clearly indicates that the loss of Cl is an initial barrier to catalysis.

3.2.4 Hydrogen Evolution

Since the kinetics obtained during formic acid decomposition consisted of both the oxidation of formate to produce **Ir-H** and CO_2 and the subsequent protonation of the hydride to form H_2, a different method was required to investigate the kinetics involved in the thermodynamically uphill, second step of the formic acid decomposition pathway. To do this,

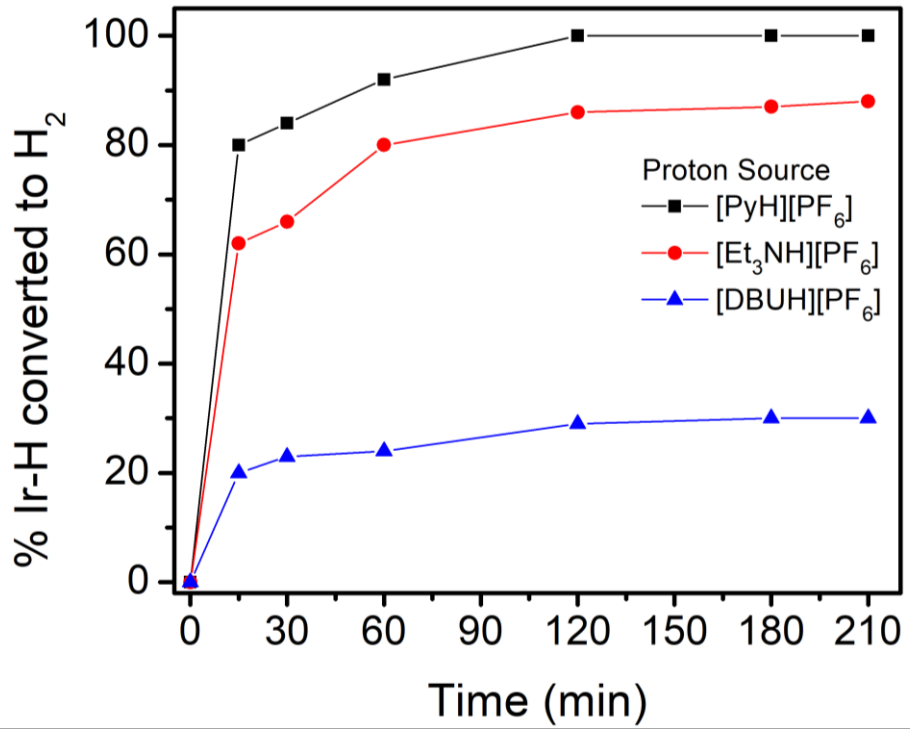

Figure 3.4. The conversion of Ir-H to H_2 as determined from NMR upon the addition of a slight excess (1.1 eq total added, 10% excess) of a proton source with a known pK_a in MeCN.

^{1}H NMR was used to determine the reactivity of **Ir-H** with several acids of known pK_as in MeCN. Specifically, a slight excess (1.1 eq total added, 10% excess) of a known acid was added to an NMR tube containing **Ir-H** and the ratio of **Ir-H**:**Ir-MeCN** was tracked over the space of 4 h. Figure 3.4 shows that a stronger acid corresponds with faster H_2 evolution. In this case, the thermodynamic driving force seems to influence the overall rate. When this is considered along with the NMR studies, the rate of formic acid decomposition by the Ir(Cp*)(ppy)(X) catalyst is limited by H_2 evolution.

Table 3.1 The pK_a and driving force for H_2 evolution using Equation 3.2 for the acids used in Figure 3.3

	[DBU-H][PF$_6$]	**[HNEt$_3$][PF$_6$]**	**[C$_5$H$_5$NH][PF$_6$]**
pK_a	24.31	18.83	12.53
$\Delta G°_{H2}$ with Ir-H (kcal/mol)	6.1	-1.3	-9.9

The determination of the rate limiting step provides several insights into future catalytic optimizations for formic acid decomposition over transfer hydrogenation. First, in MeCN, for both $HCOO^-$ oxidation and subsequent H_2 evolution to be thermodynamically favored with the current **Ir-H** catalyst, the pK_a of the acid must be below 19.94. However, if the hydrogen source remains $[Bu_4N][HCO_2]_2H$, then the hydricity of the metal hydride must be between 44 and 47.5 kcal/mol, leading to a loss in thermodynamic driving force for the oxidation of $HCOO^-$. Additionally, the sluggish H_2 evolution allows for utilization of the **Ir-H** and $[Bu_4N][HCO_2]_2H$ in an efficient transfer hydrogenation system.

3.2.5 Transfer Hydrogenation of 2-cyclohexen-1-one

The determination of the hydricity of **Ir-H** also can be used to gain some insight into the TH of alkenes and ketones in MeCN. One TH substrate of interest is 2-cyclohexen-1-one, as it contains both a ketone and a C=C double bond, both of which can be hydrogenated. While the hydricity has not been directly measured for 2-cyclohexen-1-one in addition to most alkenes and ketones, the hydride affinity ($\Delta H°_{H-}$) of several similar compounds has been measured in MeCN. This hydride affinity provides insight into the possible selectivity of the TH reaction. Hydride affinity

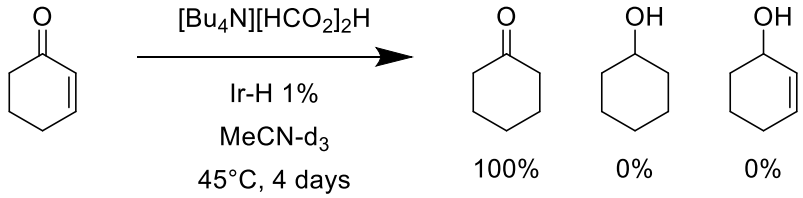

Figure 3.5. The conditions and product selectivity for the NMR scale transfer hydrogenation of 2-cyclohexen-1-one by Ir-H.

is defined as the enthalpy change during the reaction of an unsaturated bond with a free hydride ion to form the subsequent carbanion.[28] In MeCN, the $\Delta H°_{H-}$ of ketones ($\Delta H°_{H-}$ between -30 and -45 kcal/mol),[29] are less energetically favorable to reduce than alkenes ($\Delta H°_{H-}$ between -50 and -65 kcal/mol).[30] This difference allows for the prediction that in a TH setup with **Ir-H**, as the first hydrogenation product should be cyclohexanone rather than cyclohex-2-en-1-ol. Additionally, if the Ir-H is strong enough, it can further reduce cyclohexanone to form cyclohexanol.

To determine the experimental hydrogenation selectivity of **Ir-H** in solution, TH using $[Bu_4N][HCO_2]_2H$ as the hydrogen source was monitored via NMR. By monitoring the reaction at lower temperatures (45°C), NMR determines that the only hydrogenation product is cyclohexanone, achieving full conversion from 2-cyclohexen-1-one after 4 days. In addition, H_2 is detected, showing that while H_2 was slow, the kinetics of the TH were not fast enough to outpace H_2 evolution entirely.

To understand how the formic acid decomposition pathway was affected upon the addition of a TH substrate, the gas evolution was monitored in an identical set up to formic acid decomposition. One might expect the overall rate for gas evolution to be slower from the addition

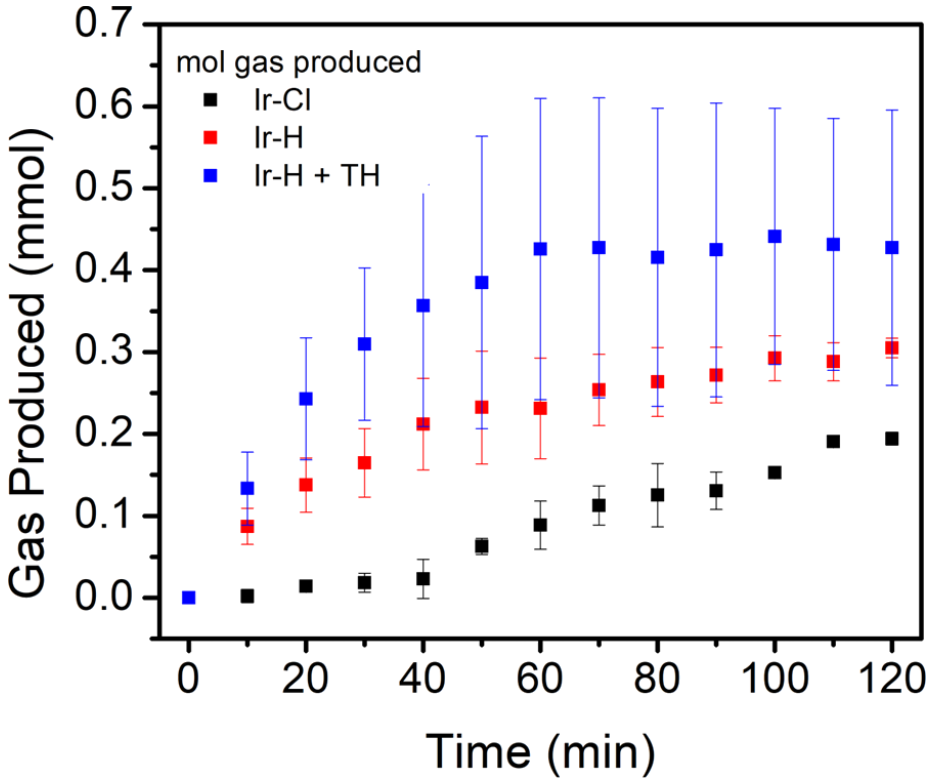

Figure 3.6. The moles of gas produced over time during formic acid decomposition with **Ir-H** (red), **Ir-Cl** (black) and during the TH of 2-cyclohexen-1-one.

of a TH substrate due to the utilization of the hydrogen in TH rather than H_2 evolution, but this is not the case. In fact, the overall rate of gas evolution outpaces formic acid decomposition, leading to clear plateau after one hour due to the overall depletion of $[Bu_4N][HCO_2]_2H$. Product analysis reveals that while the reaction remains selective for hydrogenation of the alkene to form cyclohexanone, the yield is significantly lower (25% conversion). While the overall rate of gas formation increased, the yield indicates that there is still a significant amount of H_2 production. This illustrates that though hydrogen evolution is the slow step in formic acid decomposition, the kinetics for TH are still slower, indicating a larger kinetic barrier for TH than for H_2.

3.3 Conclusion

The determination of the thermodynamic hydricity and apparent hydricity of Ir(Cp*)(ppy)X (where X = Cl, H) has been shown to provide insight into the mechanisms involved in formic acid decomposition and TH. Using these insights, two slow steps in catalysis were identified, Cl^- dissociation and H_2 evolution. By substituting the Cl^- for a H^- ligand, the rate for formic acid decomposition improved significantly. Additionally, we have shown that H_2 evolution is a thermodynamically uphill process and controlled by the pK_a of the formic acid, proposing several methods to increase the react of the catalytic reaction. Furthermore, we showed how hydricity and hydride affinity can be used to predict product formation in the TH of 2-cyclohexen-1-one. Finally, we showed that while there is a large enthalpic driving force for the transfer of a hydride to 2-cyclohexen-1-one to form cyclohexanone, the kinetic barrier is larger than that for the thermodynamically uphill H_2 evolution reaction. Overall, this underscores the strength of hydricity in understanding formic acid decomposition and TH and provides insights into future catalytic designs and strategies.

3.4 Methods and Materials

3.4.1 General Considerations

^{1}H NMR were recorded on a JOEL 500 MHz or 400 MHz spectrometer. The ^{1}H Chemical shifts are referenced to deuterated solvent peaks and reported relative to TMS ($\delta = 0$). Transmission spectra of the headspace of the formic acid decomposition reaction were acquired on a Thermo Scientific Nicolet 6700. Spectra were average over 32 scans at a 0.25 cm^{-1} resolution. Solvents were received from Fisher Scientific and were dried on a custom solvent system (degassed with Argon and dried over alumina columns) and stored over 3 Å sieves. Deuterated solvents were obtained from Cambridge Isotope Laboratories. **Ir-Cl**,[31] **Ir-H**,[24] **Ir-MeCN**,[32] $[Bu_4N][HCO_2]_2H$,[33]

triethylammonium hexafluorophosphate ($[Et_3NH][PF_6]$),[34] protonated 1,8-Diazabicyclo(5.4.0)undec-7-ene hexafluorophosphate ($[DBUH][PF_6]$),[34] and pyridinium hexafluorophosphate ($[PyH][PF_6]$),[34] were made via literature methods. All other reagents were obtained from commercial sources and used without further purification. Where stated, reactions under nitrogen atmosphere were performed using standard Schlenk-line and glove box techniques. Gas samples were analyzed on a Hewlett-Packard 7890A Series Gas Chromatogram with two molseive columns (30m × 0.53 mm i.d. × 25 μm film).

3.4.2 Determination of Cl^- dissociation equilibrium

In a N_2 filled glove box, to vial containing **Ir-Cl** (2.15 mg, 4.16 μmol, 1.0 eq) and 1,2,4,5-tetramethylbenzene (2.0 mg, 14.90 μmol, NMR internal standard) in 1 mL of dry MeCN-d_3, $AgPF_6$ (1.06 mg, 4.20 μmol, 1.01 eq) was added. The solution was mixed until the formation of a precipitate (AgCl) and subsequent color change from vibrant yellow to pale yellow (1 minute). The solution was then filtered over a celite plug to remove the precipitate and added to an NMR tube. NMR was run to confirm the full conversion of **Ir-Cl** to **Ir-MeCN-d$_3$**. 20 μL of a stock solution containing of 45 mM $[Bu_4N][Cl]$ in dry MeCN-d_3 was added to the NMR tube and the solution was allowed to come to equilibrium (30 min) and using the 1,2,4,5-tetramethylbenzene as an internal standard and the $[Bu_4N^+]$ as a proxy for $[Cl^-]$, the equilibrium was determined between **Ir-Cl** and **Ir-MeCN-d$_3$**. The addition and equilibration were then repeated 6 additional times. The resulting equilibrium constant for Cl^- dissociation was determined to be 0.06 ±0.02 and the $\Delta G°_{Cl^- \text{ dissociation}}$ was determined to be 1.6 ± 0.5 kcal/mol.

3.4.3 General Procedure for the determination of the Hydricity of Ir-H

In a N_2 filled glovebox, to a vial containing a solution of Ir-Cl (1.67 mg, 3.23 μmol, 1 eq) in 1 mL dry MeCN-d_3, $NaPF_6$ (1.08 mg, 6.46 μmol, 2 eq) was added and left to stir for 24 h. The

resulting precipitate, NaCl, was filter off via a celite plug and the solution was moved to an NMR tube containing Et_3N (3.51 mg, 34.69 μmol, 10.7 eq) and $[Et_3NH][PF_6]$ (1.60 mg, 6.47 μmol, 2 eq). The NMR tube was then degassed and 1 atm of H_2 was added. NMR tracked the reaction, with the solution reaching equilibrium after 48 h, and the equilibrium constant of the reaction was determined. This was then repeated 3 times, varying the amount of added Et_3N and $[Et_3NH][PF_6]$ (see Appendix).

3.4.4 General Procedure of Formic Acid Decomposition

To 250 mL 2-neck round bottom flask with a magnetic stir bar, $[Bu_4N][HCO_2]_2H$ (100 mg, 0.3 mmol, 100 eq) and MeCN (99 mL) were added. The flask was then attached to a reflux condenser. Via tygon tubing, the condenser was then attached to a 3-way valve to the Schlenk line. The solution was then sparged with N_2 for 30 minutes. To the 3-way valve, a silicone oil bubbler was attached via tygon tubing and sparged with N_2 for 5 minutes. The bubbler was then attached to a graduated burette filled with silicone oil to prevent gas dissolution (*see Appendix Section 3.7.5*). The flask was then lowered into an oil bath that was preheated to 80°C and allowed to equilibrate (1 h). Then either **Ir-Cl** or **Ir-H** (3 μmol, 1 eq) in 1 mL of degassed, dry MeCN was added to the solution through a rubber septum and the system was cut off from active N_2 flow. The reaction was then opened to the burette via the 3-way valve. The initial volume of the oil in the burette was recorded. As gas evolution lowered the level of the silicone oil in the burette, the separatory funnel was lowered to keep the oil levels approximately the same to maintain atmospheric pressure in the reaction. The level of the oil was recorded every 10 minutes over the 2-hour experiment. This procedure was repeated 3 times. Gas evolution is reported as the measured gas in the catalytic reaction minus the average gas measurement at the same time for 3 control

(without catalyst) trials. Turnover numbers are reported as the number of moles of both CO_2 and H_2 utilizing the ideal gas law and equation 3.7.

The turnover number is then determined using the following equation (3.8)

$$n_{prod}\ TON = \frac{n_{prod}}{n_{cat}} \qquad \text{(Equation 3.8)}$$

$$2(22.4\frac{L}{mol})$$

3.4.5 Determination of gaseous species

To confirm the formation of CO_2 during the reaction, 1 mL of the head space was sampled prior to the addition of catalyst and added to an evacuated IR gas cell and the spectra was then obtained. The catalyst was then added to the solution and the formic acid decomposition was allowed to run for 2 h. Then, 1 mL of the headspace of the reaction was then sample and added to the evacuated IR gas cell and the spectra was recorded. CO_2 was confirmed via the appearance of the rovibrational transitions between 2380 cm^{-1} and 2280 cm^{-1}. Additionally, there were no CO rovibrational transitions detected between 2200 cm^{-1} and 2100 cm^{-1}.

To confirm the formation of H_2 during the reaction, GC was performed on 2 mL of headspace prior to the start of the reaction. Then the catalyst was added to the reaction and allowed to run for 30 minutes. Then another 2 mL of the headspace were sampled via GC showing the formation of H_2, with no formation of CO observed.

3.4.6 General Procedure for the determination of the rate of Hydrogen Evolution

In a N_2 filled glovebox, to an NMR tube containing 1 equivalent of **Ir-H** (~1.5 mg) and a known amount of 1,2,4,5-tetramethylbenzene (internal standard) in 0.7 mL of dry MeCN-d_3, 1.1 equivalents of acid were added. The solution was then monitored by ^{1}H NMR over the next 3 h.

The rate of reaction was measured by the ratio of non-overlapping phenylpyridine proton signals of **Ir-H** and **Ir-MeCN** in the NMR.

3.4.7 NMR study of the Transfer Hydrogenation of 2-Cyclohexen-1-one

In a N_2 filled glovebox, to a J. Young NMR tube containing $[Bu_4N][HCO_2]_2H$ (20 mg, 59.97 μmol, 1 eq.) and 2-cyclohexen-1-one (2.88 mg, 29.98 μmol, 0.5 eq) in 1 mL of dry MeCN-d_3, 20 μL of a 30 mM solution of Ir-H in MeCN-d_3 was added. The NMR tube was then taken out of the glove box and placed into an oil bath preheated to 45°C. The reaction was monitored by NMR over the course of 4 days. The NMR was compared to the NMR of the starting material and possible products to determine selectivity.

3.4.8 Measurement of Gas Production during Transfer Hydrogenation

The experimental setup for the measurement of gas from TH was identical to the formic acid decomposition experiment, except for the addition of 2-cyclohexen-1-one (14.41 mg, 0.150 μmol, 50 eq) to the round bottom flask prior to the connection of the reflux condenser. After 2 h, the reaction was removed from the oil bath and allowed to cool to room temperature. After cooling, the solvent was removed. 2 mL of MeCN-d_3 was added to flask for NMR analysis. The selectivity of the molecule was determined by comparing the crude mixture with the possible products. The yield was determined via the ratio for the integration of the starting material versus the product.

3.5 Acknowledgements

Chapter 3, in full, is being prepared for submission for publication of the material entitled Miller, C.J.; Okuno, S.; Brunner, F.M.; Waldie, K.M.; Weddle, L.R.; Lee, B.; Kubiak, C.P. Hydricity as a Guide in H_2 Evolution, Formic Acid Decomposition, and Transfer Hydrogenation: A Case Study with Ir(Cp*)(2-phenylpyridine)H. The dissertation author was the primary researcher and author of this paper. We also acknowledge Dr. Michael L. Neville and Joseph

Palasz for invaluable discussion and the Kubiak group members for their feedback. This work is supported by the Air Force Office of Scientific Research under Award No. FA9550-17-0198.

3.6 References

1. Wang, D.; Astruc, D., The Golden Age of Transfer Hydrogenation. *Chem. Rev.* **2015,** *115* (13), 6621-6686.

2. Samec, J. S. M.; Bäckvall, J.-E.; Andersson, P. G.; Brandt, P., Mechanistic aspects of transition metal-catalyzed hydrogen transfer reactions. *Chem. Soc. Rev.* **2006,** *35* (3), 237-248.

3. Brieger, G.; Nestrick, T. J., Catalytic Transfer Hydrogenation. *Chem. Rev.* **1974,** *74*, 567.

4. Himeda, Y.; Onozawa-Komatsuzaki, N.; Miyazawa, S.; Sugihara, H.; Hirose, T.; Kasuga, K., pH-Dependent Catalytic Activity and Chemoselectivity in Transfer Hydrogenation Catalyzed by Iridium Complex with 4,4′-Dihydroxy-2,2′-bipyridine. *Chem. Eur. J.* **2008,** *14*, 11076.

5. Ogo, S.; Makihara, N.; Kaneko, Y.; Watanabe, Y., pH-Dependent Transfer Hydrogenation, Reductive Amination, and Dehalogenation of Water-Soluble Carbonyl Compounds and Alkyl Halides Promoted by Cp*Ir Complexes. *Organometallics* **2001,** *20*, 4903.

6. Trochagr, J.; Henbest, H. B., Catalysis of the Transfer of Hydrogen from Propan-2-ol to α,β-Unsaturated Ketones by Organoiridium Compounds. A Carbon-Iridium Compound Containing a Chelate Keto-group. *Chem. Commun.* **1967**, 544.

7. Blum, J.; Sasson, Y.; Iflah, S., Hydrogen Transfer from Formyl Compounds to α,β-Unsaturated Ketones Catalyzed by Ru, Rh and Ir Complexes. *Tetrahedron Lett.* **1972,** *13*, 1015.

8. Chowdhury, R. L.; Bäckvall, J. E., Efficient Ruthenium-catalysed Transfer Hydrogenation of Ketones by Propan-2-ol. *J. Chem. Soc., Chem. Commun.* **1991**, 1063.

9. Aliende, C.; Pérez-Manrique, M.; Jaloń, F. A.; Manzano, B. R.; Rodrıǵuez, A. M.; Espino, G., Arene Ruthenium Complexes as Versatile Catalysts in Water in both Transfer Hydrogenation of Ketones and Oxidation of Alcohols. Selective Deuterium Labeling of rac-1-Phenylethanol. *Organometallics* **2012,** *31*, 6106.

10. Uematsu, N.; Fujii, A.; Hashiguchi, S.; Ikariya, T.; Noyori, R., Asymmetric Transfer Hydrogenation of Imines. *J. Am. Chem. Soc.* **1996,** *118*, 4916.

11. Albrecht, M.; Crabtree, R. H.; Mata, J.; Peris, E., Chelating Bis-Carbene Rhodium(III) Complexes in Transfer Hydrogenationof Ketones and Imines. *Chem. Commun.* **2002**, 32.

12. Kuhl, S.; Schneider, R.; Fort, Y., Transfer Hydrogenation of Imines Catalyzed by a Nickel(0)/NHC Complex. *Organometallics* **2003,** *22*, 4184.

13. Canivet, J.; Süss-Fink, G., Water-Soluble Arene Ruthenium Catalysts Containing Sulfonated Diamine Ligands for Asymmetric Transfer Hydrogenation of α-Aryl Ketones and Imines in Aqueous Solution. *Green Chem.* **2007,** *9*, 391.

14. Braunstein, P.; Naud, F.; Pfaltz, A.; Rettig, S. J., Ruthenium Complexes with Novel Tridentate N,P,N Ligands Containing a Phosphonite Bridge between Two Chiral Oxazolines. Catalytic Activity in Cyclopropanation of Olefins and Transfer Hydrogenation of Acetophenone. *Organometallics* **2000,** *19*, 2676.

15. Horn, S.; Gandolfi, C.; Albrecht, M., Transfer Hydrogenation of Ketones and Activated Olefins Using Chelating NHC Ruthenium Complexes. *Eur. J. Inorg. Chem.* **2011**, 2863.

16. Yang, P.; Xu, H.; Zhou, J., Nickel-Catalyzed Asymmetric Transfer Hydrogenation of Olefins for the Synthesis of α- and β-Amino Acids. *Angew. Chem., Int. Ed.* **2014,** *53*, 12210.

17. Sanz, S.; Benítez, M.; Peris, E., A New Approach to the Reduction of Carbon Dioxide: CO2 Reduction to Formate by Transfer Hydrogenation in iPrOH. *Organometallics* **2010,** *29*, 275.

18. Samec, J. S. M.; Backvall, J. E.; Andersson, P. G.; Brandt, P., Mechanistic Aspects of Transition Metal-Catalyzed Hydrogen Transfer Reactions. *Chem. Soc. Rev.* **2006,** *35*, 237.

19. Fellay, C.; Yan, N.; Dyson, P. J.; Laurenczy, G., Selective Formic Acid Decomposition for High-Pressure Hydrogen Generation: A Mechanistic Study. *Chem. Eur. J.* **2009,** *15* (15), 3752-3760.

20. Johnson, T. C.; Morris, D. J.; Wills, M., Hydrogen generation from formic acid and alcohols using homogeneous catalysts. *Chem. Soc. Rev.* **2010,** *39* (1), 81-88.

21. Sordakis, K.; Tang, C.; Vogt, L. K.; Junge, H.; Dyson, P. J.; Beller, M.; Laurenczy, G., Homogeneous Catalysis for Sustainable Hydrogen Storage in Formic Acid and Alcohols. *Chem. Rev.* **2018,** *118* (2), 372-433.

22. Wiedner, E. S.; Chambers, M. B.; Pitman, C. L.; Bullock, R. M.; Miller, A. J. M.; Appel, A. M., Thermodynamic Hydricity of Transition Metal Hydrides. *Chem. Rev. (Washington, DC, U. S.)* **2016,** *116* (15), 8655-8692.

23. Waldie, K. M.; Ostericher, A. L.; Reineke, M. H.; Sasayama, A. F.; Kubiak, C. P., Hydricity of Transition-Metal Hydrides: Thermodynamic Considerations for CO2 Reduction. *ACS Catal.* **2018,** *8* (2), 1313-1324.

24. Turlington, C. R.; Harrison, D. P.; White, P. S.; Brookhart, M.; Templeton, J. L., Probing the Oxidation Chemistry of Half-Sandwich Iridium Complexes with Oxygen Atom Transfer Reagents. *Inorg. Chem.* **2013,** *52* (19), 11351-11360.

25. Tshepelevitsh, S.; Kütt, A.; Lõkov, M.; Kaljurand, I.; Saame, J.; Heering, A.; Plieger, P. G.; Vianello, R.; Leito, I., On the Basicity of Organic Bases in Different Media. *Eur. J. Org. Chem.* **2019,** *2019* (40), 6735-6748.

26. DuBois, D. L.; Berning, D. E., Hydricity of transition-metal hydrides and its role in CO2 reduction. *Appl. Organomet. Chem.* **2000,** *14* (12), 860-862.

27. Stirling, M. J.; Sweeney, G.; MacRory, K.; Blacker, A. J.; Page, M. I., The kinetics and mechanism of the organo-iridium-catalysed enantioselective reduction of imines. *Organic & Biomolecular Chemistry* **2016,** *14* (14), 3614-3622.

28. Ilic, S.; Alherz, A.; Musgrave, C. B.; Glusac, K. D., Thermodynamic and kinetic hydricities of metal-free hydrides. *Chem. Soc. Rev.* **2018,** *47* (8), 2809-2836.

29. Zhu, X.-Q.; Chen, X.; Mei, L.-R., Determination of Hydride Affinities of Various Aldehydes and Ketones in Acetonitrile. *Org. Lett.* **2011,** *13* (9), 2456-2459.

30. Zhu, X.-Q.; Zhang, M.; Liu, Q.-Y.; Wang, X.-X.; Zhang, J.-Y.; Cheng, J.-P., A Facile Experimental Method To Determine the Hydride Affinity of Polarized Olefins in Acetonitrile. *Angew. Chem. Int. Ed.* **2006,** *45* (24), 3954-3957.

31. Scheeren, C.; Maasarani, F.; Hijazi, A.; Djukic, J.-P.; Pfeffer, M.; Zaric, S. D.; Le Goff, X.-F.; Ricard, L., Stereoselective "Electrophilic" Cyclometalation of Planar-Prochiral (η6-Arene)tricarbonylchromium Complexes with Asymmetric Metal Centers: pseudo-T-4 [CpRhCl2]2 and [CpIrCl2]2. *Organometallics* **2007,** *26* (14), 3336-3345.

32. Park-Gehrke, L. S.; Freudenthal, J.; Kaminsky, W.; DiPasquale, A. G.; Mayer, J. M., Synthesis and oxidation of Cp*IrIII compounds: functionalization of a Cp* methyl group. *Dalton Trans.* **2009,** (11), 1972-1983.

33. Seu, C. S.; Appel, A. M.; Doud, M. D.; DuBois, D. L.; Kubiak, C. P., Formate oxidation via beta-deprotonation in [Ni((P2N2R ')-N-R)(2)(CH3CN)](2+) complexes. *Energy Environ. Sci.* **2012,** *5* (4), 6480-6490.

34. Saba, S.; Hernandez, R.; Choy, C. C.; Carta, K.; Bennett, Y.; Bondi, S.; Kolaj, S.; Bennett, C., A simple and efficient one-step protocol for the preparation of alkyl-substituted ammonium tetrafluoroborate and hexafluorophosphate salts. *J. Fluorine Chem.* **2013,** *153*, 168-171.

3.7 Appendix

3.7.1 NMR determination of Cl dissociation

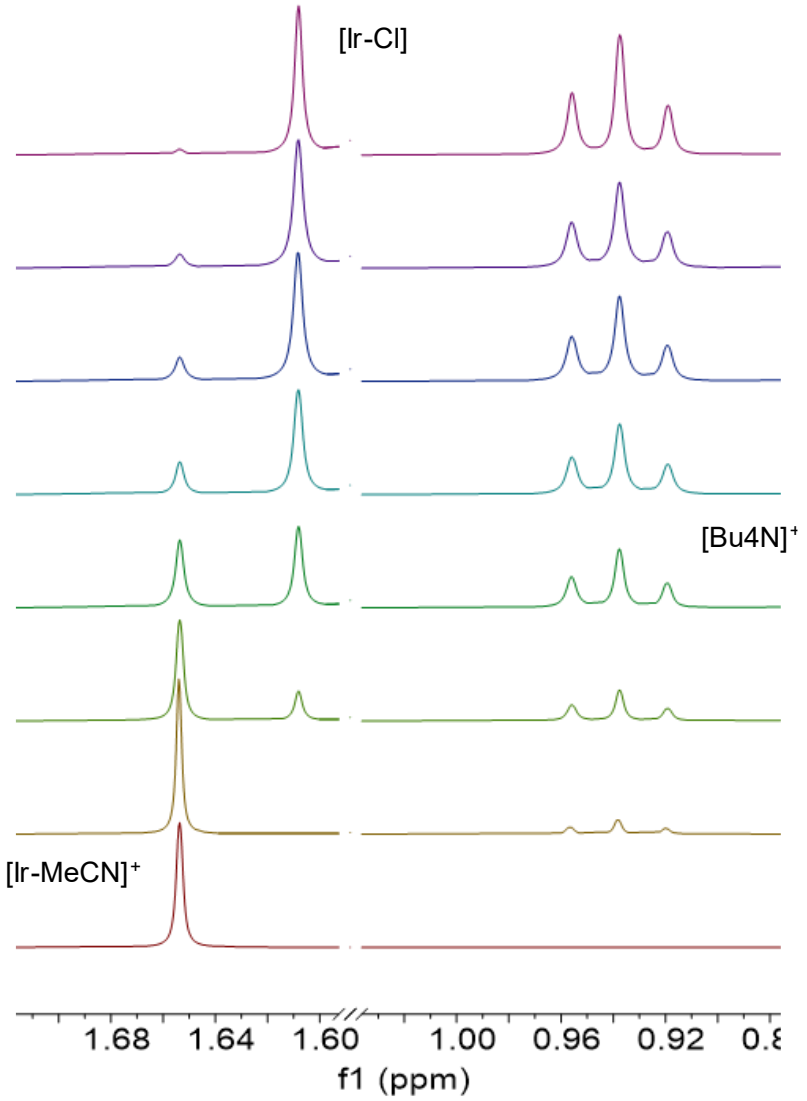

Figure 3.7. ^{1}H NMR spectra showing the relative concentrations of **Ir-MeCN** and **Ir-Cl** (Cp* region) when [Bu_4N][Cl] is added.

3.7.2 NMR of Formic Acid Decomposition with Ir-C

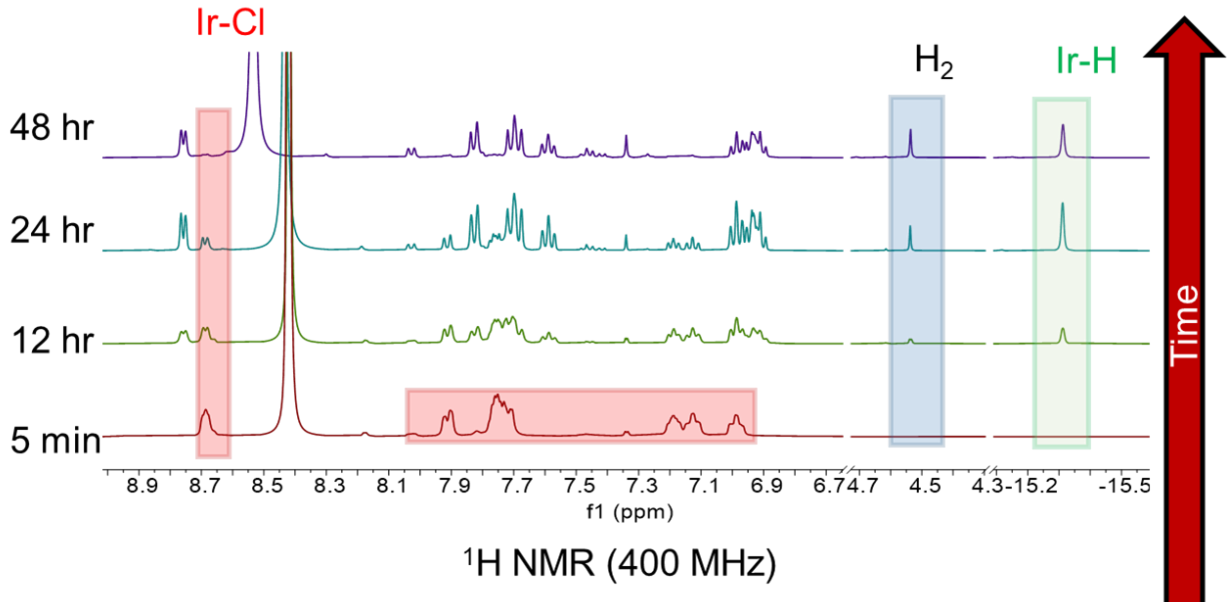

Figure 3.8. ^{1}H NMR spectra of the formic acid decomposition starting with **Ir-Cl**, showing that the only two species of Ir detected on an NMR time scale are **Ir-Cl** and **Ir-H.**

3.7.3 FTIR Spectra of Formic Acid Reaction Headspace

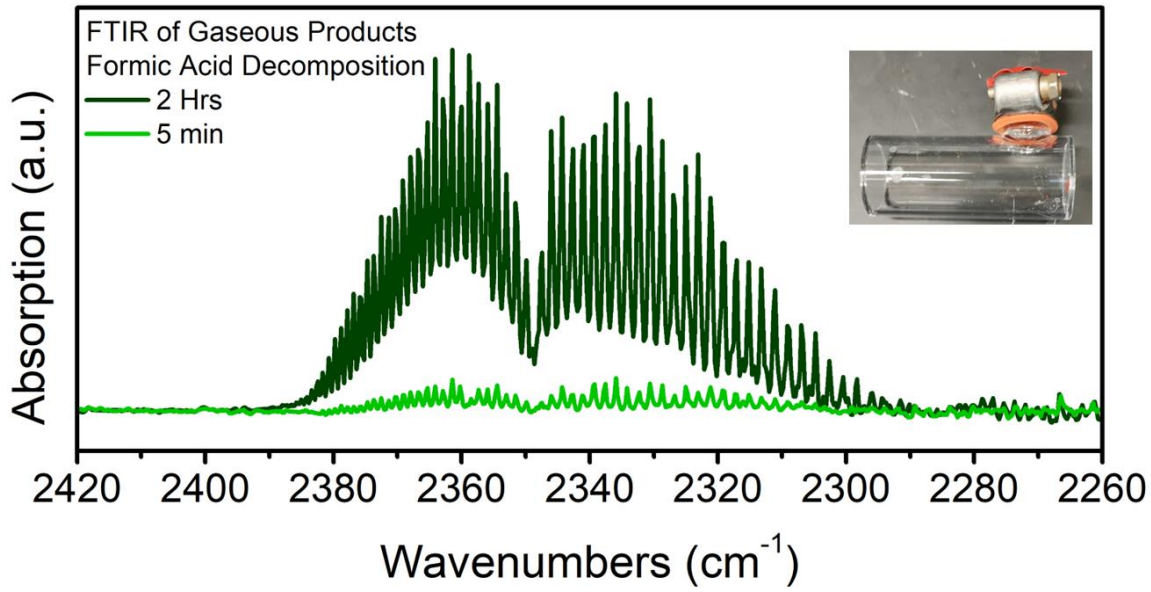

Figure 3.9. FTIR spectra of the headspace of the formic acid decomposition reaction run at 80°C showing significant formation of CO_2 gas. (Inset) The IR gas cell used for detection of CO_2

3.7.4 GC of Formic Acid Reaction Headspace

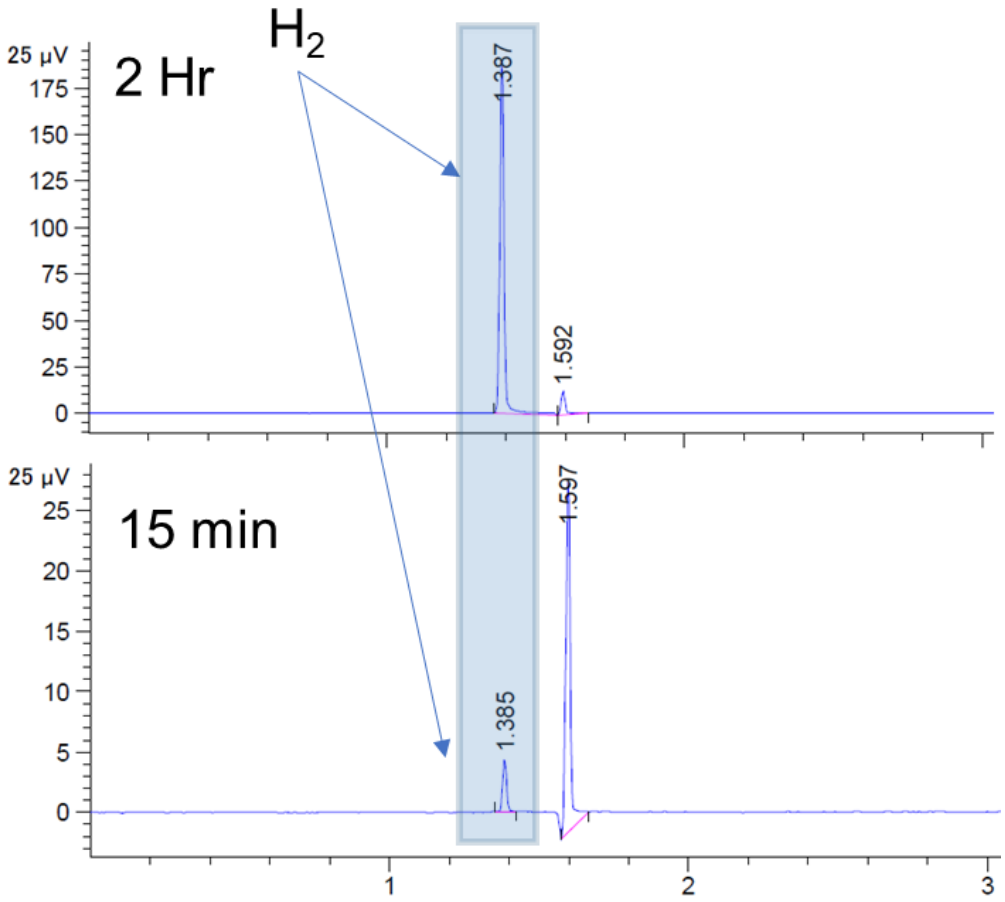

Figure 3.10. GC trace of the H_2 detection using N_2 as the carrier gas. The other peak is from air.

3.7.5 Diagram of Experimental Set Up for Gas Volume Measurement

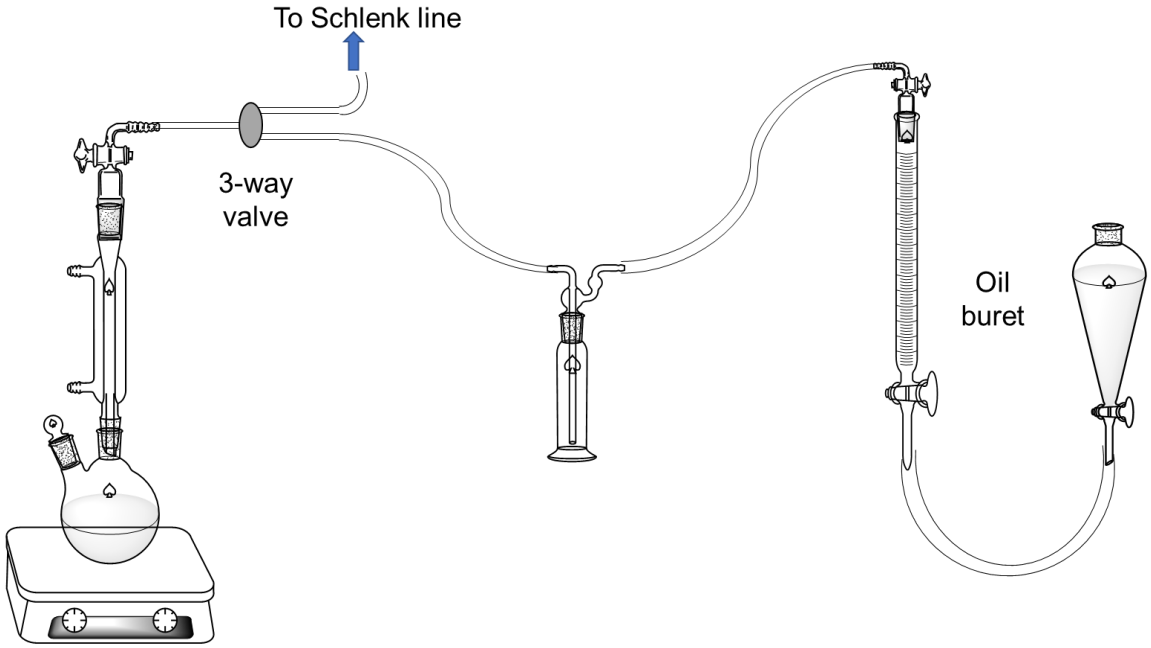

Figure 3.11. Diagram showing the experimental set up for the measurement of the volume of gas produced during formic acid decomposition and transfer hydrogenation.

3.7.6 NMR of Transfer Hydrogenation Reaction at 45°C

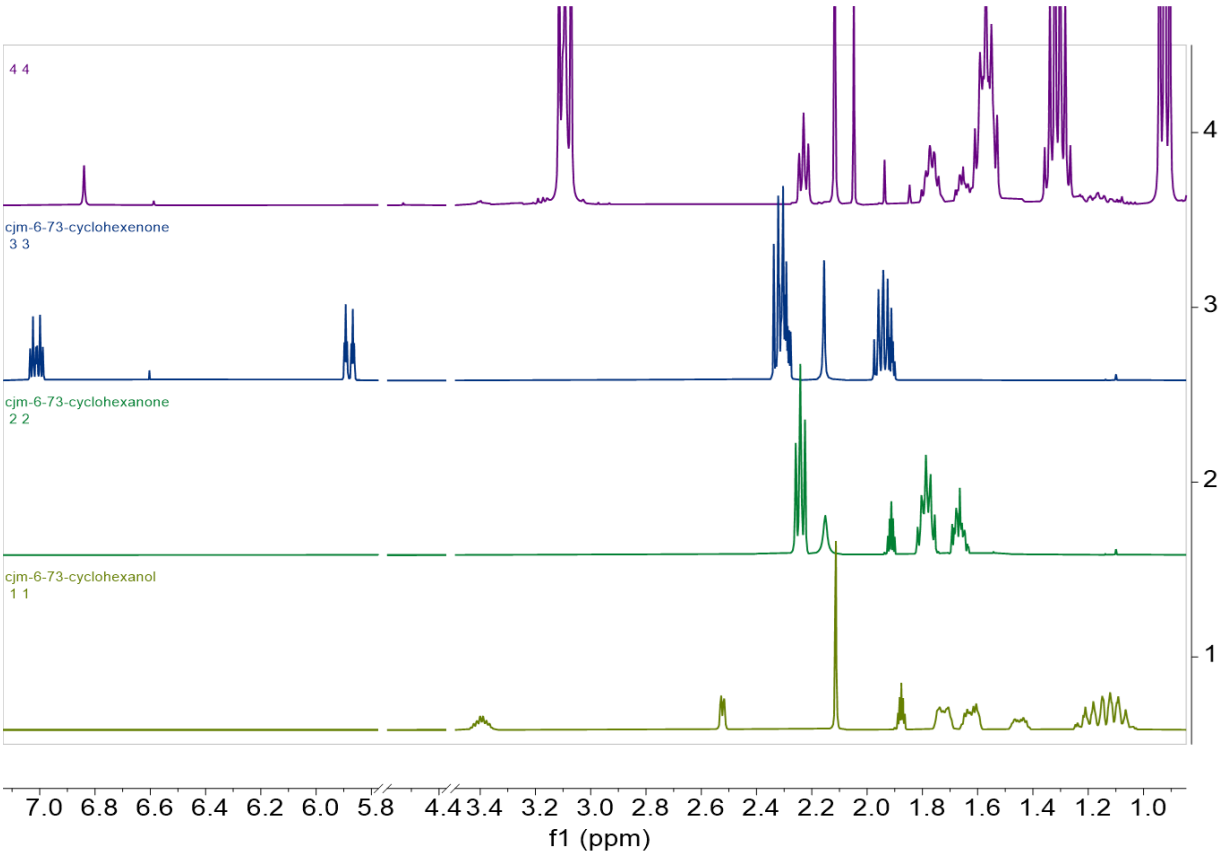

Figure 3.12. ^{1}H NMR spectrum of the TH at 45°C after 4 days (top, purple). Additionally, the 1H NMR of purchased 2-cyclohexen-1-one (blue), cyclohexanone (green), and cyclohexanol (yellow-green).

3.7.7 NMR of the crude reaction mixture following TH at 80°C

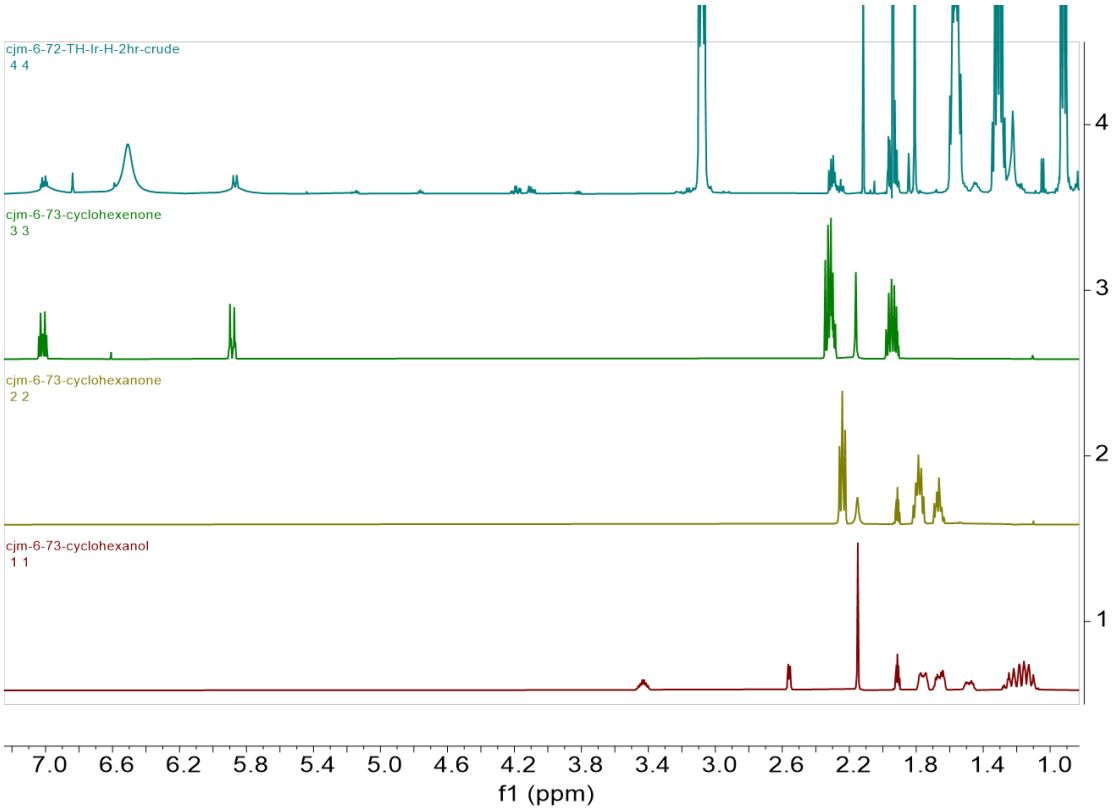

Figure 3.13. ^{1}H NMR spectrum of the crude reaction mixture obtained after TH at 80 °C for 2 h (top, blue). Additionally, the ^{1}H NMR of purchased 2-cyclohexen-1-one (green), cyclohexanone (yellow-green), and cyclohexanol (red).

CHAPTER 4. PM-IRRAS and DFT Investigation of the Surface Orientation and Reactivity of New Ir Piano-stool Complexes Attached to Au (111)

4.1 Introduction

Iridium piano-stool complexes, such as [Ir(Cp*)(bpy)(Cl)]Cl and Ir(Cp*)(ppy)(Cl) (where Cp*=pentamethylcyclopentadienyl, bpy = 2,2'-bipyridine and ppy = 2-phenylpyridine) are highly active catalysts for a wide range of fundamental transformations, including electrochemical and photochemical hydrogen evolution[1-5] and transfer hydrogenation/dehydrogenation of ketones[6-10], olefins[11-12], formic acid[13-14], and CO_2.[15-17] These types of catalysts are generally selective, tunable, easy to characterize, and their mechanisms can be well understood via conventional spectroscopies. Heterogeneous catalysts, on the other hand, are often touted for their stability, activity, scalability, low catalyst loadings required on supports, and ease of separation of products. In contrast to homogeneous catalysts, their mechanisms are often more difficult to interpret due to the intrinsic difficulty in analyzing surfaces. This lack of mechanistically informed synthesis often hinders catalyst design, so catalyst discovery often relies on high-throughput screening and predictive modeling as opposed to rational design.[18] Thus, surface immobilization of molecular catalysts aims to provide the benefits of both homogeneous molecular and heterogeneous catalysts.[19]

Previously, iridium piano-stool complexes have been attached to semiconductor surfaces[20-25]; however, their orientation on the surface was not described. The orientation of these catalysts could have significant effects on activity, as the bulky cyclopentadienyl or surface may block substrates from reacting with the Ir center.[24, 26] Au surfaces are ideal for this type of study as surface attachment via self-assembled monolayers of thiols and disulfides is a well-established, covalent attachment strategy.[27-29] In addition, the properties of Au allow for surface-sensitive IR characterization using polarization modulation infrared reflection absorption spectroscopy (PM-IRRAS).[30-32] PM-IRRAS has already been shown to be a useful tool for determining average binding orientation for organic thiols[33-35], electrochemical absorbates[36-38], and molecular catalysts[27, 39-43] on conducting surfaces. Due to the selection rules of PM-IRRAS on metal surfaces, p-polarized light will interact with the absorbed molecules and only transition dipole moments (TDM) with a component normal to the surface will absorb the light, reinforced by the image dipole.[31, 44-46] The relative absorption of these transition dipole moments, coupled with density functional theory (DFT) calculations are useful in determining the average molecular orientation of SAMs on Au.

Herein, we describe the synthesis and characterization of three new Ir piano-stool complexes with sulfur modified bipyridine and phenylpyridine ligands (**C1**, **C2**, and **C3**). The differences in the reactivities of these ligands and the synthesis of the complexes are described. Self-assembled monolayers of **C1** and **C2** were made and characterized, giving two new surface-immobilized Ir complexes on Au surfaces. Using PM-IRRAS and DFT, the average molecular orientations on the surface were determined.

4.2 Results and Discussion

4.2.1 Synthesis and Characterization of Ligands

To prevent direct reactivity of a free thiol with the iridium center, which is known to readily react with thiolate ligands[47], disulfides were chosen over free thiols as the attachment strategy (Figure 4.1). Disulfides are also known to cleave upon self-assembly onto Au surfaces without

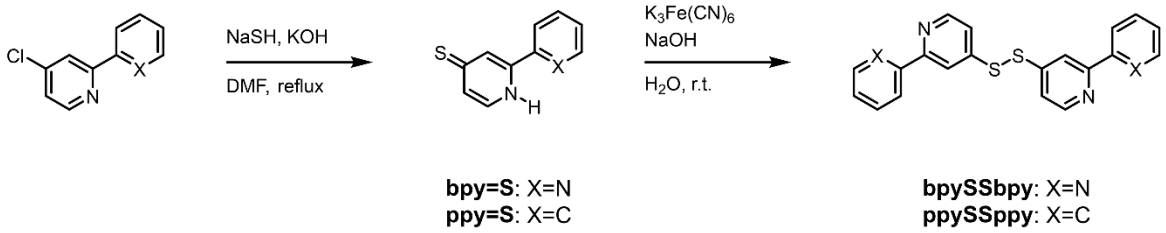

Figure 4.1. Synthesis of disulfide ligands bpySSbpy and ppySSppy.

generating byproducts.[29] Both ligands di(2,2'-bipyridine)-4-disulfide (**bpySSbpy**) di(2-phenylpyridine)-4-disulfide (**ppySSppy**) were synthesized from their corresponding 4-chloro-pyridine derivatives. 4-chloro-2,2'-bipyridine was synthesized using a literature procedure or was obtained from commercial sources.[48]

4-chloro-2-phenylpyridine was obtained by cross-coupling of phenylboronic acid with 2-bromo-4-chloropyridine following a literature procedure.[49] The pyridine-chlorides were converted into thiones through nucleophilic aromatic substitution of the chloride with sodium hydrogen sulfide in basic DMF following modified literature procedures.[27, 50] The dry NaSH was replaced with technical grade NaSH · xH_2O with no adverse effects on the reaction. The same procedure was used to synthesize 4-thione-2-phenylpyridine. Both thiones are insoluble in neutral water but readily dissolve under basic conditions. Oxidation of the thiones yields the more stable disulfide. The previously reported procedure used catalytic NaI and hydrogen peroxide as the oxidant which resulted in low yields of under 40%.[27] Since the reaction proceeds through a simple outer sphere

electron transfer, any oxidant with a sufficient oxidation potential can be used. The oxidation of the thione to disulfide is best carried out in aqueous conditions. Potassium ferricyanide is a readily available water-soluble oxidant with a sufficient oxidation potential. Furthermore, it is otherwise inert under the reaction conditions, preventing side reactions and the only byproduct is water-soluble ferrocyanide. Upon addition of the oxidant, the disulfide is formed immediately and precipitates out under the reaction conditions, while all other species are highly water-soluble. The disulfides were isolated in almost quantitative yield by filtration. If pure thione is used in the reaction no further purification steps are necessary. However, we found that purification of **ppySSppy** by flash column chromatography efficiently removes possible impurities from previous steps.

4.2.2 Synthesis and Characterization of Molecular Complexes

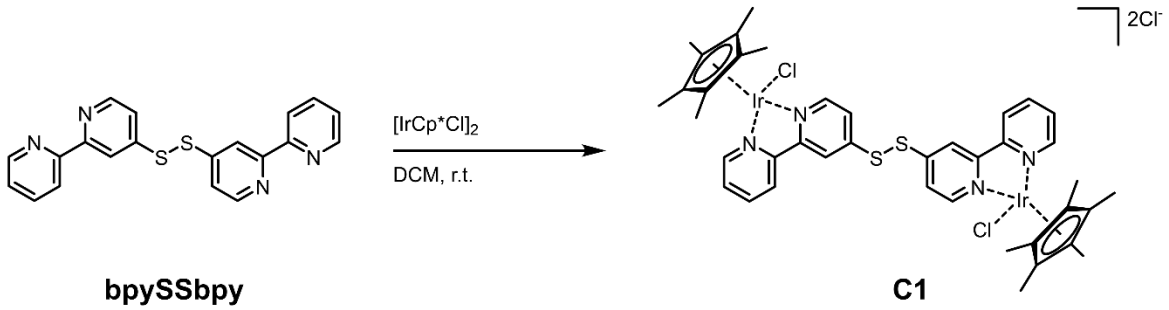

Figure 4.2. Synthesis of **C1** from the corresponding ligand and [Ir(Cp*)Cl2]2 dimer.

[Cp*Ir((2,2'-bipyridine-4-sulfide)Cl]2[Cl]2 (C1). Metalation of the bpySSbpy ligand with $[Ir(Cp^*)Cl2]_2$ led to the formation of $[Cp^*Ir((2,2'\text{-bipyridine-4-sulfide})Cl]_2[Cl]_2$ (C1). The metalation can be carried out in MeOH or DCM under an inert atmosphere. Using MeOH as the solvent had several drawbacks. First, the low solubility of the iridium precursor in MeOH requires the reaction to be carried out at 40 °C. Under these conditions, to avoid the formation of partially metalated ligand, a slight excess of metal was used in this procedure. The reaction mainly yielded

the title compound with slight impurities of excess starting material and side products. Purification by flash column chromatography over neutral alumina improved the purity of the product. Carrying out the reaction in DCM (Fig. 2) has several advantages. The higher solubility of the starting material permitted running the reaction at room temperature which led to a cleaner reaction. Furthermore, the elimination of MeOH as a solvent allowed us to carry out the reaction and purification in a glove box, providing rigorous exclusion of oxygen and water and simplifying handling. This also allowed us to utilize stoichiometric amounts of ligand and metal and resulted in improved purity. In addition, the product is highly hygroscopic, quickly picking up water in air, leading to difficulty in purification. This can be seen in the FTIR spectra of the KBr pellet made from the compound made in air, leading to a broad peak between 3100-3600 cm^{-1} (Fig. S22B). However, this peak did not appear in the ATR-IR of the product when the reaction and ATR-IR measurement was done in the glovebox (Fig. S22A). Precipitation from DCM through the addition of THF resulted in pure product.

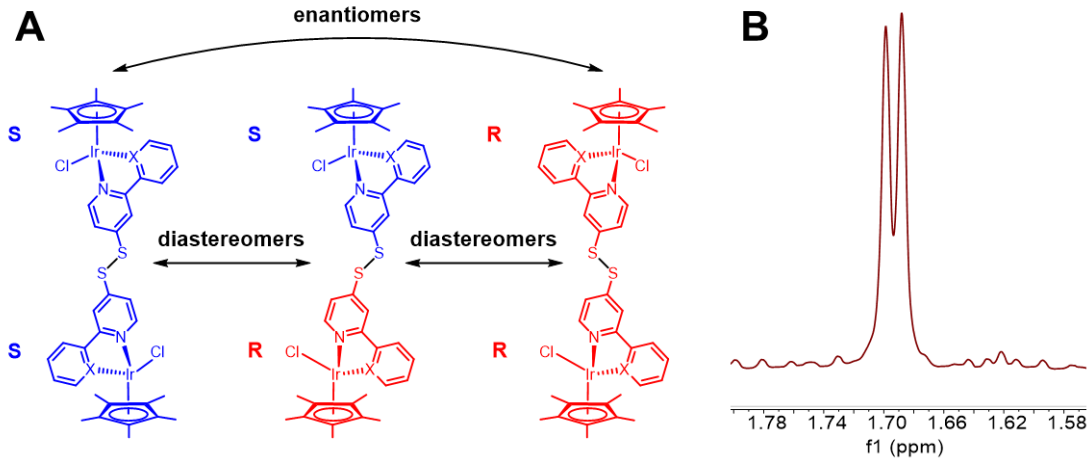

Figure 4.3. A) Representation of the enantiomers (S,S and R,R) and diastereomers (S,S and R,R are diastereomer of S,R) of C1: X=N or C2: X=C that are formed as a statistical mixture. B) the ^{1}H NMR of the methyl protons on the Cp* ring showing the splitting due the chirality at the metal of C1 in $CDCl_3$.

The iridium center in **C1** is an enantiomeric center, making molecules of this type chiral. Only a few reports mention the chiral nature of the molecules, often when it represents the key

component of the work.[51-52] Utilizing the disulfide dimer **bpySSbpy** as a ligand, we connect the two chiral metal centers from each complex, leading to the formation of diastereomers. While the difference between the diastereomers is not large, the two diastereomers can be distinct in proton NMR (Fig. S10 and S11). The Cp* experiences a different environment in both diastereomers, leading to two distinct peaks in the ^{1}H NMR centered at δ=1.71 ppm. The splitting is influenced by the solvent. While in chloroform, there is a measurable separation of 0.02 ppm (Fig. 3) between the two Cp* peaks, in acetonitrile the two peaks almost coalesce with a separation of only 0.0015 ppm (Fig. S10). For the bipyridine there are also distinguished peaks observed for several protons. This further illustrates the similarity of the two isomers, and the influence the solvent has on the dynamics of the molecule. Attempts to separate the two diastereomers by fractional crystallization were not successful but were also unnecessary for further use in surface modification. During the formation of the SAM, the disulfide bond is homolytically cleaved by the Au surface.[27, 29] This cleavage of the disulfide yields monomers that are chiral enantiomers, not diastereomers.

Cp*Ir(2-phenylpyridine-4-sulfide)Cl]$_2$ (C2) and [Cp*Ir(2-phenylpyridine-4-thiol)]$_3$ (C3). Initial attempts to cyclometalate [Ir(Cp*)Cl$_2$]$_2$ with **ppySSppy** resulted in the formation of a mixture of eight different compounds that could be separated by flash column chromatography. Only the first fraction was identified. An X-ray crystal structure (Fig.

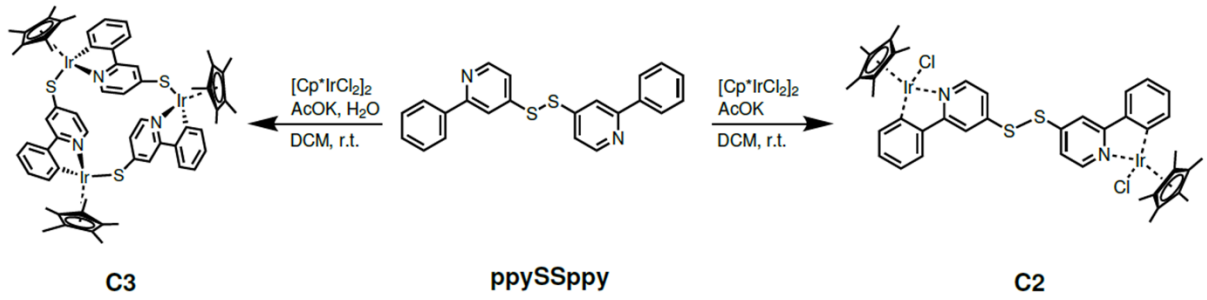

Figure 4.4. Synthesis of **C2** from the corresponding ligand and [Ir(Cp*)Cl$_2$]$_2$ dimer (right). The same reaction conditions in the presence of trace water lead to the formation of **C3** (left).

S43) was obtained that corresponds to the trimer [Cp*Ir(2-phenylpyridine-4- thiol)]$_3$ (**C3**). The iridium is bonded to one unit of the phenylpyridine and the next unit of thiol. If the reaction is carried out under rigorous exclusion of water and oxygen in a nitrogen-filled glove box, C2 is formed as the predominant product (Fig. 4). We speculate that the formed [Cp*IrppyCl] complex can lose the chloride ligand in the presence of water and cleave the disulfide.[53] We believe that evidence of this is seen in the ATR-IR of a **C2** done in air. A weak, broad peak ranging from 3200-3600 cm^{-1} corresponding to $\nu_{stretch}$(O-H) of water forms once the compound is brought into air (Fig. S23B). We believe this leads to the formation of different oligomers with the **C3** trimer being a particularly stable species that is formed in significant quantities. Similar to **C1**, the $\nu_{stretch}$(O-H) does not appear in the ATR-IR of the purified compound taken in a N_2-filled glovebox. As with the bipyridine counterpart, **C2** is also chiral and isolated as a statistical mixture of enantiomers.

4.2.3 Complex Orientation on Au Surface by DFT Calculations

Disulfide bonds are known to cleave in the presence of a gold surface to form self-assembled monolayers. In the case of the **C1** and **C2** dimers, the disulfide bond breaks to form a monolayer of the monomer, herein referred to as **C1m** and **C2m,** respectively. Following our previous studies,[26-27, 54-56] the lowest energy binding modes for **C1m** and **C2m** were determined using DFT. In accordance with experimental measurements discussed later, **C3** was found to have very weak interactions with the Au surface precluding the characterization of a well-defined binding geometry. All calculations were performed in Gaussian 16, Revision C.01[57] using the ωB97X-D functional;[58] nonmetal atoms were treated with a 6-31G(d,p) basis set[59-61] and the DEF2SVP basis set and pseudopotential[62] were used on Ir and Au (see SI for further discussions

about the computational method). Frequency calculations were used to confirm stationary points and perform spectroscopic analysis of **C1m** and **C2m**.

Table 4.1. Orientational and energetic parameters of the DFT optimized (wB97XD functional and the DEF2SVP basis set) structures of **C1m** and **C2m** shown in Fig. 5.

Structure	Cl orientation	Tilt angle (°)		Twist Angle (°)	Relative Energy (kcal/mol)	S-Au (Å)
		θ_1	θ_2	ψ_1		
C1m	Up	75	23	91	0	2.39
	Down	77	76	268	-2.8	2.47
C2m	Up	73	23	93	-1.8	2.26
	Down	76	74	269	0	2.32

To characterize the binding modes of **C1m** and **C2m** on the surface, we utilize the Euler angles relating to the molecular frame to the laboratory frame fixed on the gold surface according to tilt (θ), twist (ψ), and rotation (phi) (Fig. 5A and B). Here, θ_1 refers to the tilt angle of the bipyridine for **C1** and phenylpyridine for **C2** and θ_2 refers to the tilt of the Cp* angle relative to the surface normal. The geometry could not be assumed for monolayers formed for **C1m** and **C2m.** Therefore, two possible DFT-optimized geometries were determined for each complex, one with the chloride atom pointing towards the surface (Cl down) and the other pointing away (Cl up). Other considered starting orientations optimized to either the Cl down or Cl up geometry.

The four DFT optimized orientations of **C1m** and **C2m** are depicted in **Fig. 5** and their relevant geometrical parameters and energetics are described in **Table 4.1**. Interestingly, DFT indicates that the **C1m** and **C2m** have different preferred orientations. For **C1m**, the Cl up orientation is 2.8 kcal/mol higher in energy compared to the Cl down orientation. For **C2m**, the relative energy for the Cl down orientation is 1.8 kcal/mol higher than that of the Cl up orientation. However, in both cases, the small energy differences indicate that there is unlikely to be a

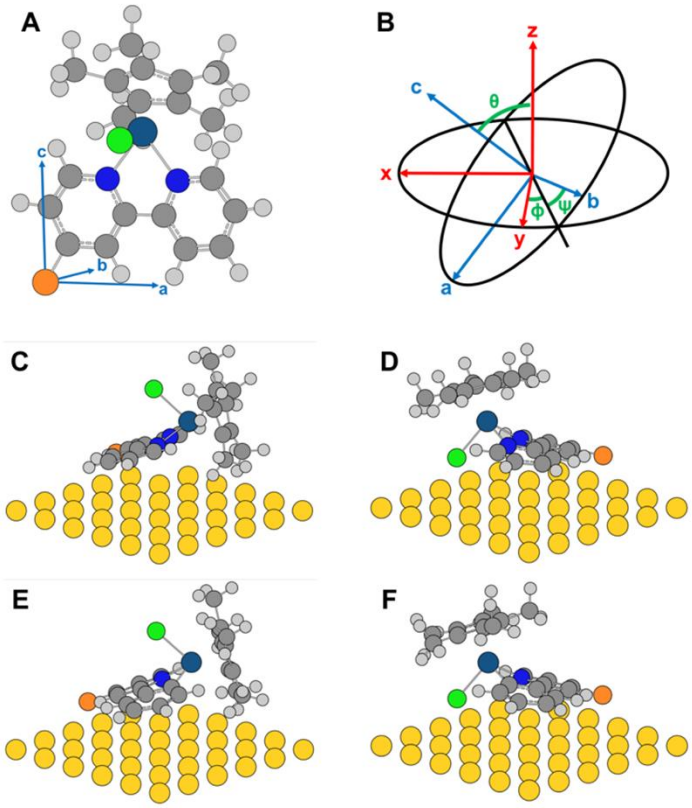

Figure 4.5. (A) Definition of axes in molecular frame (a, b, c) using C1m as an example. (B) Euler angle definition for a molecular orientation relative to the laboratory frame (x, y, z). DFT optimized structures (wB97XD functional and the DEF2SVP basis set) of C1m (C, D) and C2m (E, F) on a Au cluster showing the minimum binding modes of the complexes in the Cl up (C and E) and Cl down (D and F) orientations. Color code for atoms: yellow = Au, orange = S, gray = C, white = H, blue = N, navy = Ir, green = Cl

preferred orientation of the monolayers formed on the surface experimentally. However, the energy difference does motivate direct comparison with PM-IRRAS to confirm the favored orientation under experimental conditions.

In both orientations, the θ_1 and ψ_1 differ by only a few degrees, with the two ranging between 73° and 77° for θ_1 and ψ_1 is slightly off parallel with the surface. The orientation of both the phenylpyridine and bipyridine match previous reports[27, 55] of using similar ligands on Au. In addition, the steric bulk of the Cp* ring does not seem to significantly affect the binding orientation in the Cl up orientation as there is no change in the tilt angle between **C1m** and **C2m**. The similarity

in orientation between the two complexes indicates that there is not a significant impact on binding due to overall charge of the complexes.

The DFT can provide insight into future reactivity studies. In both **C1m** and **C2m** in the Cl down orientation, the Cp* ligand to lies above the complex, at 76° and 74° off normal, respectively. This orientation possibly blocks substitution of the chloride ligand, hindering reactivity. However, in the Cl up orientation for **C1m** and **C2m**, the Cp* ligand lies at 23° off surface normal for both, allowing for substitution and substrate access to the iridium metal center.

4.2.4 Orientation Determination Via PM-IRRAS and DFT

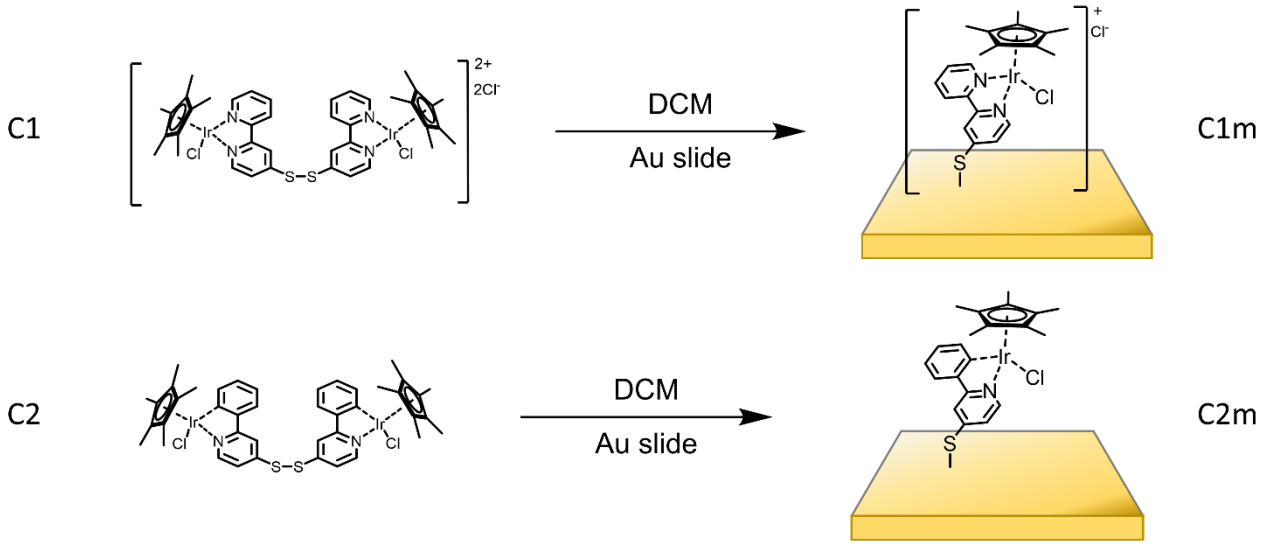

Figure 4.6. Representation of the surface modification of Au (111) with complexes **C1** and **C2** to form monolayers **C1m** and **C2m.**

Polarization modulation infrared reflection-absorption spectroscopy (PM-IRRAS) is a useful tool for determination of monolayer orientation. The intensity of PM-IRRAS spectral lines is dependent on the angle of the transition dipole moment of the vibrational modes. For Au surfaces, there is an electric field amplitude normal to the surface. For transition dipole moments with amplitude normal to the surface, there is an enhancement in signal that is proportional to the magnitude of the dipole moment and angle off normal of that transition. As shown in previous

studies[63-64], the anisotropic amplitude enhancement, the integrated absorbance for a transition dipole moment normal to the surface is three times as large as the integrated absorbance of an isotropic arrangement of molecules in a thin film of same thickness (Equation 4.1).

$$\cos^2\theta = \frac{\int A_{exp}}{3\int A_{sim}} \quad (4.1)$$

Therefore, a comparison can be made between the isotropic FTIR absorbance of complexes **C1**, and **C2**, in a KBr pellet and the anisotropic PM-IRRA spectra. Determination of the orientation of the monolayers was done by direct comparison of the spectral fits of the PM-IRRAS and the simulated IRRAS from the KBr giving an experimentally determined orientation of the TDM. This value was then compared to the TDMs and relative intensity of the transitions determined from the DFT calculations (see Appendix 4.).

To determine which of the calculated orientations exist on the surface, self-assembled monolayers of **C1** and **C2** were made by soaking a clean Au-coated slide in a 1 mM solution of the corresponding complex in DCM for 24 h (Fig. 6). The sample was then washed with DCM and dried under N_2 before characterization. C3 was excluded from this analysis as the monolayer did not survive this washing step with DCM prior to analysis. The narrow line widths of the PM-IRRA spectra indicate a well-ordered, intact monolayer on the surface. Inductively coupled plasma mass spectroscopy (ICP-MS) and X-ray photoelectron spectroscopy (XPS) corroborates this data. ICP-MS determines the surface coverage of **C1m** to be $1.25\text{x}10^{-9}$ mol/cm^2 and **C2m** to be $2.20\text{x}10^{-10}$ mol/cm^2. XPS analysis shows that the Ir remains in the expected +3 oxidation state along with the corresponding Cl, N, and S peaks that are expected in the complexes (see appendix).However, the $\nu_{stretch}$(C-H) frequency was not useful for orientation determination due to the fact that peaks were

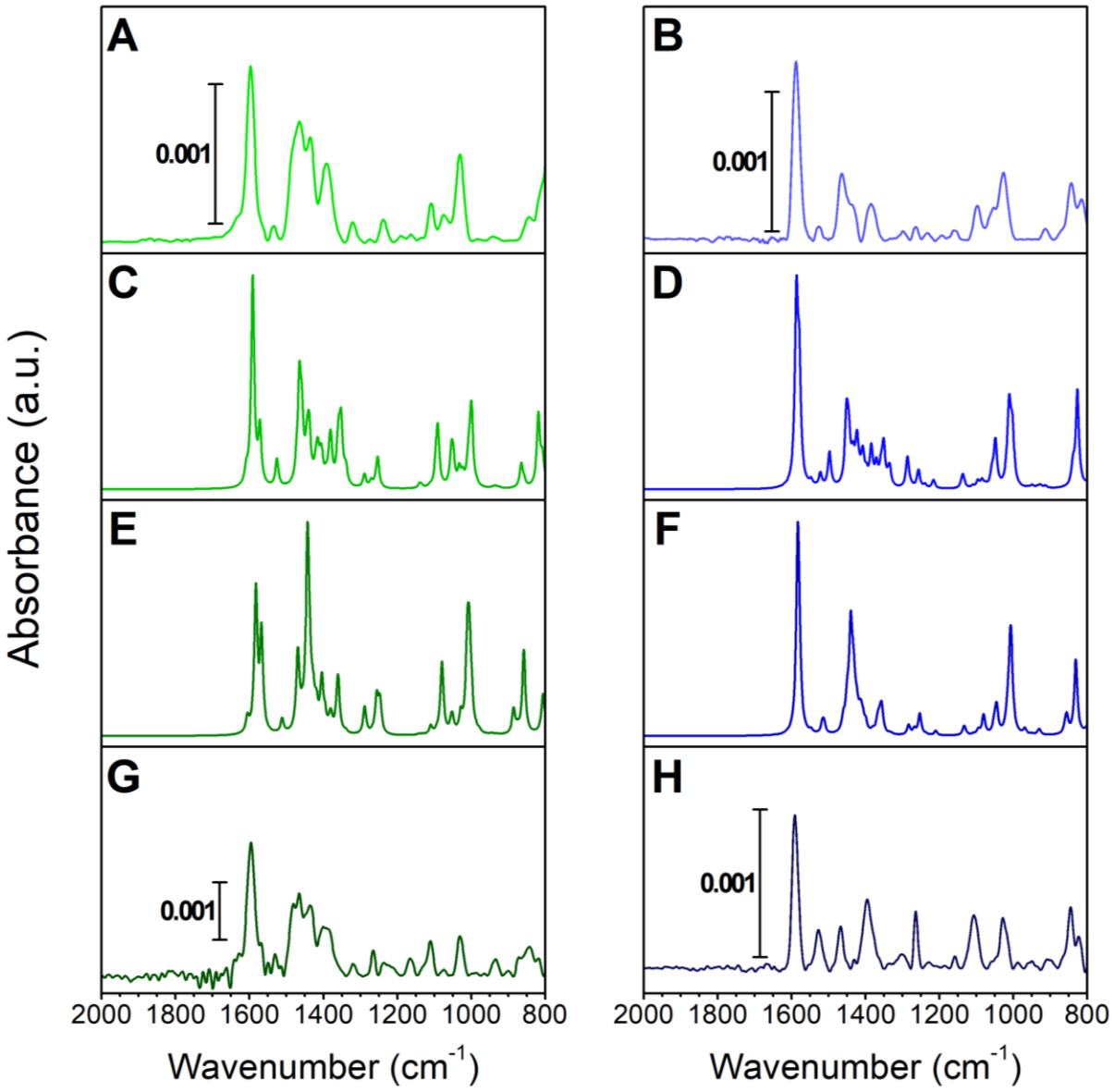

Figure 4.7. Experimental and computational spectra of **C1m** (green) and **C2m** (blue) on Au. The isotropic simulated IRRA spectra from the KBr (A and B), DFT (wB97XD functional and the DEF2SVP basis set with a 0.9485 scaling factor) calculated IR spectra in the Cl up orientation (C and D) and Cl down (E and F) and the PM-IRRA spectra of of the monolayers adsorbed on Au (G and H).

not above the noise level of the instrument. This result indicates that the dipole moments for these transitions have insignificant amplitude normal to the surface.

For **C1m**, there appears to a mix of orientations of the complex present on the surface. A full analysis of the angles of the TDM with respect to orientation and analysis of the PM-IRRAS,

Table 4.2. Experimentally determined and the DFT (wB97XD functional and the DEF2SVP basis set) calculated TDMs with respect to normal for orientation determination of the C1 monolayer on Au used in final determination of the orientation of C1m on the surface.

Peak PM (cm^{-1})	θ (°) ±6°	Calculated Peak Cl down (scaled by 0.9485)	Relative Intensity	TDM angle at peak Cl down	Calculated Peak Cl up (scaled by 0.9485)	Relative Intensity	TDM angle Cl up	Transition (DFT)
1596	40	**1605**	5.9	48	**1609**	4.6	50	bipyridine breathing modes
		1583	56.7	20	**1591**	69.2	16	bipyridine breathing modes
		1567	39.4	32	**1572**	18.5	17	bipyridine breathing modes
		1512	5.7	29	**1526**	9.1	34	bipyridine breathing modes
1488	23	**1471**	10.9	63	**1472**	5.1	40	C-H bending (bipyridine, Cp*)
1466	56	**1468**	21.8	42				C-H bending (bipyridine, Cp*)
		1443	66.1	18	**1465**	31.8	16	C-H bending (Cp*)
		1441	8.8	46	**1458**	19.0	33	C-H bending (Cp*)
					1442	7.7	6	C-H bending (bipyridine, Cp*)
					1438	14.0	70	C-H bending (Cp*)
1441	36	**1436**	14.0	39				C-H bending (bipyridine, Cp*)
		1427	7.5	62	**1415**	7.9	48	C-H bending (Cp*)
		1419	7.2	80				C-H bending (bipyridine, Cp*)
1390	38	**1406**	5.4	54	**1384**	4.8	83	C-H bending (Cp*) Cp* breathing asymmetric
		1404	15.2	30	**1381**	6.1	52	C-H bending (Cp*) Cp* breathing symmetric
		1396	5.3	84				C-H bending (Cp*) Cp* breathing symmetric
					1379	7.8	49	C-H bending, C-C breathing mix (bipyridine)
1318	59	**1362**	10.6	75	**1361**	5.6	64	C-H bending (Cp*) Cp* breathing symmetric
		1359	9.8	80	**1358**	11.0	37	C-H bending (Cp*) Cp* breathing asymmetric
					1352	19.3	31	C-H bending (Cp*) Cp* breathing asymmetric
1229	36	**1288**	11.1	25	**1253**	9.8	29	C-H bending, C-C breathing mix (bipyridine)
		1256	14.5	18				C-H bending, C-C breathing mix (bipyridine)
		1247	12.2	20				C-H bending, C-C breathing mix (bipyridine)
1110	20	**1110**	3.3	37	**1095**	7.2	30	asymmetric C-H bending, C-C breathing mix (bipyridine)
					1090	17.0	16	asymmetric C-H bending, C-C breathing mix (bipyridine)
1075	70	**1079**	28.9	14	**1053**	10.4	19	asymmetric C-H bending (Cp*, bpy), C-C breathing mix (bipyridine)
					1048	7.2	30	asymmetric C-H bending (Cp*, bpy), C-C breathing mix (bipyridine)
1027	60	**1028**	7.0	27	**1032**	5.5	15	asymmetric C-H bending, C-C breathing mix (bipyridine)
		1011	24.7	20	**1007**	6.2	45	C-H bending (Cp*) Cp* and bpy breathing asymmetric
		1009	7.3	35	**1000**	6.4	30	C-H bending (Cp*) Cp* and bpy breathing asymmetric
		1006	5.9	24	**1000**	13.0	37	C-H bending (Cp*) Cp* and bpy breathing asymmetric
		1005	56.7	25				C-H bending (Cp*) Cp* and bpy breathing asymmetric
		1003	39.4	76				C-H bending (Cp*) Cp* and bpy breathing asymmetric
944	41	**999**	5.7	33	**998**	7.8	9	out of plane C-H bending bpy, bpy breathing mix
		885	10.9	65	**865**	7.7	47	out of plane C-H bending, bpy
839	32	**858**	21.8	16	**818**	23.5	21	out of plane C-H bending, bpy
818	61	**806**	66.1	22	**808**	8.4	17	out of plane C-H bending, bpy, bpy breathing mix

DFT and simulated isotropic IRRAS data can be found in the appendix of this chapter. Briefly, the DFT (wB97XD functional and the DEF2SVP basis set) analysis indicates that while the relative intensities of the calculated spectra for the Cl up spectra are a closer approximation of the PM-IRRA spectra, the TDM analysis is inconclusive in determining a preferred orientation. The most intense transition in this region, at 1597 cm^{-1}, arises from the pyridine breathing modes. The experimental orientation of this TDM is determined to be around 40° off normal. DFT indicates that there are four bipyridine breathing modes between 1609 cm^{-1} and 1512 cm^{-1} that differ due to the asymmetry induced by the thiolate in the 4 position of the bipyridine. However, the orientation of the TDM of these transitions are not significantly different for the Cl up and down orientations and when the computed intensity is considered, the average angle of the TDMs is determined to be around 23° off normal, showing relative disagreement with experiment. The more indicative peaks for determining the orientation of the compound on the surface are those transitions that are from the Cp* ligand. As stated above, **Table 4.1** shows the change in tilt angle, θ_2, of the Cp* ligand off surface normal. DFT indicates that this large orientation difference leads to significant differences in the angle of the TDM of the molecular vibrations from the Cp* ligand. The $\nu_{bending}$(C-H) modes of the methyl groups in the Cp* ligand have vibrational transitions between 1480-1420 cm^{-1} and around 1020 cm^{-1} as well as a mix of $\nu_{bending}$(C-H) and $\nu_{breathing}$(C-C) vibrations around 1390 cm^{-1} and 1320 cm^{-1}.[24, 65-66] In this case, the relative IR intensity of the transitions between 1480 cm^{-1} and 1390 cm^{-1} follow the trend for the calculated spectra of the Cl down orientation. In particular, the PM-IRRAS does not have an intense peak around 1443 cm^{-1}. However, for the transitions between 1480 cm^{-1} and 1320 cm^{-1}, the angles of the TDM determined from the DFT either do not differ significantly, the determined experimentally determined TDM does not indicate a preferred orientation. The peak that shows the largest difference between the

isotropic spectra and the PM-IRRAS is at 1075 cm^{-1}. DFT indicates that this peak corresponds to a mix of asymmetric $\nu_{bending}$(C-H) on the Cp* and bipyridine ligand and breathing modes in the pyridines. While DFT indicates that there is not much difference in the determined angle of the TDM (14° for Cl down and 19° for Cl up), the orientation of the monolayer does lower the energy of this transition in the Cl up orientation by 22 cm^{-1} to 1053 cm^{-1}. However, the disagreement between DFT and experiment indicates that this mode cannot be used to determine a preferred orientation. Due to the variance in the angles of the TDM determined experimentally compared to the DFT calculated TDM, the orientation could not be directly obtained from this method alone. When considering the binding energy determined by DFT, it is likely that a mixture of orientations persists on the surface.

Similar to **C1m**, there appears to be a mix of different orientations of **C2m** present on the surface. A full analysis of the angles of the TDM with respect to orientation and analysis of the PM-IRRAS data of **C2** can be found in the section **4.4.12** information. Briefly, the DFT determined TDM for the transition at 1587 cm^{-1} corresponding to the phenylpyridine breathing mode does not change angle significantly depending on orientation of the complex on the surface being 27° and 37° off normal for Cl down and 31° and 36° off normal for Cl up. However, they do differ significantly from the experimentally determined TDM of 61±4°. In addition, there are two peaks in the PM-IRRAS that have significantly lower absorbances as compared to the isotropic spectra and DFT computed spectra. First, the transition at 1448 cm^{-1} has a significant decrease in absorbance for the PM-IRRAS spectra, giving a determined TDM angle of 83±2°. DFT indicates that this band is the combination of transitions primarily of the asymmetric $\nu_{bending}$(C-H) mode of the methyls on the Cp* ligand. the computed TDMs for these transitions are inconclusive for orientation determination. For the Cl down orientation, computed TDM are 44°, 32° and 75° off

Table 4.3. Experimentally determined and the DFT (wB97XD functional and the DEF2SVP basis set) calculated TDMs with respect to normal for orientation determination of the C2 monolayer on Au used in final determination of the orientation of C2m on the surface.

Peak PM (cm^{-1})	θ (°) ±6°	Calculated Peak Cl down (scaled by 0.9485)	Relative Intensity	TDM angle at peak Cl down	Calculated Peak Cl up (scaled by 0.9485)	Relative Intensity	TDM angle Cl up	Transition (DFT)
1589	61	**1581**	88.2	27	**1587**	68.7	31	phenylpyridine breathing modes
		1578	13.9	37	**1579**	40.6	36	phenylpyridine breathing modes
		1513	4.7	85				phenylpyridine breathing mode
1526	7	**1512**	3.9	76	**1522**	5.0	78	C-H bend (Cp*) and Cp* breathing asymmetric
1476	66	**1460**	5.6	45	**1497**	13.2	16	C-H bend (Cp*) and Cp* breathing asymmetric
1448	83	**1449**	10.6	44	**1452**	20.9	37	C-H bend (Cp*) and Cp* breathing asymmetric
		1440	42.7	32	**1449**	7.5	50	C-H bend (Cp*) and Cp* breathing asymmetric
		1432	10.3	75	**1445**	12.8	5	C-H bend (Cp*)
1431	70	**1430**	12.9	21	**1434**	8.3	90	C-H bend (Cp*)
		1424	4.9	84	**1423**	12.9	59	C-H bend (Cp*, phenylpyridine)
		1414	3.7	42	**1408**	6.8	59	C-H bend (Cp*)
1395	36	**1412**	4.4	72	**1397**	3.8	88	C-H bend (Cp*)
1370	50	**1367**	4.7	38	**1384**	5.8	46	C-H bend (Cp*, phenylpyridine)
		1360	4.1	80	**1384**	8.2	44	phenylpyridine bending
		1355	9.9	88	**1370**	7.7	35	C-H bend (Cp*, phenylpyridine)
					1358	5.5	55	C-H bend (Cp*)
					1351	15.1	38	C-H bend (Cp*)
					1334	6.3	66	C-H bending asymmetric (ppy)
1300	69	**1284**	4.4	66	**1286**	11.8	54	C-H bending asymmetric (ppy), phenylpyridine breathing mix
1227	50	**1252**	9.7	29	**1257**	6.8	38	Methyl wagging (Cp*)
1186	64	**1209**	2.0	19	**1216**	3.2	40	Methyl wagging (Cp*)
1158	62	**1134**	2.8	50	**1136**	3.9	51	C-H bending asymmetric (ppy), phenylpyridine breathing mix
1104	41	**1077**	8.8	4	**1096**	2.6	11	C-H bending asymmetric (ppy), phenylpyridine breathing mix
1053	74	**1049**	3.9	75	**1058**	5.5	23	Methyl wagging (Cp*)
		1045	10.1	24	**1049**	12.7	26	Methyl wagging (Cp*)
					1047	4.9	15	C-H bend (Cp*)
1028	66	**1017**	2.2	34	**1011**	26.4	30	Methyl wagging (Cp*)
		1014	5.0	15	**1007**	4.3	14	C-H bending asymmetric (ppy), phenylpyridine breathing mix
		1008	26.2	23	**1002**	15.9	26	C-H bending asymmetric (ppy), phenylpyridine breathing mix
912	73	**1004**	7.7	88	**927**	1.2	65	C-H bending asymmetric (ppy), phenylpyridine breathing mix
		1003	13.8	17				C-H bending asymmetric (ppy), phenylpyridine breathing mix
865	51	**857**	6.8	77	**840**	0.2	69	C-H bending ppy out of plane
845	53	**850**	33.1	13	**839**	7.2	72	C-H bending ppy out of plane
823	59	**797**	2.9	17	**827**	36.1	11	C-H bending Cp* out of plane
815	81	**771**	41.0	34	**796**	0.6	42	C-H bending ppy out of plane

normal and 37°, 50°, and 5° off normal for the Cl up orientation. In addition, the symmetric C-H wagging mode of the methyls on the Cp* ligand at 1053 cm-1 also has a significant decrease in absorbance in the PM-IRRAS when compared to the simulated isotropic spectra. The experimentally determined TDM is 78° off normal. The DFT determines that the TDM is 75° and 25° off normal for the Cl down orientation and 23° and 26° for the Cl up orientation. These two transitions, along with the variance between the other TDM angles determined experimentally and DFT suggests that there is no preference for either orientation. While this disagrees with the relative binding energy determined by DFT, the computed difference 1.8 kcal/mol is small enough that it can be overcome under experimental conditions.

4.3 Conclusion

There is a growing interest in understanding the orientation of molecular catalysts immobilized on surfaces to gather insights to the mechanisms that arise in heterogenized catalysis. We reported the synthesis and characterization of three new Cp*Ir piano-stool complexes, $[Cp^*Ir((2,2'\text{-bipyridine-4-sulfide})Cl]_2[Cl]_2$ (**C1**), $[Cp^*Ir(2\text{-phenylpyridine-4-sulfide})Cl]_2$ (**C2**), and $[Cp^*Ir(2\text{-phenylpyridine-4-thiol})]_3$ (**C3**). By combining DFT and PM-IRRAS, we have determined that there is no preferred orientation for the monolayers formed from **C1m** and **C2m** on Au(111). While the narrow line widths in the PM-IRRA spectra indicate some ordering on the surface, the small difference in binding energy for each orientation determined by DFT suggests that there is likely a mixed orientation **C1** monolayer. Similarly, the PM-IRRAS and DFT calculated spectra for **C2m** suggests that there is a no preference for the Cl down or Cl up orientation. These conclusions show the strength in combining DFT and PM-IRRAS in the determination of orientation of organometallic compounds on Au surfaces even in the absence of a strong IR absorber. In addition,

the mixed orientation of these compounds can provide insights into future reactivity studies in substituting the chloride motif with other substrates.

4.4 Experimental

4.4.1 General Methods and Materials

^{1}H were recorded on a Bruker 300 MHz or JOEL 500 MHz spectrometer. ^{13}C NMR spectra were recorded on a JEOL 500 MHz spectrometer. The ^{13}C and ^{1}H Chemical shifts are referenced to deuterated solvent peaks and reported relative to TMS ($\delta = 0$). ATR-FT-IR spectra were recorded on a Bruker Alpha II. Transmission spectra of KBr pellets of **C1, C2**, and **C3** were acquired on a Thermo Scientific Nicolet 6700. A detailed description of the determination of the simulated IRRAS spectra from these KBr pellets can be found in the SI. Acquired spectra were averaged over 32 scans at a 4 cm^{-1} resolution. Mass spectrometry was performed on a Micromass Quattro Ultima. High resolution Mass spectrometry was performed on an Agilent 6230 Accurate-Mass TOFMS. XPS was performed on a SSF-Kratos AXIS-SUPRA. Mass spectrometry was performed on a Micromass Quattro Ultima. Solvents were received from Fisher Scientific and were dried on a custom solvent system (degassed with Argon and dried over alumina columns) and stored over 3 Å sieves. Deuterated solvents were obtained from Cambridge Isotope Laboratories. Flash column chromatography was performed on a Teledyneisco CombiFlash Rf200 using SiO_2 or neutral alumina loaded columns. 2,2'-bipyridine-N-oxide,[48] 4-chloro-2,2'-bipyridine,[48] 4-thione-2,2'-bipyridine,[27] and di(2,2'-bipyridine)-4-disulfide,[27] $[Ir(Cp^*)Cl_2]_2$[67] were synthesized following previously reported procedures. All other reagents were obtained from commercial sources and used without further purification. Where stated, reactions under nitrogen atmosphere were performed using standard Schlenk-line and Glove Box techniques. Flash column

chromatography was performed on a Teledyneisco CombiFlash Rf200 using SiO_2 or neutral alumina loaded columns.

4.4.2 Synthesis of 4-thione-2,2'-bipyridine (bpy=S)

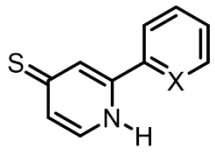

Figure 4.8. Chemical structure of 4-thione-2,2'-bipyridine (bpy=S)

The compound was synthesized using a modified literature procedure,[27] $NaSH \cdot xH_2O$ (16.80 g, 70 %, 209.83 mmol, 20.0 eq.) was added to DMF (100 mL) and the mixture was deoxygenated by sparging with N_2. To it, 4-chloro-2,2'-bipyridine (2.0 g, 10.49 mmol, 1.0 eq.) and KOH (1.77 g, 31.47 mmol, 3.0 eq.) were added and the mixture was deoxygenated by sparging with N_2 again. The mixture was heated to light reflux for 24 h (high reflux rates led to sublimation and subsequent deposition of NaSH in the condenser). After cooling to room temperature (if not cooled to room temperature prior to air exposure a brown precipitate forms that complicates workup and adversely effects the yield) the solution was filtered to remove the white precipitate, rinsed with ethyl acetate and the was solvent was removed from the combined filtrate under reduced pressure. The residue was dissolved in H_2O (50 mL) and the pH was set to neutral with aqueous HCl (2M). The solution was extracted with DCM (3 x 50 mL) and the combined organic layers were washed with brine (50 mL) and dried over $MgSO_4$. The solvent was removed under vacuum and the residue crystallized from EtOH to yield the title compound as a crystalline orange/yellow solid (1.44 g, 7.65 mmol, 73%) Proton NMR matches reference.[50]

^{1}H NMR (300 MHz, CD3CN) δ/ppm 11.34 (bs, 1H), 8.73 - 8.68 (m, 1H), 8.09 (d, J = 8.1 Hz, 1H), 8.00 - 7.91 (m, 2H), 7.56 - 7.47 (m, 2H), 7.31 (dd, J = 6.7, 2.0 Hz, 1H).

4.4.3 Synthesis of di(2,2'-bipyridine)-4-disulfide (bpySSbpy)

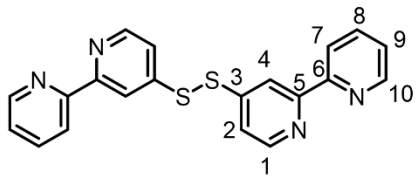

Figure 4.9. Chemical structure of di(2,2'-bipyridine)-4-disulfide (bpySSbpy)

4-thione-2,2'-bipyridine (1.00 g, 5.31 mmol, 1.0 eq.) was solubilized in H_2O (100 mL) by addition of NaOH (233.72 mg, 5.84 mmol, 1.1 eq.). At room temperature a solution of potassium ferricyanide (1.92 g, 5.84 mmol, 1.1 eq.) in H_2O (20 mL) was added. A white precipitate was formed immediately, and the mixture was stirred for 2 h. The precipitate was filtered off and washed thoroughly with water. After drying under vacuum the title compound was obtained as a white solid (949 mg, 2.53 mmol, 95%). Proton and carbon NMR matches reference.[27]

^{1}H NMR (500 MHz, $CDCl_3$) δ /ppm 8.67 (ddd, J = 4.8, 1.7, 0.9 Hz, 1H, H^{10}), 8.61 - 8.51 (m, 2H, $H^{4,1}$), 8.37 (dt, J = 7.9, 1.0 Hz, 1H, H^7), 7.81 (td, J = 7.8, 1.8 Hz, 1H, H^8), 7.44 (dd, J = 5.3, 2.0 Hz, 1H, H^2), 7.32 (ddd, J = 7.5, 4.8, 1.2 Hz, 1H, H^9).

^{13}C{^{1}H} NMR (126 MHz, $CDCl_3$) δ /ppm 156.5 (C^5), 155.4 (C^6), 149.6 (C^1), 149.4 (C^{10}), 148.1 (C^3), 137.2 (C^8), 124.3 (C^9), 121.6 (C^7), 119.8 (C^2), 117.9 (C^4).

IR (ATR) ν_{max} [cm^{-1}]: 3079 (w), 3057 (w), 1573(s), 1561(s), 1537(s), 1447(s), 1377(s), 1271(m), 996(m), 829(m), 790(s), 745(m), 702(s), 657(m), 619(m), 593(m).

4.4.4 Synthesis of 4-thione-2-phenylpyridine (ppy=S)

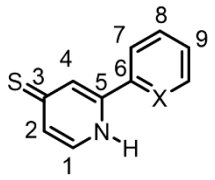

Figure 4.10. Chemical structure of 4-thione-2-phenylpyridine (ppy=S)

4-chloro-2-phenylpyridine (800 mg, 4.22 mmol, 1.0 eq.), NaSH x H_2O (6.76 g, 70 %, 84.37 mmol, 20.0 eq.), and KOH (710.04 mg, 12.66 mmol, 3.0 eq.) were added to DMF (50 mL) and the mixture was deoxygenated by sparging with N_2 (g). The mixture was heated to light reflux for 24 h (high reflux rates lead to sublimation and subsequent deposition of NaSH in the condenser). After cooling to room temperature (if not cooled to room temperature prior to air exposure a brown precipitate forms that complicates workup and adversely effects the yield) the solution was filtered and washed with ethyl acetate and the solvent was removed under reduces pressure. The residue was dissolved in H_2O (50 mL) and pH was set to neutral with aqueous HCl (2M). The precipitate was filtered off and washed with water. After drying under vacuum the title compound was obtained as a yellow solid (Yield: 663 mg, 3.54 mmol, 84%).

^{1}H NMR (300 MHz, $(CD_3)_2SO$) δ/ppm 12.76 (s, 1H, H^{N-H}), 7.78 - 7.73 (m, 2H, H^7), 7.62 (d, J = 6.7 Hz, 1H, H^1), 7.58 - 7.55 (m, 3H, $H^{8, 9}$), 7.47 (d, J = 1.9 Hz, 1H, H^4), 7.18 (dd, J = 6.7, 2.0 Hz, 1H, H^2).

^{1}H NMR (300 MHz, $CDCl_3$) δ/ppm 7.70-7.63 (m, 3H, $H^{1, 7}$), 7.57 (d, J = 1.9 Hz, 1H, H^4), 7.45-7.39 (m, 3H, $H^{8, 9}$), 7.20 (dd, J = 6.3, 1.9 Hz, 1H, H^2).

^{13}C{^{1}H} NMR (126 MHz, $(CD_3)_2SO$) δ/ppm 190.60 (s, C3), 143.37 (s, C^5), 133.66 (s, C1), 132.48 (s, C^6), 130.65 (s, C^9), 129.26 (s, C^8), 128.57 (s, C2), 127.36 (s, C^4), 127.07 (s, C^7).

IR (ATR) ν_{max} [cm^{-1}]: 3300 (b), 3063 (b), 2942 (b), 1606 (s), 1575 (s), 1499 (w), 1471 (m), 1454 (m), 1409 (m), 1301 (m), 1230 (w), 1096 (s), 989 (w), 900 (w), 814 (s), 766 (s),713 (m), 692 (s), 626 (w), 609 (w), 522 (m).

HR-ESI-MS: m/z calcd for $[M]^+$ 188.0527 (found) 188.052; calcd for $[M + H]^+$ 187.0450 (found) 187.0450.

4.4.5 Synthesis of (Cp*Ir(2,2'-bipyridine-4-sulfide)Cl]$_2$[Cl]$_2$ (C1)

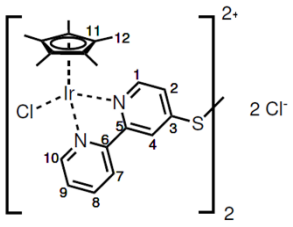

Figure 4.11. Chemical Structure of (Cp*Ir(2,2'-bipyridine-4-sulfide)Cl]$_2$[Cl]$_2$ (C1)

To a solution of $[Cp^*IrCl_2]_2$ (150 mg, 188.28 μmol, 1.0 eq.) in dry DCM (15 mL) in the glovebox, bpySSbpy (70.51 mg, 188.28 μmol, 1.0 eq.) was added. The solution was stirred at room temperature for 1 day. The solvent was removed under vacuum and the resulting yellow solid was purified by precipitation from DCM through the addition of THF. The solid was filtered off and dried under vacuum to yield the title compound as a bright yellow solid (Yield: 197 mg, 164.0 μmol, 87%). The product was isolated as a statistical mixture of diastereomers. Numbers annotated with (') in the NMR data refer to signals corresponding to different diastereomers. The complex is air-stable but highly hygroscopic and was stored and handled in a nitrogen filled glove box.

^{1}H NMR (500 MHz, MeCN) δ/ppm 9.36 (s, 2H, $H^{4/4'}$), 9.32 (s, 2H, $H^{4'/4'}$), 9.17 (d, J = 8.1 Hz, 2H, $H^{7/7'}$), 9.13 (d, J = 8.1 Hz, 2H, $H^{7/7'}$), 8.87 (dd, J = 5.6, 1.1 Hz, 4H, $H^{10, 10'}$), 8.81 (d, J = 6.2 Hz, 2H, $H^{1/1'}$), 8.78 (d, J = 6.2 Hz, 2H, $H^{1/1'}$), 8.20 (t, J = 7.9 Hz, 4H, $H^{8, 8'}$), 8.07 (dd, J = 6.2,

2.0 Hz, 2H, $H^{2/2'}$), 8.00 (dd, J = 6.2, 2.0 Hz, 2H, $H^{2/2'}$), 7.81 - 7.74 (m, 4H, $H^{9, 9'}$), 1.64 - 1.60 (m, J = 1.2 Hz, 60H, $H^{12, 12'}$).

$^{13}C\{^{1}H\}$ NMR (126 MHz, MeCN) δ/ppm 156.26 (s, $C^{5/5'}$), 156.21 (s, $C^{5/5'}$), 155.63 (s, $C^{6, 6'}$), 152.72 (s, $C^{10, 10'}$), 152.67 (s, $C^{3/3'}$), 152.64 (s, $C^{3/3'}$), 152.43 (s, $C^{1/1'}$), 152.29 (s, $C^{1/1'}$), 141.24 (s, $C^{8/8'}$), 141.22 (s, $C^{8/8'}$), 130.09 (s, $C^{9, 9'}$), 126.33 (s, $C^{2/2'}$), 126.30 (s, $C^{7/7'}$), 126.28 (s, $C^{7/7'}$), 125.97 (s, $C^{2/2'}$), 122.93 (s, $C^{4/4'}$), 122.82 (s, $C^{4/4'}$), 90.42 (s, C^{11}), 8.78 (s, C^{12}).

IR (ATR) ν_{max} [cm^{-1}]: 3059 (w), 2972 (m), 2916 (w), 2873 (w), 1595 (s), 1537 (w), 1463 (m), 1431 (m), 1390 (m), 1322 (w), 1238 (w), 1110 (m), 1063 (w), 1031 (m), 849 (w), 812 (w), 790 (s), 754 (w), 715 (w), 594 (m).

HR-ESI-MS: m/z calcd. for [M - 2Cl]2+ 550.0804 (found) 550.0807 (isotope pattern matches simulated spectrum, Fig. S31).

4.4.6 Synthesis of [Cp*Ir(2-phenylpyridine-4-sulfide)Cl]$_2$ (C2)

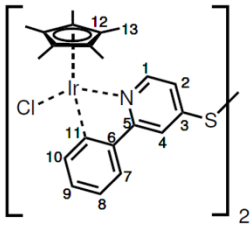

Figure 4.12. Chemical Structure of [Cp*Ir(2-phenylpyridine-4-sulfide)Cl]$_2$ (C2)

[Cp*$IrCl_2$]$_2$ (213.88 mg, 268.45 μmol, 1.0 eq.), di(2-phenylpyridine)-4-disulfide (100.00 mg, 268.45 μmol, 1.0 eq.) and potassium acetate (158.08 mg, 1.61 mmol, 6.0 eq.) were mixed in dry DCM and stirred at room temperature for 22 h. The reaction mixture was filtered over Celite® and the solvent was removed from the filtrate. The orange residue was purified by flash column chromatography (SiO2, DCM to DCM/10% MeOH). The solvent was removed under vacuum to yield the title compound as a bright orange solid (189 mg, 172.4 μmol, 64%). The product was

isolated as a statistical mixture of diastereomers. Numbers annotated with (') in the NMR data refer to signals corresponding to different diastereomers.

^{1}H NMR (500 MHz, CDCl3) δ/ppm 8.57 - 8.56 (m, 2H, $H^{1, 1'}$), 7.91 - 7.87 (m, 2H, $H^{4, 4'}$), 7.83-7.79 (m, 2H, $H^{10, 10'}$), 7.68 -7.62 (m, 2H, $H^{7, 7'}$), 7.24 - 7.15 (m, 4H, $H^{9, 9', 2, 2'}$), 7.06 - 6.99 (m, 2H, $H^{8, 8'}$), 1.69 - 1.64 (m, 30H, $H^{13, 13'}$).

^{13}C{^{1}H} NMR (126 MHz, CDCl3) δ/ppm 167.52 ($C^{5/5'}$), 167.36 ($C^{5/5'}$), 164.38 ($C^{11/11'}$), 164.34 ($C^{11/11'}$), 151.40 ($C^{1/1'}$), 151.23 ($C^{1/1'}$), 147.93 ($C^{3/3'}$), 147.84 ($C^{3/3'}$), 143.17 ($C^{6/6'}$), 143.09 ($C^{6/6'}$), 136.07 ($C^{10,10'}$), 131.70 ($C^{9/9'}$), 131.68 ($C^{9/9'}$), 124.30 ($C^{7,7'}$), 122.37 ($C^{8/8'}$), 122.32 ($C^{8/8'}$), 118.73 ($C^{2/2'}$), 118.49 ($C^{2/2'}$), 115.40 ($C^{4/4'}$), 115.07 ($C^{4/4'}$), 88.90 ($C^{12,12'}$), 9.10 ($C^{13,13'}$).

IR (ATR) ν_{max} [cm^{-1}]: 2956 (m), 2920 (s), 2851 (s), 1721 (w), 1686 (w), 1587 (s), 1460 (s), 1378 (m), 1261 (m), 1090 (m), 1026 (m), 822 (m), 806 (m), 772 (m), 729 (s).

HR-ESI-MS: m/z calcd. for [M - 2Cl]2+ 512.1085 (found) 512.1090 isotope pattern matches simulated spectrum (SI Fig. S32).

4.4.7 Synthesis of [Cp*Ir(2-phenylpyridine-4-thiol)]$_3$ (C3)

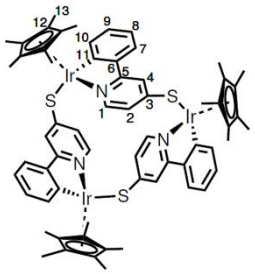

Figure 4.13. Chemical structure of [Cp*Ir(2-phenylpyridine-4-thiol)]3 (C3)

To degassed DCM (10 mL) in a Schlenk flask $[Cp \cdot IrCl_2]_2$ (176.45 mg, 221.47 μmol, 1.1 eq.), 1,2-bis(2-phenylpyridin-4-yl)disulfide (75 mg, 201.34 μmol, 1.0 eq.), potassium acetate (118.56 mg, 1.21 mmol, 6.0 eq.) were added, resulting in an orange solution with a white precipitate. The mixture was stirred at room temperature for 1 day. The solid was filtered off and the solvent was

removed from the filtrate under vacuum. The resulting orange residue was purified by flash column chromatography (SiO2, DCM to DCM/5% MeOH). The first peak was isolated as a bright yellow/orange solid (40 mg, 26.01 μmol, 19 %). Crystals suitable for X-ray diffraction were grown by slow evaporation of pentane into a solution of the complex in 1,2-dichlorobenzene.

^{1}H NMR (500 MHz, $CDCl_3$) δ/ppm 8.01 (d, J = 6.3 Hz, 3H, H^1), 7.44 (d, J = 1.9 Hz, 3H, H^4), 7.42 (d, J = 7.6 Hz, 3H, H^{10}), 7.29 (dd, J = 7.8, 0.9 Hz, 3H, H^7), 7.07 (td, J = 7.5, 1.3 Hz, 3H, H^9), 6.89 (td, J = 7.7, 1.1 Hz, 3H, H^8), 6.74 (dd, J = 6.3, 2.0 Hz, 3H, H^2), 1.80 (s, 45H, H^{13}).

^{13}C{^{1}H} NMR (126 MHz, $CDCl_3$) δ/ppm 163.33 (s, C^3), 162.30 (s, C^{11}), 158.53 (s, C^5), 148.02 (s, C^1), 144.44 (s, C^6), 134.29 (s, C^{10}), 130.16 (s, C^9), 123.62 (s, C^7), 123.26 (s, C^2), 122.03 (s, C^8), 121.31 (s, C^4), 89.97 (s, C^{12}), 9.06 (s, C^{13}).

IR (ATR) ν_{max} [cm^{-1}]: 3045 (w), 2916 (w), 2851 (w), 1738 (w), 1589 (s), 1507 (w), 1466 (m), 1444 (m), 1381 (m), 1292 (w), 1263 (w), 1235 (w), 1156 (w), 1106 (m), 1098 (m), 1016 (m), 859 (w), 819 (m), 770 (m), 725 (s), 714 (w), 663 (w), 638 (w), 611 (w), 537 (w).

HR-ESI-MS: m/z calcd. for $[M + H]^+$ 1538.3329 (found) 1538.3357 (isotope pattern matches a $[M]^+$ / $[M+H]^+$ ratio of 0.58 / 0.42, Fig. S33).

4.4.8 Preparation of Au and self-assembled monolayers

All samples for PM-IRRAS, ICP-MS, and XPS were prepared on optically flat Au substrates consisting of a layer of Cr (1-4 nm) and Au (200-300 nm) evaporated onto borosilicate glass slides. The substrates were cleaned by dipping in piranha solution (3:1 H_2SO_4:30% H_2O_2) for 1-2 minutes. ***Caution, piranha solutions are extremely energetic and may result in explosions if not handled with extreme caution.*** The slides were then washed with water and dried. Prior to use, slides were flame treated to remove surface water and then added to 1 mM solutions of the compound in

dichloromethane overnight. The slides were then washed with dichloromethane and dried under a stream of nitrogen before analysis.

4.4.9 Polarization Modulation Infrared Reflection-Absorption Spectroscopy (PM-IRRAS)

PM-IRRAS spectra were obtained on a Bruker 55 FTIR with a Bruker PMA 37 accessory under a dry air atmosphere using a Parker Balston Purge Gas Generator. Polarization was achieved using a PEM-90-D ZnSe Photoelestic Modulator (Hinds Instruments) operating at 50 kHz and half-wave retardation coupled with a Synchronous Sampling Demodulator (GWC Instruments). A liquid nitrogen cooled mercury cadmium telluride detector equipped with a BaF_2 window detector was used and set at an angle of incidence of 88˚ with respect to normal. Scans were collected for 2000 scans each sum and difference with 4 cm^{-1} resolution and maximum dephasing at either 1600 cm^{-1} and 3000 cm^{-1} to minimize PM error across the entire spectra. Baseline was established by previous literature precedent by normalization to a reference (blank) slide.[31, 68-69] Blank slides were made via the same cleaning method as the samples and allowed to soak in dichloromethane for the same amount of time as the samples. Once baseline corrected, the PM-IRRAS spectra was converted to absorbance values by $A = 0.0223\left[\left(\frac{\Delta I}{I}\right)_{norm} - 1\right]$ where $[\Delta I/I]_{norm}$ is the baseline corrected PM-IRRAS signal.[31] Detailed experimental methods for the fitting of the PM-IRRA spectra for the orientation determination can be found in the SI.

4.4.10 Single Crystal X-ray Diffraction

Single crystal X-ray data was collected on a Bruker Apex II-Ultra CCD diffractometer equipped with MoKα radiation (λ = 0.71073 Å). The crystals were mounted on a Cryo-loop with Paratone oil. Data were collected under a nitrogen gas stream at 100 K using ω and φ scans. Data were integrated using the Bruker SAINT software program and scaled using the SADABS software program. All structures were solved via direct methods with SHELXS[70] and refined by full-matrix

least squares procedures using SHELXL21 within the Olex2 small- molecule solution, refinement, and analysis software package.[71] All nonhydrogen atoms were refined anisotropically by full-matrix least-squares (SHELXL-2014). Crystallographic data, structure refinement parameters, and additional notes on structure refinement are summarized in the Appendix.

4.4.11 Simulated isotropic IRRAS spectra.

The method for the simulation of isotropic IRRA spectra from transmission spectra of C1 and C2 followed previous literature precedent.[31, 45-46, 63-64, 72-74] Briefly, the simulation of isotropic IRRA spectra requires the known experimentally determined molar absorptivity, refractive index, and estimated molecular density, surface coverage, and monolayer thickness of the analyte and the refractive index and molar absorptivity of the Au surface. The molar absorptivity is determined from a transmission FTIR spectra of C1 and C2 were obtained on KBr pellets of known concentrations and thickness (Figure SX). The refractive index is determined via the Kramers-Kronig transformation following molar absorptivity determination (Figure SX). The molecular density of C1 and C2 is estimated from the C3 crystal structure. While this is a starting point for the estimation of the density of C1 and C2, calculated spectra were also made using a high (2.0 g/cm^3) and low (1.2 g/cm^3) estimation of the density to bracket the determined angle of the transition dipole moments. The high and low estimates were chosen as 91% of all Ir piano-stool complexes that contained both a halide and either a 2,2-bipyridne or phenylpyridine moiety in the Cambridge Structural Database had a density between these two values (Figure S45, 78 structures). The surface coverage determined via ICP-MS of the monolayers. The monolayer thickness of C1 and C2 was determined as the average of the distance from the surface and the atom farthest from the surface to the S atom attached to the surface of C1m and C2m monolayers in the Cl up and Cl down orientations in DFT. Spectra was then simulated used methods published elsewhere, using

an angle of incidence of the IRRAS as 88° to match the experimental PM-IRRAS.[46, 73-74] Overall, due to the estimation of the density, the method has an average tolerance of ±6° (average difference between initial estimation and bracketed high and low values) for the determined angle of the transition dipole moment (TDM).

4.4.12 Comparison of the PM-IRRAS and the Simulated IRRAS via Spectral Fitting.

The comparison of the PM-IRRAS and simulated isotropic spectra follows previously reported methods.[31, 46, 73-74] Briefly, spectral fits were performed in OriginPro. Following previous lab precedent, all spectra were smoothed with at 9 cm-1 resolution and fit.[39, 75] Second derivative analysis provided by the OMNIC Series software allowed for the resolution of bands. The PM-IRRA spectra were fit with Gaussian line shapes and simulated IRRAS spectra were fit with a mixture of Lorentzian and Gaussian line shapes to obtain the most accurate peak areas.[31, 74, 76-77]

4.4.13 Determination of Surface Coverage by ICP-MS

Inductively coupled plasma mass spectrometry (ICP-MS) was conducted on a Thermo iCAP RQ ICP-MS instrument with prepared standards and samples. The standards were prepared from an iridium standard with a concentration of 1μg/ml in 10-20% HCl solution from Acros Organics. Trace metal concentrated HCl (Fisher Chemical) and trace metal concentrated HNO_3 (Fisher Chemical) were used and diluted to the appropriate concentrations. The standards were prepared in 1% HCl with concentrations of 1000ppb Ir, 100ppb Ir, 10ppb Ir, 1ppb Ir, and 0 ppb. The samples were digested in a 17% HCl solution overnight then diluted with 18.2 MΩ·cm water to a 1% HCl solution for analysis. The digestion Teflon tube was cleaned prior to use with a 1% HNO_3 solution and left to air dry.

4.4.14 Characterization of SAMs by X-ray photoelectron spectroscopy (XPS).

XPS was done on gold slides prepared identically to the PM-IRRAS and ICP-MS experiments. XPS survey spectra were recorded with a pass energy of 160 eV with a 1eV step. High-resolution spectra of the Au 4f, C 1s, N 1s, S 2p, Cl 2p, and Ir 4f/Au $5p_{3/2}$ were recorded with a pass energy of 20 eV. Data processing and analysis was done using CasaXPS. The binding energy of all spectra was energy corrected to the Au $4f_{7/2}$ line at 84.0 eV as reference. Background correction was carried out using a Shirley background for all signals. High-resolution spectra were fit with a mix of Gaussian and Lorentzian line shapes to obtain the most accurate peak areas.

4.4.15 Computational Benchmarking

Benchmarking DFT calculations were performed with the ωB97X-D functional[58] as well as the Perdew-Burke-Ernzerhof (PBE) functional[78] with Grimme's D3 dispersion with Becke-Johnson damping (D3-BJ).[79] The inclusion of dispersion was considered to be crucial to correctly describing ligand-Au interactions, and the PBE D3-BJ method had previously been shown to provide accurate and computationally accessible modeling bonds between molecules and Au.[80] Initial calculations were performed with the 6-31G(d,p) basis set[59-61] on all nonmetal atoms and the LANL2DZ basis set and pseudopotential[81] on Ir and Au. Although the minimum energy binding geometries were nearly identical for the two functionals (Table S5, S6 and 1), it was found that the ωB97X-D stretching frequencies and IR intensities (after 0.9485 correction) showed much better agreement with the experiment (Figure S35 and S36). This was particularly evident for the highest intensity mode at ~1600 cm^{-1} corresponding to a bpy breathing mode; this peak showed low intensity using PBE D3-BJ, but was the most intense peak using ωB97X-D. Given the poor agreement of the PBE D3-BJ spectrum, only the ωB97X-D functional was used for further calculations with the larger DEF2SVP basis set and pseudopotential[62] on Ir and Au (Tables S11

and S12). These results were relatively similar to the LANL2DZ results but were used for all analyses in the main text since they corresponded to a larger, more polarizable metal basis set.

4.4.16 Comparison of the Experimental and DFT calculated TDMs for orientation determination.

To determine the orientation of the monolayers on the Au surface, a comparison between the experimentally determined TDM and DFT (ωB97X-D functional, DEF2SVP basis set) calculated TDM moments. Due to resolution limitations, the peaks determined experimentally correspond to multiple transitions calculated by DFT. By considering all of the possible TDM calculated for a select mode with the experimentally determined data with similar energy, a comparison can be made. For example, the experimentally determined angle of the transition dipole moment for the bipyridine breath mode was determined to be 40° off normal. DFT calculated 4 bipyridine breathing modes. The average for the 4 transitions is about 26° for the Cl down and 20° for the Cl up orientation.

4.5 Acknowledgements

Chapter 4, in full has been submitted for publication of the material entitled, Miller, C.J.; Brunner, F.M.; Kelly, H.R.; Cheung, P.L.; Torquato, N. Gembicky, M.; Okuno, S.; Chan, T.; Bastista, V.S.; Kubiak, C.P. PM-IRRAS and DFT investigation of the surface orientation of new Ir piano-stool complexes attached to Au (111). *In review.* The dissertation author is the primary author of this material. We acknowledge Joseph Palasz, Sarah Tyler, Dr. Michael Neville, and Prof. Tianquan (Tim) Lian for invaluable discussions and the UCSD Molecular Mass Spectrometry Facility for HRMS sample analysis. This work was supported by the Air Force Office of Scientific Research under Award No. FA9550-17-0198. The authors acknowledge Dr. Ich Tran and the use of facilities and instrumentation at the UC Irvine

Materials Research Institute (IMRI), which is supported in part by the National Science Foundation through the UC Irvine Materials Research Science and Engineering Center (DMR-2011967). XPS was performed using instrumentation funded in part by the National Science Foundation Major Research Instrumentation Program under grant no. CHE-1338173.

4.6 References

1. Barrett, S. M.; Stratakes, B. M.; Chambers, M. B.; Kurtz, D. A.; Pitman, C. L.; Dempsey, J. L.; Miller, A. J. M., Mechanistic basis for tuning iridium hydride photochemistry from H2 evolution to hydride transfer hydrodechlorination. *Chem. Sci.* **2020,** *11* (25), 6442-6449.

2. Pitman, C. L.; Miller, A. J. M., Molecular Photoelectrocatalysts for Visible Light-Driven Hydrogen Evolution from Neutral Water. *ACS Catal.* **2014,** *4* (8), 2727-2733.

3. Stratakes, B. M.; Miller, A. J. M., H2 Evolution at an Electrochemical "Underpotential" with an Iridium-Based Molecular Photoelectrocatalyst. *ACS Catal.* **2020,** *10* (16), 9006-9018.

4. Brereton, K. R.; Bonn, A. G.; Miller, A. J. M., Molecular Photoelectrocatalysts for Light-Driven Hydrogen Production. *ACS Energy Lett.* **2018,** *3* (5), 1128-1136.

5. Barrett, S. M.; Slattery, S. A.; Miller, A. J. M., Photochemical Formic Acid Dehydrogenation by Iridium Complexes: Understanding Mechanism and Overcoming Deactivation. *ACS Catal.* **2015,** *5* (11), 6320-6327.

6. Ogo, S.; Makihara, N.; Kaneko, Y.; Watanabe, Y., pH-Dependent Transfer Hydrogenation, Reductive Amination, and Dehalogenation of Water-Soluble Carbonyl Compounds and Alkyl Halides Promoted by Cp*Ir Complexes. *Organometallics* **2001,** *20*, 4903.

7. Abura, T.; Ogo, S.; Watanabe, Y.; Fukuzumi, S., Isolation and Crystal Structure of a Water-Soluble Iridium Hydride: A Robust and Highly Active Catalyst for Acid-Catalyzed Transfer Hydrogenations of Carbonyl Compounds in Acidic Media. *J. Am. Chem. Soc.* **2003,** *125*, 4149.

8. Ngo, A. H.; Ibanez, M.; Do, L. H., Catalytic Hydrogenation of Cytotoxic Aldehydes Using Nicotinamide Adenine Dinucleotide (NADH) in Cell Growth Media. *ACS Catal.* **2016,** *6* (4), 2637-2641.

9. Brewster, T. P.; Miller, A. J. M.; Heinekey, D. M.; Goldberg, K. I., Hydrogenation of Carboxylic Acids Catalyzed by Half-Sandwich Complexes of Iridium and Rhodium. *J. Am. Chem. Soc.* **2013,** *135* (43), 16022-16025.

10. Kawahara, R.; Fujita, K.-i.; Yamaguchi, R., Dehydrogenative Oxidation of Alcohols in Aqueous Media Using Water-Soluble and Reusable Cp*Ir Catalysts Bearing a Functional Bipyridine Ligand. *J. Am. Chem. Soc.* **2012,** *134* (8), 3643-3646.

11. Himeda, Y.; Onozawa-Komatsuzaki, N.; Miyazawa, S.; Sugihara, H.; Hirose, T.; Kasuga, K., pH-Dependent Catalytic Activity and Chemoselectivity in Transfer Hydrogenation Catalyzed by Iridium Complex with 4,4′-Dihydroxy-2,2′-bipyridine. *Chem. Eur. J.* **2008,** *14*, 11076.

12. Liu, J.-t.; Yang, S.; Tang, W.; Yang, Z.; Xu, J., Iridium-catalyzed efficient reduction of ketones in water with formic acid as a hydride donor at low catalyst loading. *Green Chem.* **2018,** *20* (9), 2118-2124.

13. Sasayama, A. F.; Moore, C. E.; Kubiak, C. P., Electronic effects on the catalytic disproportionation of formic acid to methanol by [Cp*IrIII(R-bpy)Cl]Cl complexes. *Dalton Trans.* **2016,** *45* (6), 2436-2439.

14. Onishi, N.; Iguchi, M.; Yang, X.; Kanega, R.; Kawanami, H.; Xu, Q.; Himeda, Y., Development of Effective Catalysts for Hydrogen Storage Technology Using Formic Acid. *Adv. Energy Mater.* **2019,** *9* (23), 1801275.

15. Himeda, Y.; Onozawa-Komatsuzaki, N.; Sugihara, H.; Kasuga, K., Simultaneous Tuning of Activity and Water Solubility of Complex Catalysts by Acid−Base Equilibrium of Ligands for Conversion of Carbon Dioxide. *Organometallics* **2007,** *26* (3), 702-712.

16. Sanz, S.; Benítez, M.; Peris, E., A New Approach to the Reduction of Carbon Dioxide: CO2 Reduction to Formate by Transfer Hydrogenation in iPrOH. *Organometallics* **2010,** *29*, 275.

17. Ogo, S.; Kabe, R.; Hayashi, H.; Harada, R.; Fukuzumi, S., Mechanistic investigation of CO2 hydrogenation by Ru(ii) and Ir(iii) aqua complexes under acidic conditions: two catalytic systems differing in the nature of the rate determining step. *Dalton Trans.* **2006,** (39), 4657-4663.

18. An, L.; Chen, R., Direct formate fuel cells: A review. *J. Power Sources* **2016,** *320*, 127-139.

19. Bullock, R. M.; Das, A. K.; Appel, A. M., Surface Immobilization of Molecular Electrocatalysts for Energy Conversion. *Chem. Eur. J.* **2017,** *23* (32), 7626-7641.

20. Poddutoori, P. K.; Thomsen, J. M.; Milot, R. L.; Sheehan, S. W.; Negre, C. F. A.; Garapati, V. K. R.; Schmuttenmaer, C. A.; Batista, V. S.; Brudvig, G. W.; van der Est, A., Interfacial electron transfer in photoanodes based on phosphorus(v) porphyrin sensitizers co-deposited on SnO2 with the Ir(III)Cp* water oxidation precatalyst. *J. Mater. Chem. A* **2015,** *3* (7), 3868-3879.

21. Moore, G. F.; Blakemore, J. D.; Milot, R. L.; Hull, J. F.; Song, H.-e.; Cai, L.; Schmuttenmaer, C. A.; Crabtree, R. H.; Brudvig, G. W., A visible light water-splitting cell with a photoanode formed by codeposition of a high-potential porphyrin and an iridium water-oxidation catalyst. *Energy Environ. Sci.* **2011,** *4* (7), 2389-2392.

22. Joya, K. S.; Subbaiyan, N. K.; D'Souza, F.; de Groot, H. J. M., Surface-Immobilized Single-Site Iridium Complexes for Electrocatalytic Water Splitting. *Angew. Chem. Int. Ed.* **2012,** *51* (38), 9601-9605.

23. Tong, H.; Jiang, Y.; Zhang, Q.; Li, J.; Jiang, W.; Zhang, D.; Li, N.; Xia, L., Enhanced Interfacial Charge Transfer on a Tungsten Trioxide Photoanode with Immobilized Molecular Iridium Catalyst. *ChemSusChem* **2017,** *10* (16), 3268-3275.

24. Materna, K. L.; Rudshteyn, B.; Brennan, B. J.; Kane, M. H.; Bloomfield, A. J.; Huang, D. L.; Shopov, D. Y.; Batista, V. S.; Crabtree, R. H.; Brudvig, G. W., Heterogenized Iridium Water-Oxidation Catalyst from a Silatrane Precursor. *ACS Catal.* **2016,** *6* (8), 5371-5377.

25. Lattimer, J. R. C.; Blakemore, J. D.; Sattler, W.; Gul, S.; Chatterjee, R.; Yachandra, V. K.; Yano, J.; Brunschwig, B. S.; Lewis, N. S.; Gray, H. B., Assembly, characterization, and electrochemical properties of immobilized metal bipyridyl complexes on silicon(111) surfaces. *Dalton Trans.* **2014,** *43* (40), 15004-15012.

26. Ge, A.; Rudshteyn, B.; Videla, P. E.; Miller, C. J.; Kubiak, C. P.; Batista, V. S.; Lian, T., Heterogenized Molecular Catalysts: Vibrational Sum-Frequency Spectroscopic, Electrochemical, and Theoretical Investigations. *Acc. Chem. Res.* **2019,** *52* (5), 1289-1300.

27. Clark, M. L.; Ge, A.; Videla, P. E.; Rudshteyn, B.; Miller, C. J.; Song, J.; Batista, V. S.; Lian, T.; Kubiak, C. P., CO2 Reduction Catalysts on Gold Electrode Surfaces Influenced by Large Electric Fields. *J. Am. Chem. Soc.* **2018**.

28. Chidsey, C. E. D.; Loiacono, D. N., Chemical functionality in self-assembled monolayers: structural and electrochemical properties. *Langmuir* **1990,** *6* (3), 682-691.

29. Ulman, A., Formation and Structure of Self-Assembled Monolayers. *Chem. Rev.* **1996,** *96* (4), 1533-1554.

30. Golden, W. G.; Dunn, D. S.; Overend, J., A method for measuring infrared reflection—Absorption spectra of molecules adsorbed on low-area surfaces at monolayer and submonolayer concentrations. *J. Catal.* **1981,** *71* (2), 395-404.

31. Buffeteau, T.; Desbat, B.; Turlet, J. M., Polarization Modulation FT-IR Spectroscopy of Surfaces and Ultra-thin Films: Experimental Procedure and Quantitative Analysis. *Appl. Spectrosc.* **1991,** *45* (3), 380-389.

32. Monyoncho, E. A.; Zamlynny, V.; Woo, T. K.; Baranova, E. A., The utility of polarization modulation infrared reflection absorption spectroscopy (PM-IRRAS) in surface and in situ studies: new data processing and presentation approach. *Analyst* **2018,** *143* (11), 2563-2573.

33. Lebec, V.; Landoulsi, J.; Boujday, S.; Poleunis, C.; Pradier, C. M.; Delcorte, A., Probing the Orientation of β-Lactoglobulin on Gold Surfaces Modified by Alkyl Thiol Self-Assembled Monolayers. *J. Phys. Chem. C* **2013,** *117* (22), 11569-11577.

34. Silien, C.; Buck, M.; Goretzki, G.; Lahaye, D.; Champness, N. R.; Weidner, T.; Zharnikov, M., Self-Assembly of a Pyridine-Terminated Thiol Monolayer on Au(111). *Langmuir* **2009,** *25* (2), 959-967.

35. Luo, W.; Legge, S. M.; Luo, J.; Lagugné-Labarthet, F.; Workentin, M. S., Investigation of Au SAMs Photoclick Derivatization by PM-IRRAS. *Langmuir* **2020,** *36* (4), 1014-1022.

36. Bin, X.; Zawisza, I.; Goddard, J. D.; Lipkowski, J., Electrochemical and PM-IRRAS Studies of the Effect of the Static Electric Field on the Structure of the DMPC Bilayer Supported at a Au(111) Electrode Surface. *Langmuir* **2005,** *21* (1), 330-347.

37. Kékedy-Nagy, L.; Ferapontova, E. E.; Brand, I., Submolecular Structure and Orientation of Oligonucleotide Duplexes Tethered to Gold Electrodes Probed by Infrared Reflection Absorption Spectroscopy: Effect of the Electrode Potentials. *J. Phys. Chem. B* **2017,** *121* (7), 1552-1565.

38. Zamlynny, V.; Zawisza, I.; Lipkowski, J., PM FTIRRAS Studies of Potential-Controlled Transformations of a Monolayer and a Bilayer of 4-Pentadecylpyridine, a Model Surfactant, Adsorbed on a Au(111) Electrode Surface. *Langmuir* **2003,** *19* (1), 132-145.

39. Wang, J.; Clark, M. L.; Li, Y.; Kaslan, C. L.; Kubiak, C. P.; Xiong, W., Short-Range Catalyst–Surface Interactions Revealed by Heterodyne Two-Dimensional Sum Frequency Generation Spectroscopy. *J. Phys. Chem. Lett.* **2015,** *6* (21), 4204-4209.

40. Petersen, F.; Lautenschläger, I.; Schlimm, A.; Flöser, B. M.; Jacob, H.; Amirbeigiarab, R.; Rusch, T. R.; Strunskus, T.; Magnussen, O.; Tuczek, F., Molybdenum tricarbonyl complex functionalised with a molecular triazatriangulene platform on Au(111): surface spectroscopic characterisation. *Dalton Trans.* **2021,** *50* (3), 1042-1052.

41. Schlimm, A.; Stucke, N.; Flöser, B. M.; Rusch, T.; Krahmer, J.; Näther, C.; Strunskus, T.; Magnussen, O. M.; Tuczek, F., Influence of a Metal Substrate on Small-Molecule Activation Mediated by a Surface-Adsorbed Complex. *Chem. Eur. J.* **2018,** *24* (42), 10732-10744.

42. Jacob, H.; Kathirvel, K.; Petersen, F.; Strunskus, T.; Bannwarth, A.; Meyer, S.; Tuczek, F., Grafting of Functionalized [Fe(III)(salten)] Complexes to Au(111) Surfaces via Thiolate Groups: Surface Spectroscopic Characterization and Comparison of Different Linker Designs. *Langmuir* **2013,** *29* (27), 8534-8543.

43. Orchanian, N. M.; Hong, L. E.; Skrainka, J. A.; Esterhuizen, J. A.; Popov, D. A.; Marinescu, S. C., Surface-Immobilized Conjugated Polymers Incorporating Rhenium Bipyridine Motifs for Electrocatalytic and Photocatalytic CO2 Reduction. *ACS Appl. Energy Mater.* **2019,** *2* (1), 110-123.

44. Allara, D. L.; Nuzzo, R. G., Spontaneously organized molecular assemblies. 1. Formation, dynamics, and physical properties of n-alkanoic acids adsorbed from solution on an oxidized aluminum surface. *Langmuir* **1985,** *1* (1), 45-52.

45. Allara, D. L.; Nuzzo, R. G., Spontaneously organized molecular assemblies. 2. Quantitative infrared spectroscopic determination of equilibrium structures of solution-adsorbed n-alkanoic acids on an oxidized aluminum surface. *Langmuir* **1985,** *1* (1), 52-66.

46. Gliboff, M.; Sang, L.; Knesting, K. M.; Schalnat, M. C.; Mudalige, A.; Ratcliff, E. L.; Li, H.; Sigdel, A. K.; Giordano, A. J.; Berry, J. J.; Nordlund, D.; Seidler, G. T.; Brédas, J.-L.; Marder, S. R.; Pemberton, J. E.; Ginger, D. S., Orientation of Phenylphosphonic Acid Self-Assembled Monolayers on a Transparent Conductive Oxide: A Combined NEXAFS, PM-IRRAS, and DFT Study. *Langmuir* **2013,** *29* (7), 2166-2174.

47. Sau, Y.-K.; Yi, X.-Y.; Chan, K.-W.; Lai, C.-S.; Williams, I. D.; Leung, W.-H., Insertion of nitrene and chalcogenolate groups into the Ir-C σ bond in a cyclometalated iridium(III) complex. *J. Organomet. Chem.* **2010,** *695* (9), 1399-1404.

48. Wang, F.; Schwabacher, A. W., A convenient set of bidentate pyridine ligands for combinatorial synthesis. *Tetrahedron Lett.* **1999,** *40* (26), 4779-4782.

49. Brunner, F.; Marinakis, N.; Wobill, C.; Willgert, M.; Ertl, C. D.; Kosmalski, T.; Neuburger, M.; Bozic-Weber, B.; Glatzel, T.; Constable, E. C.; Housecroft, C. E., Modular synthesis of simple cycloruthenated complexes with state-of-the-art performance in p-type DSCs. *J. Mater. Chem. C* **2016,** *4* (41), 9823-9833.

50. Wang, Q.; Day, P.; Griffiths, J.-P.; Nie, H.; Wallis, J. D., Synthetic strategies for preparing BEDT-TTF derivatives functionalised with metal ion binding groups. *New J. Chem.* **2006,** *30* (12), 1790-1800.

51. Bauer, E. B., Chiral-at-metal complexes and their catalytic applications in organic synthesis. *Chem. Soc. Rev.* **2012,** *41* (8), 3153-3167.

52. Carmona, D.; Lahoz, F. J.; Atencio, R.; Oro, L. A.; Lamata, M. P.; Viguri, F.; San José, E.; Vega, C.; Reyes, J.; Joó, F.; Kathó, Á., Trimerisation of the Cationic Fragments [(η-ring)M(Aa)]+ ((η-ring) M=(η5-C5Me5)Rh, (η5-C5Me5)Ir, (η6-p-MeC6H4iPr)Ru; Aa=α-amino acidate) with Chiral Self-Recognition: Synthesis, Characterisation, Solution Studies and Catalytic Reactions of the Trimers [{(η-ring)M(Aa)}3](BF4)3. *Chem. Eur. J.* **1999,** *5* (5), 1544-1564.

53. Sau, Y.-K.; Yi, X.-Y.; Chan, K.-W.; Lai, C.-S.; Williams, I. D.; Leung, W.-H., Insertion of nitrene and chalcogenolate groups into the Ir–C σ bond in a cyclometalated iridium(III) complex. *J. Organomet. Chem.* **2010,** *695* (9), 1399-1404.

54. Bhattacharyya, D.; Videla, P. E.; Cattaneo, M.; Batista, V. S.; Lian, T.; Kubiak, C. P., Vibrational Stark shift spectroscopy of catalysts under the influence of electric fields at electrode–solution interfaces. *Chem. Sci.* **2021,** *12* (30), 10131-10149.

55. Clark, M. L.; Rudshteyn, B.; Ge, A.; Chabolla, S. A.; Machan, C. W.; Psciuk, B. T.; Song, J.; Canzi, G.; Lian, T.; Batista, V. S.; Kubiak, C. P., Orientation of Cyano-Substituted Bipyridine Re(I) fac-Tricarbonyl Electrocatalysts Bound to Conducting Au Surfaces. *J. Phys. Chem. C* **2016,** *120* (3), 1657-1665.

56. Cattaneo, M.; Guo, F.; Kelly, H. R.; Videla, P. E.; Kiefer, L.; Gebre, S.; Ge, A.; Liu, Q.; Wu, S.; Lian, T.; Batista, V. S., Robust Binding of Disulfide-Substituted Rhenium Bipyridyl Complexes for CO2 Reduction on Gold Electrodes. *Frontiers in Chemistry* **2020,** *8*.

57. Frisch, M. J.; Trucks, G. W.; Schlegel, H. B.; Scuseria, G. E.; Robb, M. A.; Cheeseman, J. R.; Scalmani, G.; Barone, V.; Petersson, G. A.; Nakatsuji, H.; Li, X.; Caricato, M.; Marenich, A. V.; Bloino, J.; Janesko, B. G.; Gomperts, R.; Mennucci, B.; Hratchian, H. P.; Ortiz, J. V.; Izmaylov, A. F.; Sonnenberg, J. L.; Williams; Ding, F.; Lipparini, F.; Egidi, F.; Goings, J.; Peng, B.; Petrone, A.; Henderson, T.; Ranasinghe, D.; Zakrzewski, V. G.; Gao, J.; Rega, N.; Zheng, G.; Liang, W.; Hada, M.; Ehara, M.; Toyota, K.; Fukuda, R.; Hasegawa, J.; Ishida, M.; Nakajima, T.; Honda, Y.; Kitao, O.; Nakai, H.; Vreven, T.; Throssell, K.; Montgomery Jr., J. A.; Peralta, J. E.; Ogliaro, F.; Bearpark, M. J.; Heyd, J. J.; Brothers, E. N.; Kudin, K. N.; Staroverov, V. N.; Keith, T. A.; Kobayashi, R.; Normand, J.; Raghavachari, K.; Rendell, A. P.; Burant, J. C.; Iyengar, S. S.; Tomasi, J.; Cossi, M.; Millam, J. M.; Klene, M.; Adamo, C.; Cammi, R.; Ochterski, J. W.; Martin, R. L.; Morokuma, K.; Farkas, O.; Foresman, J. B.; Fox, D. J. *Gaussian 16 Rev. C.01*, Wallingford, CT, 2016.

58. Chai, J.-D.; Head-Gordon, M., Long-range corrected hybrid density functionals with damped atom–atom dispersion corrections. *PCCP* **2008,** *10* (44), 6615-6620.

59. Hehre, W. J.; Ditchfield, R.; Pople, J. A., Self—Consistent Molecular Orbital Methods. XII. Further Extensions of Gaussian—Type Basis Sets for Use in Molecular Orbital Studies of Organic Molecules. *J. Chem. Phys.* **1972,** *56* (5), 2257-2261.

60. Hariharan, P. C.; Pople, J. A., The influence of polarization functions on molecular orbital hydrogenation energies. *Theor. Chim. Acta* **1973,** *28* (3), 213-222.

61. Francl, M. M.; Pietro, W. J.; Hehre, W. J.; Binkley, J. S.; Gordon, M. S.; DeFrees, D. J.; Pople, J. A., Self-consistent molecular orbital methods. XXIII. A polarization-type basis set for second-row elements. *J. Chem. Phys.* **1982,** *77* (7), 3654-3665.

62. Weigend, F., Accurate Coulomb-fitting basis sets for H to Rn. *PCCP* **2006,** *8* (9), 1057-1065.

63. Hansen, W. N., Electric Fields Produced by the Propagation of Plane Coherent Electromagnetic Radiation in a Stratified Medium. *Journal of the Optical Society of America* **1968,** *58* (3), 380-390.

64. McIntyre, J. D. E.; Aspnes, D. E., Differential reflection spectroscopy of very thin surface films. *Surf. Sci.* **1971,** *24* (2), 417-434.

65. Amberger, H.-D.; Reddmann, H., Electronic structures of organometallic complexes of f elements LXXIV: First Raman spectroscopic polarization measurements on uniformly oriented sandwich complex molecules: Bis(η5-pentamethylcyclopentadienyl)ruthenium. *J. Organomet. Chem.* **2010,** *695* (22), 2455-2460.

66. Bencze, É.; Lokshin, B. V.; Mink, J.; Herrmann, W. A.; Kühn, F. E., Vibrational spectra and structure of the cyclopentadienyl-anion (Cp−), the pentamethylcyclopentadienyl-anion (Cp*−) and of alkali metal cyclopentadienyls CpM and Cp*M (M=Li, Na, K). *J. Organomet. Chem.* **2001,** *627* (1), 55-66.

67. Nejman, P. S.; Morton-Fernandez, B.; Moulding, D. J.; Athukorala Arachchige, K. S.; Cordes, D. B.; Slawin, A. M. Z.; Kilian, P.; Woollins, J. D., Structural diversity of bimetallic rhodium and iridium half sandwich dithiolato complexes. *Dalton Trans.* **2015,** *44* (38), 16758-16766.

68. Barner, B. J.; Green, M. J.; Saez, E. I.; Corn, R. M., Polarization modulation Fourier transform infrared reflectance measurements of thin films and monolayers at metal surfaces utilizing real-time sampling electronics. *Anal. Chem.* **1991,** *63* (1), 55-60.

69. Buffeteau, T.; Desbat, B.; Blaudez, D.; Turlet, J. M., Calibration Procedure to Derive IRRAS Spectra from PM-IRRAS Spectra. *Appl. Spectrosc.* **2000,** *54* (11), 1646-1650.

70. Sheldrick, G., A short history of SHELX. *Acta Cryst. A* **2008,** *64* (1), 112-122.

71. Dolomanov, O. V.; Bourhis, L. J.; Gildea, R. J.; Howard, J. A. K.; Puschmann, H., OLEX2: a complete structure solution, refinement and analysis program. *J. Appl. Crystallogr.* **2009,** *42* (2), 339-341.

72. Allara, D. L.; Baca, A.; Pryde, C. A., Distortions of Band Shapes in External Reflection Infrared Spectra of Thin Polymer Films on Metal Substrates. *Macromolecules* **1978,** *11* (6), 1215-1220.

73. Sang, L.; Mudalige, A.; Sigdel, A. K.; Giordano, A. J.; Marder, S. R.; Berry, J. J.; Pemberton, J. E., PM-IRRAS Determination of Molecular Orientation of Phosphonic Acid Self-Assembled Monolayers on Indium Zinc Oxide. *Langmuir* **2015,** *31* (20), 5603-5613.

74. Wang, H. Interfacial and Solution Characterization of Rhamnolipid Biosurfactants and their Synthetic Analogues. The University of Arizona., 2011.

75. Sheik, D. A.; Chamberlain, J. M.; Brooks, L.; Clark, M.; Kim, Y. H.; Leriche, G.; Kubiak, C. P.; Dewhurst, S.; Yang, J., Hydrophobic Nanoparticles Reduce the β-Sheet Content of SEVI Amyloid Fibrils and Inhibit SEVI-Enhanced HIV Infectivity. *Langmuir* **2017,** *33* (10), 2596-2602.

76. Baker, C.; Cockerill, I. P.; Kelsey, J. E.; Maddams, W. F., The characterization of infrared absorption band shapes. I. Methods. *Spectrochimica Acta Part A: Molecular Spectroscopy* **1978,** *34* (7), 673-682.

77. Baker, C.; Johnson, P. S.; Maddams, W. F., The characterization of infrared absorption band shapes. II. Experimental studies. *Spectrochimica Acta Part A: Molecular Spectroscopy* **1978,** *34* (7), 683-691.

78. Perdew, J. P.; Burke, K.; Ernzerhof, M., Generalized Gradient Approximation Made Simple. *Phys. Rev. Lett.* **1996,** *77* (18), 3865-3868.

79. Grimme, S.; Ehrlich, S.; Goerigk, L., Effect of the damping function in dispersion corrected density functional theory. *J. Comput. Chem.* **2011,** *32* (7), 1456-1465.

80. Kepp, K. P., Benchmarking Density Functionals for Chemical Bonds of Gold. *The Journal of Physical Chemistry A* **2017,** *121* (9), 2022-2034.

81. Hay, P. J.; Wadt, W. R., Ab initio effective core potentials for molecular calculations. Potentials for K to Au including the outermost core orbitals. *J. Chem. Phys.* **1985,** *82* (1), 299-310.

4.7 Appendix

4.7.1 Molar Absorptivity and Refractive Index of C1 and C2

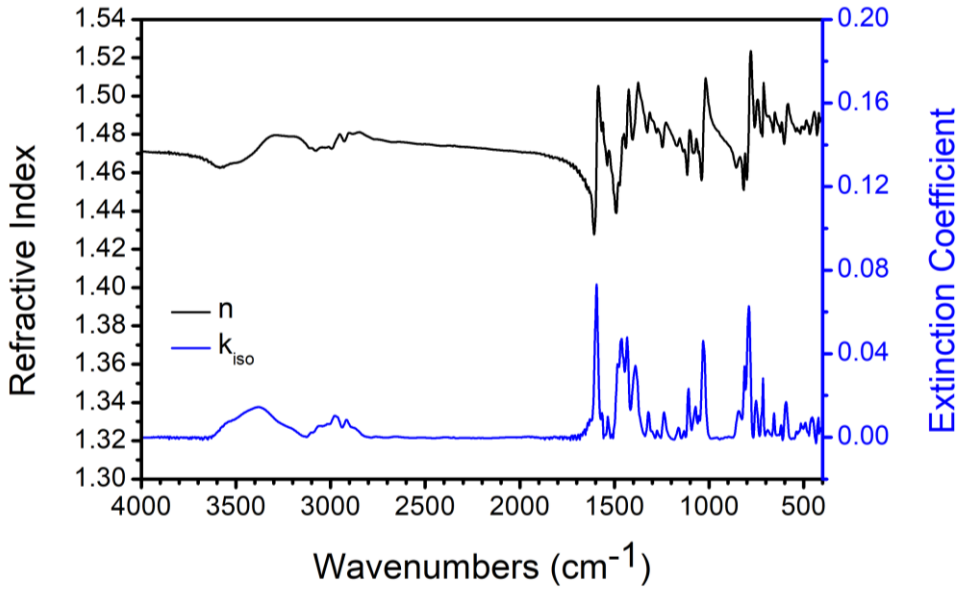

Figure 4.15. Extinction coefficient, k_{iso}, of C1 obtained from IR-transmission spectroscopy. Refractive index, n, of C1 obtained from the Kramers-Kronig transformation of k.

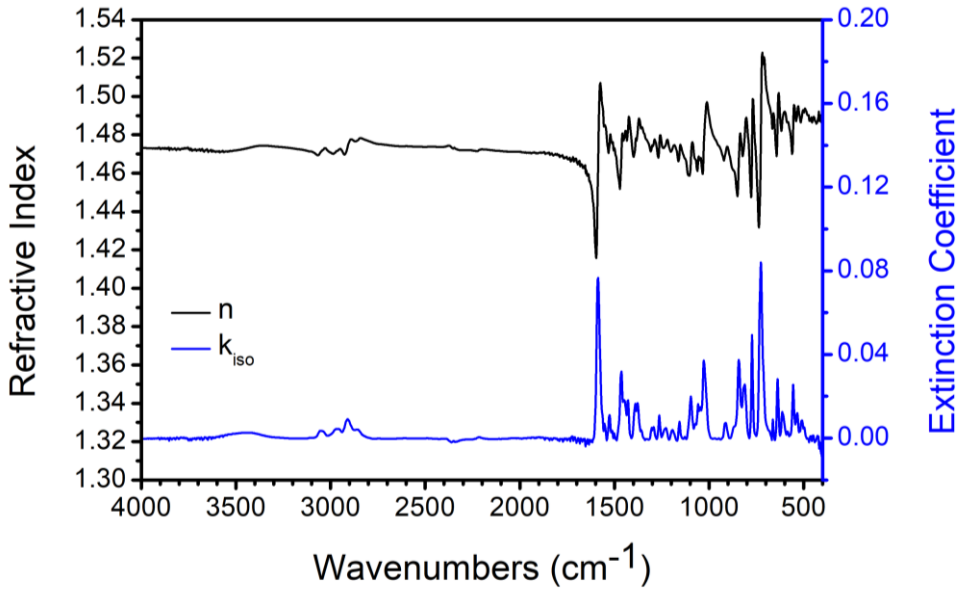

Figure 4.14. Extinction coefficient, k_{iso}, of C2 obtained from IR-transmission spectroscopy. Refractive index, n, of C2 obtained from the Kramers-Kronig transformation of k.

4.7.2 PM-IRRAS 4000-400 cm^{-1}

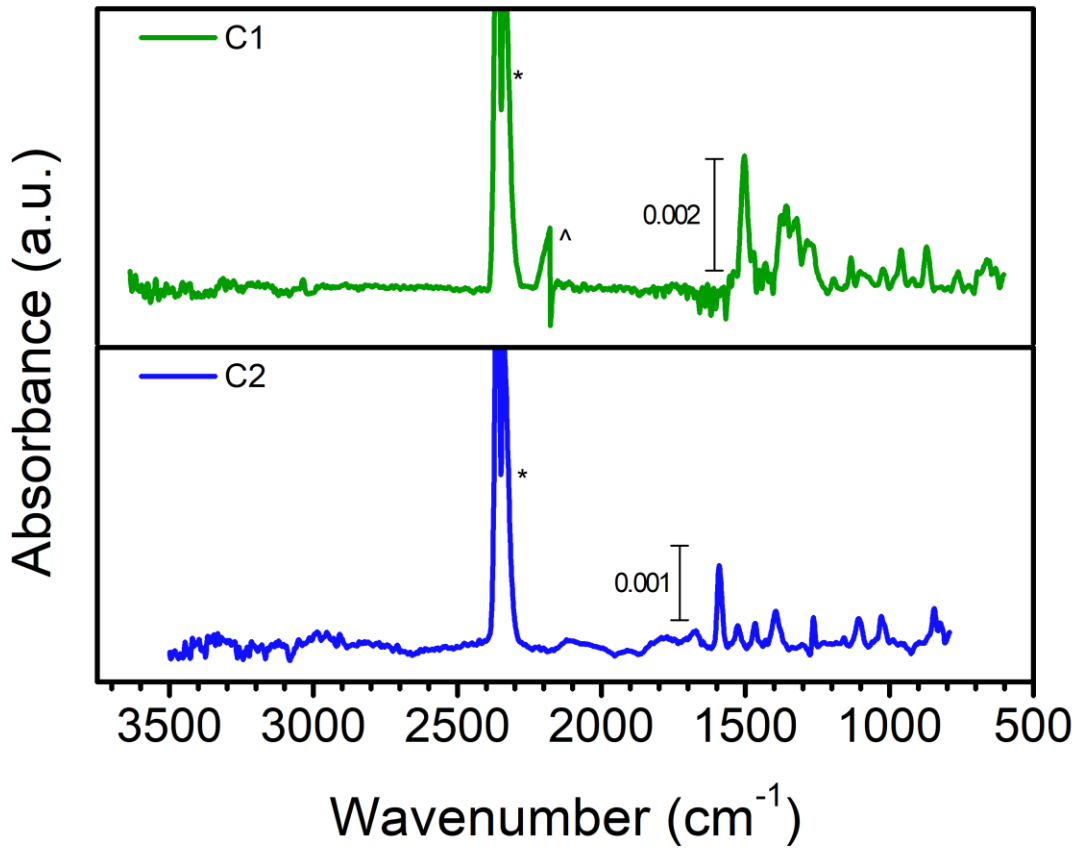

Figure 4.16. PM-IRRAS of C1 (green) and C2 (blue) on Au. Figure is combined spectra taken with maximum dephasing at 3000 cm^{-1} and 1600 cm^{-1} to minimize PM error across the entire spectra. * indicates atmospheric CO_2 and ^ is where the two spectra are combined.

4.7.3 PM-IRRAS and Simulated IRRAS Fitting

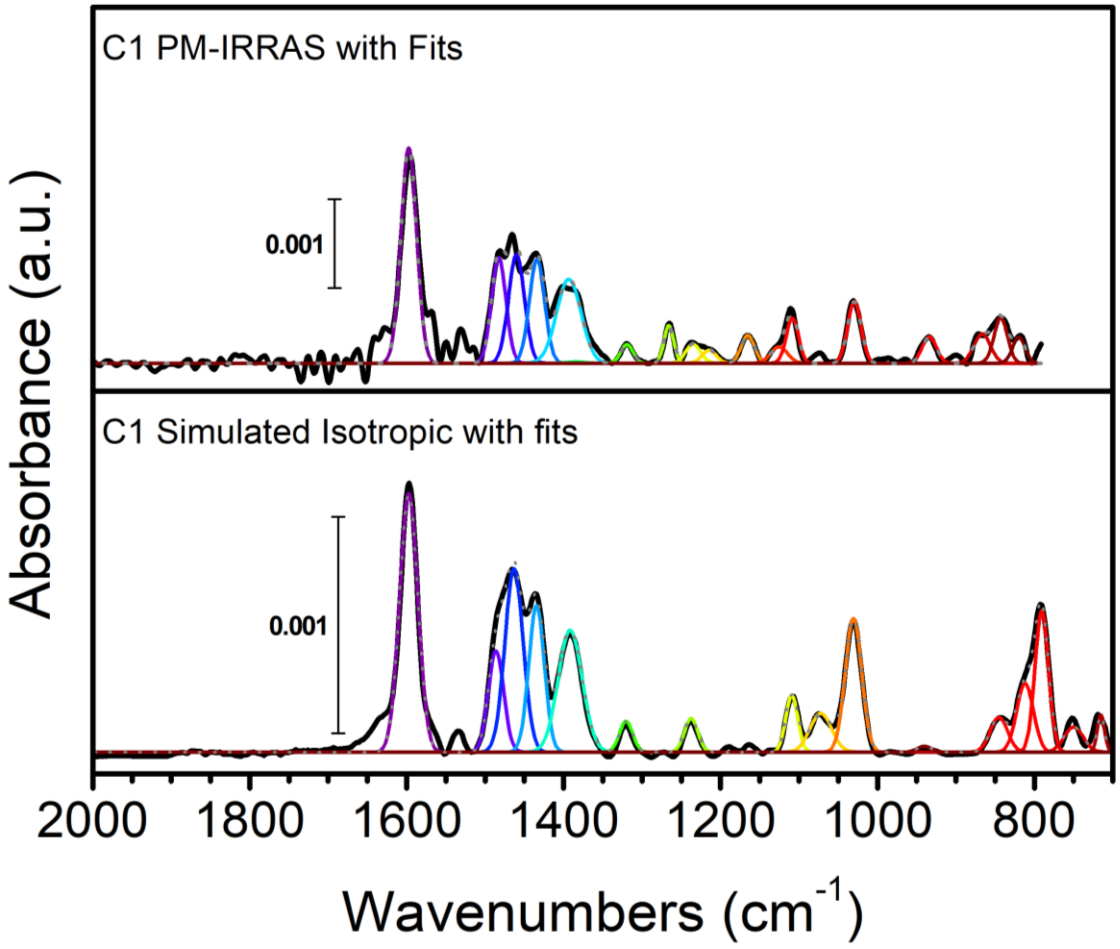

Figure 4.17. PM-IRRA (top) and simulated IRRA (bottom) spectra with fits of a monolayer made from C1. The PM-IRRA spectrum is fit with Gaussian line shapes and the simulated IRRA spectrum is fit with a combination of Lorentzian and Gaussian line shapes.

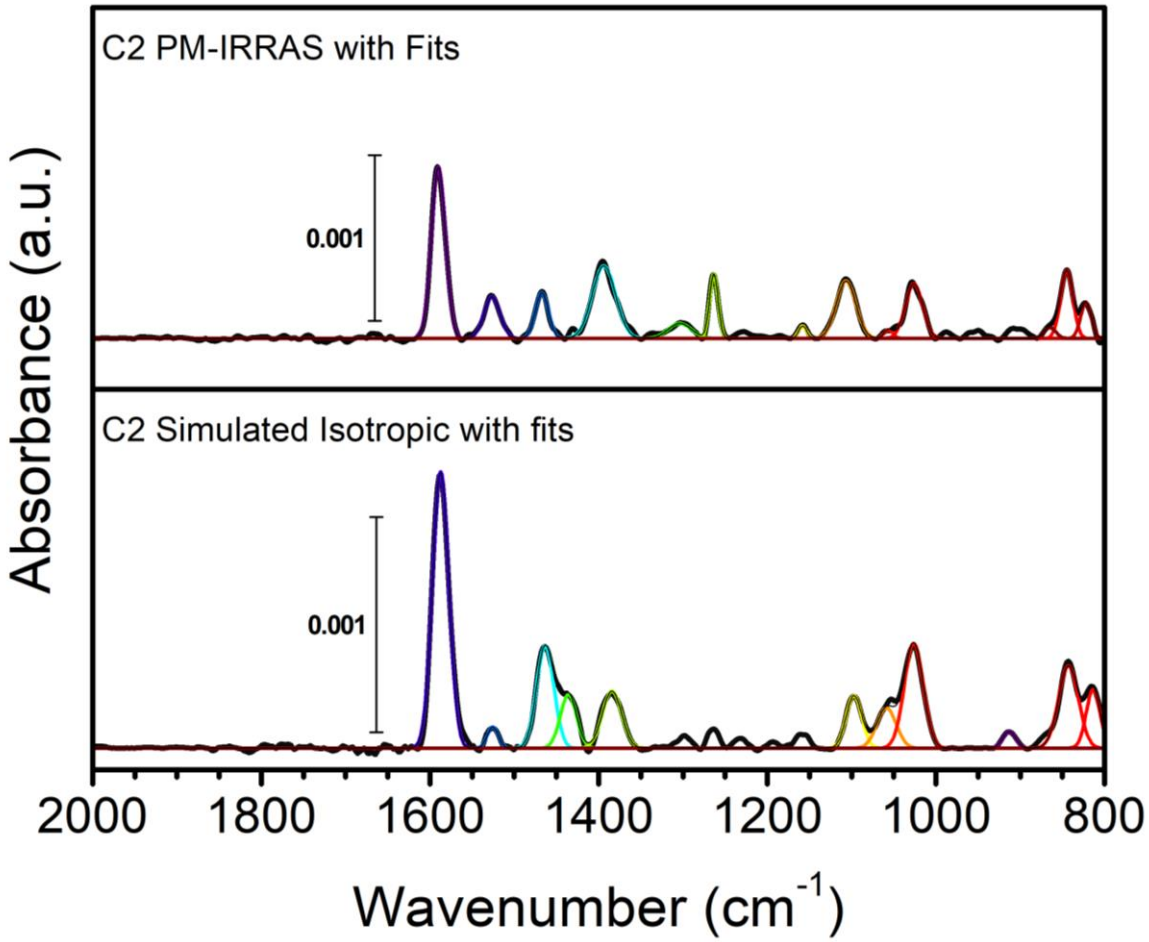

Figure 4.18. PM-IRRA (top) and simulated IRRA (bottom) spectra with fits of a monolayer made from C2 on Au. The PM-IRRA spectrum is fit with Gaussian line shapes and the simulated IRRA spectrum is fit with a combination of Lorentzian and Gaussian line shapes.

4.7.4 DFT Computed FTIR

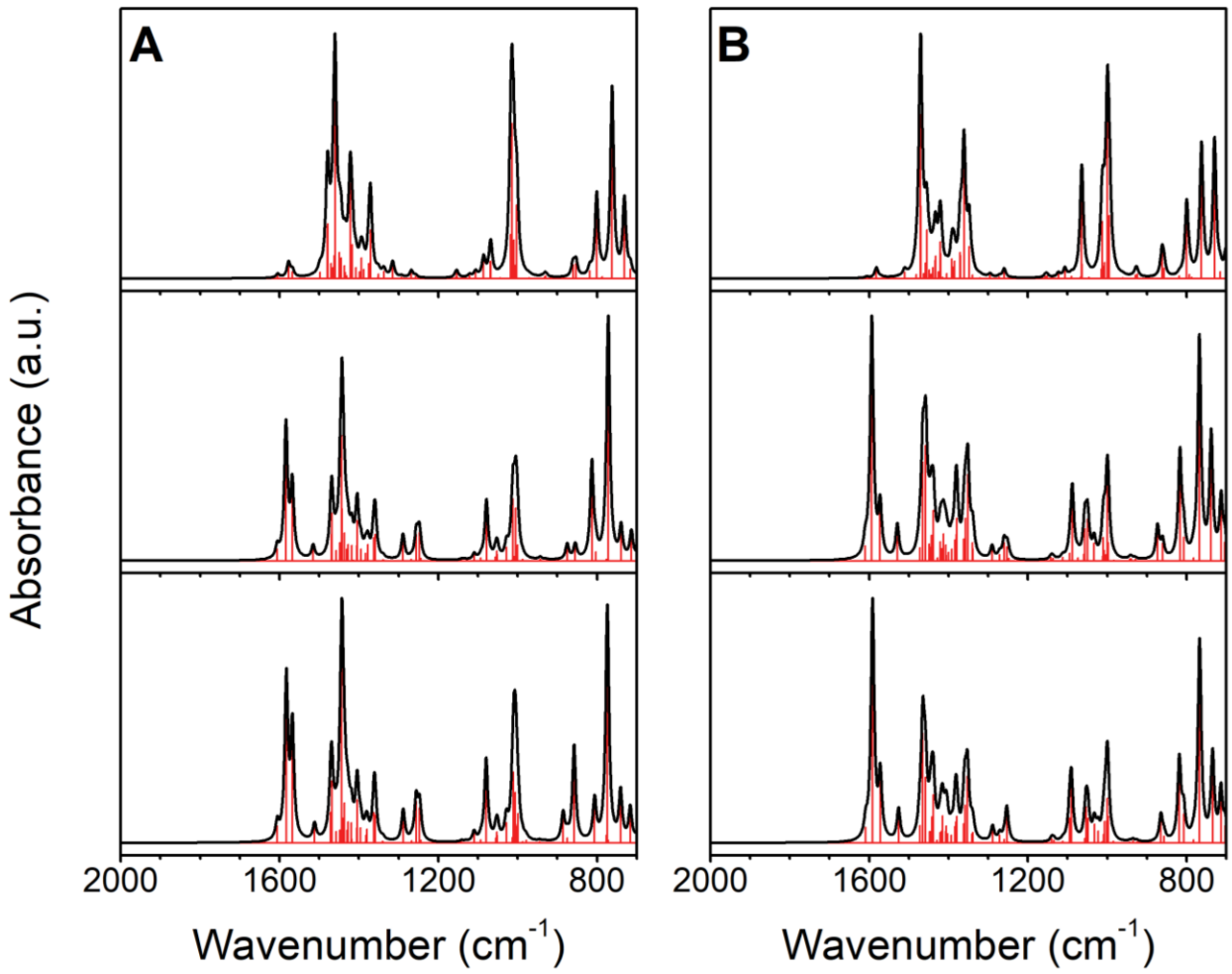

Figure 4.19. DFT calculated FTIR spectra of **C1** attached to Au in **A** the Cl down orientation using (Original Basis) (top), LAN (middle), and DEF (bottom) and **B** Cl up orientation using (Original Basis) (top), LAN (middle), and DEF (bottom).

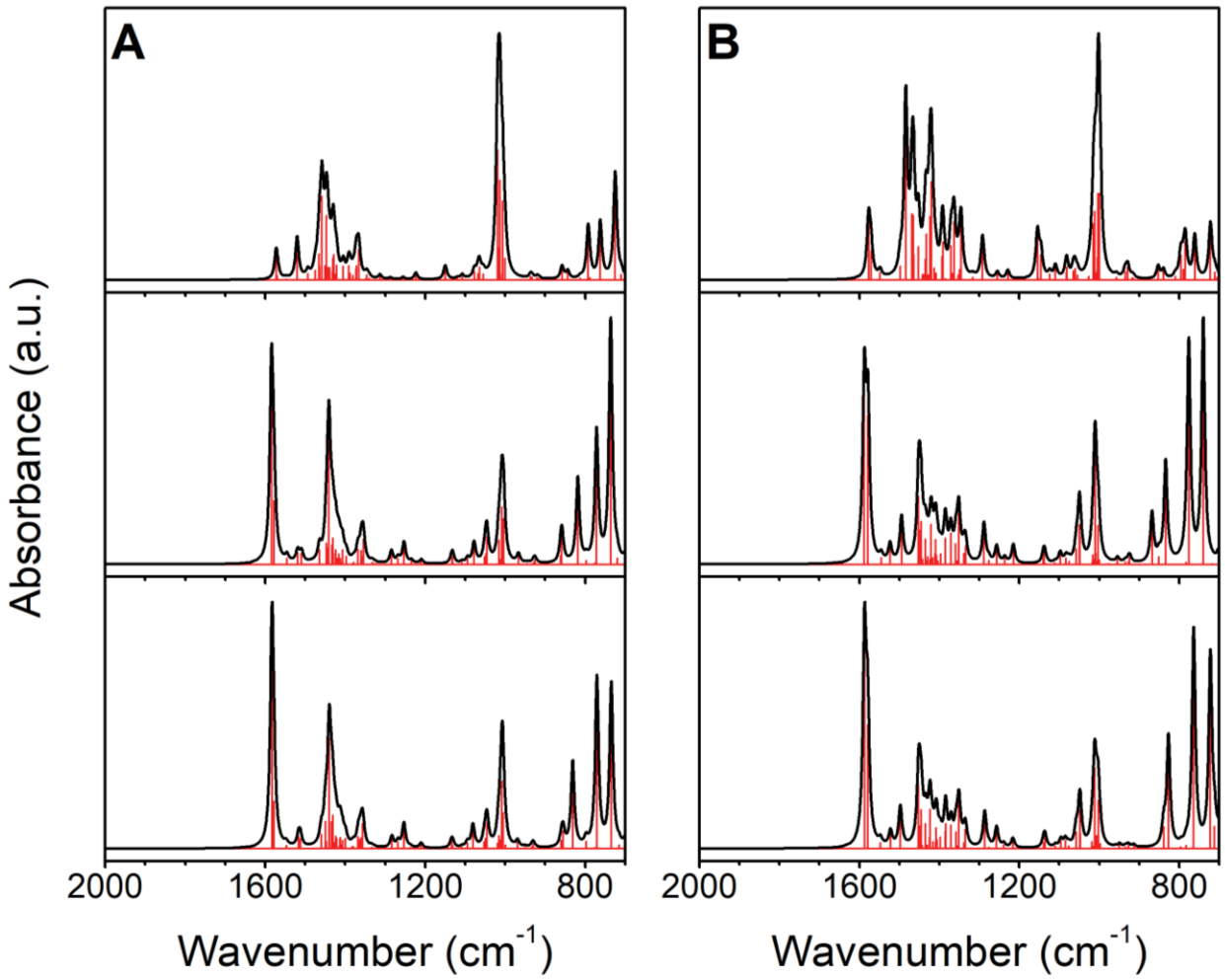

Figure 4.20. DFT calculated FTIR spectra of C2 attached to Au in **A** the Cl down orientation using (Original Basis) (top), LAN (middle), and DEF (bottom) and **B** Cl up orientation using (Original Basis) (top), LAN (middle), and DEF (bottom).

4.7.5 Visualizations of Select IR Modes

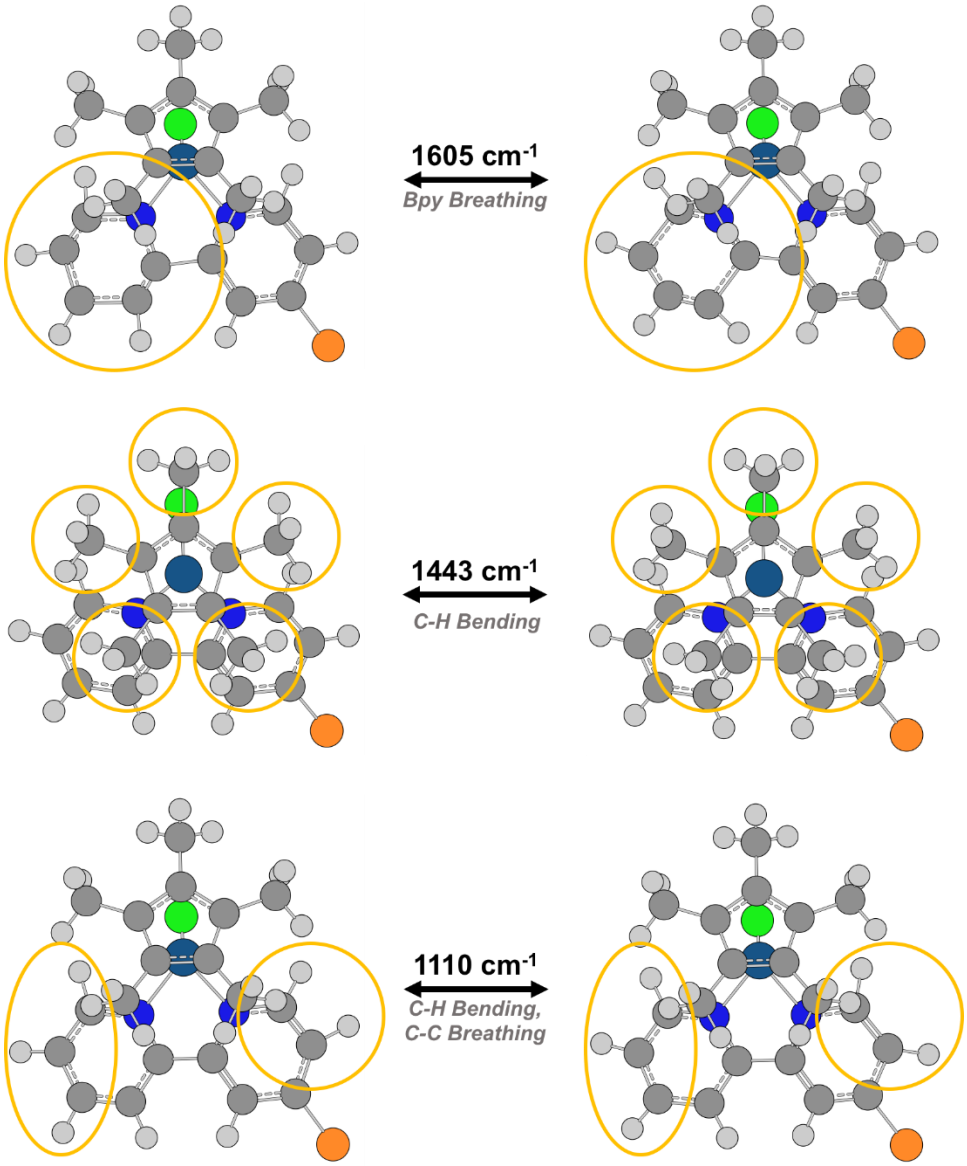

Figure 4.21. Visualization of displacements along key normal modes for **C1m** in the Cl down orientation (wB97XD functional and the DEF2SVP basis set with a 0.9485 scaling factor). Each mode is labeled with the corresponding vibrational frequency and a description; orange circles and ovals are used to highlight areas of the molecule that have the largest displacements. All normal modes are reported in **Table 4.2**. Au atoms have been removed from the molecular structures for clarity.

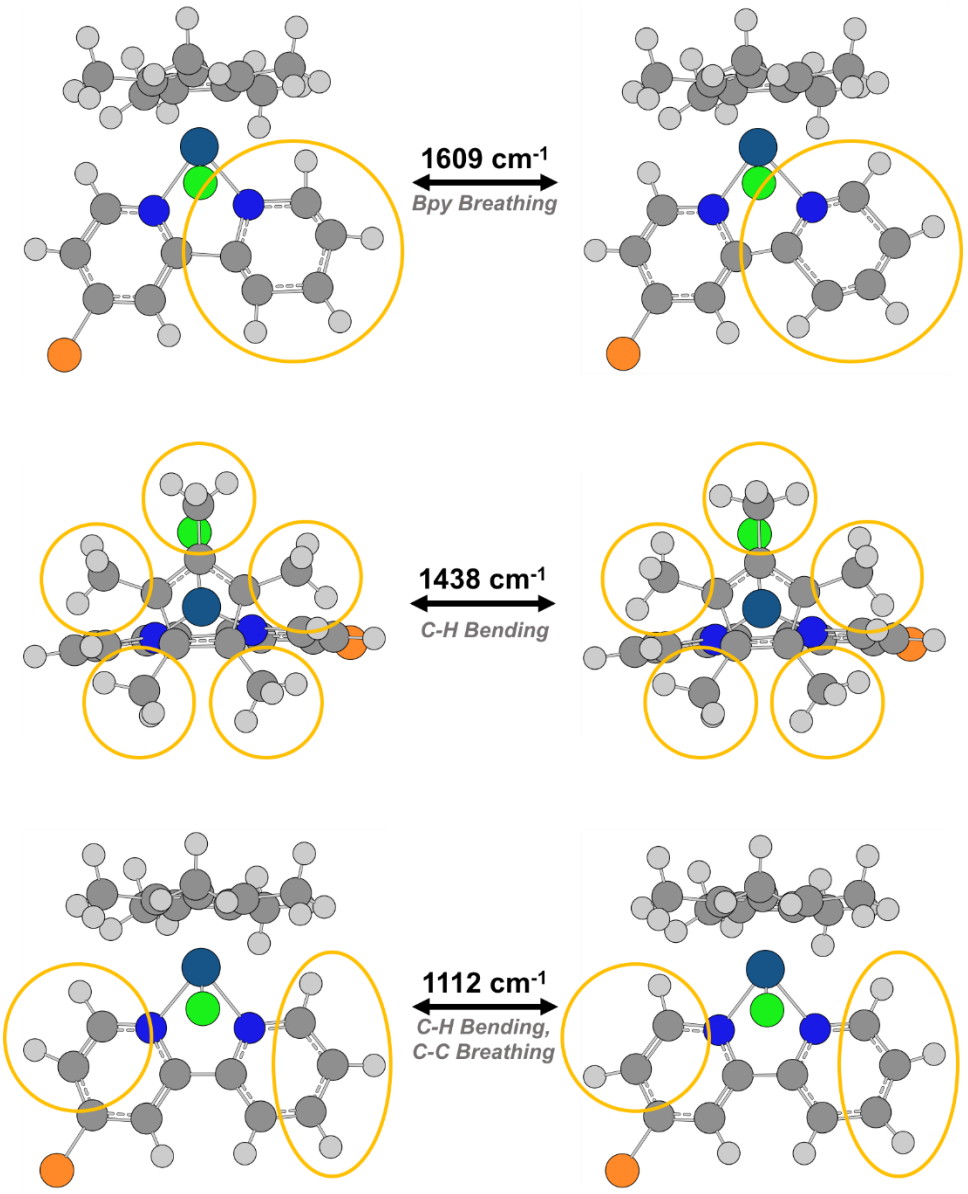

Figure 4.22. Visualization of displacements along key normal modes for **C1m** in the Cl up orientation (wB97XD functional and the DEF2SVP basis set with a 0.9485 scaling factor). Each mode is labeled with the corresponding vibrational frequency and a description; orange circles and ovals are used to highlight areas of the molecule that have the largest displacements. All normal modes are reported in **Table 4.2.** Au atoms have been removed from the molecular structures for clarity.

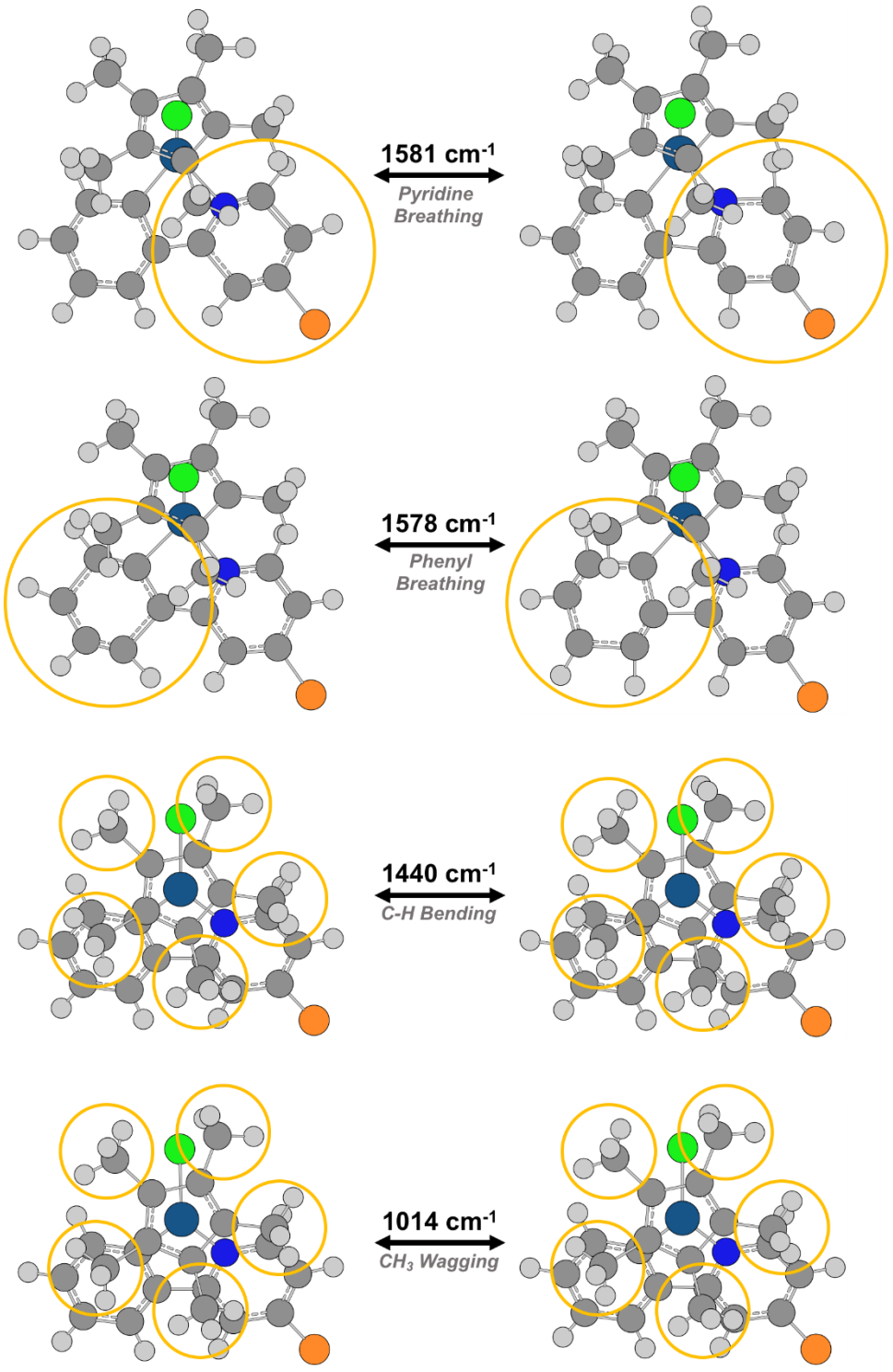

Figure 4.23. Visualization of displacements along key normal modes for **C2m** in the Cl down orientation (wB97XD functional and the DEF2SVP basis set with a 0.9485 scaling factor). Each mode is labeled with the corresponding vibrational frequency and a description; yellow circles are used to highlight areas of the molecule that have the largest displacements. All normal modes are reported in **Table 4.3**. Au atoms have been removed from the molecular structures for clarity.

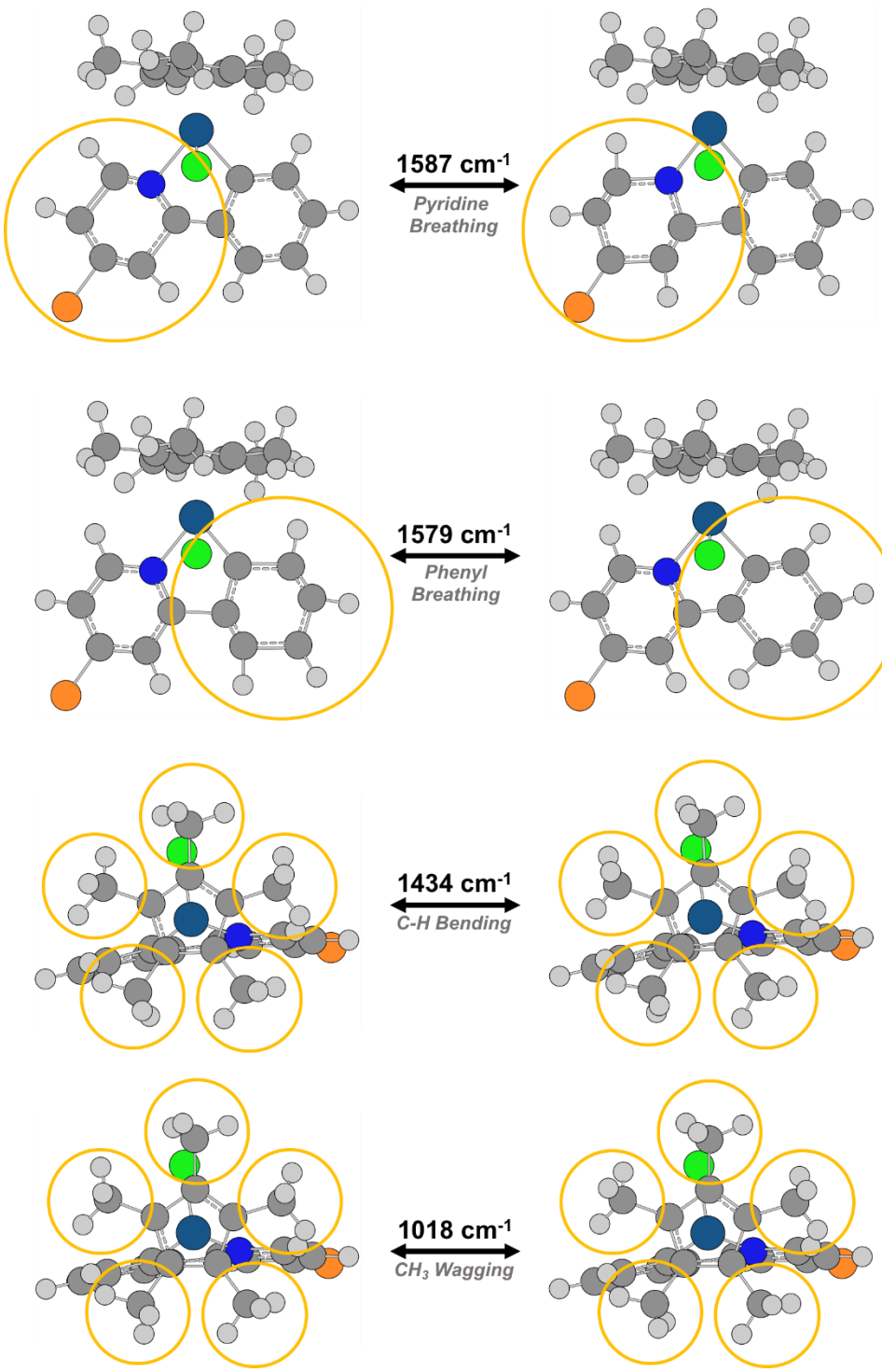

Figure 4.24. Visualization of displacements along key normal modes for **C2m** in the Cl up orientation (wB97XD functional and the DEF2SVP basis set with a 0.9485 scaling factor). Each mode is labeled with the corresponding vibrational frequency and a description; yellow circles are used to highlight areas of the molecule that have the largest displacements. All normal modes are reported in **Table 4.3**. Au atoms have been removed from the molecular structures for clarity.

4.7.6 Crystallographic Data

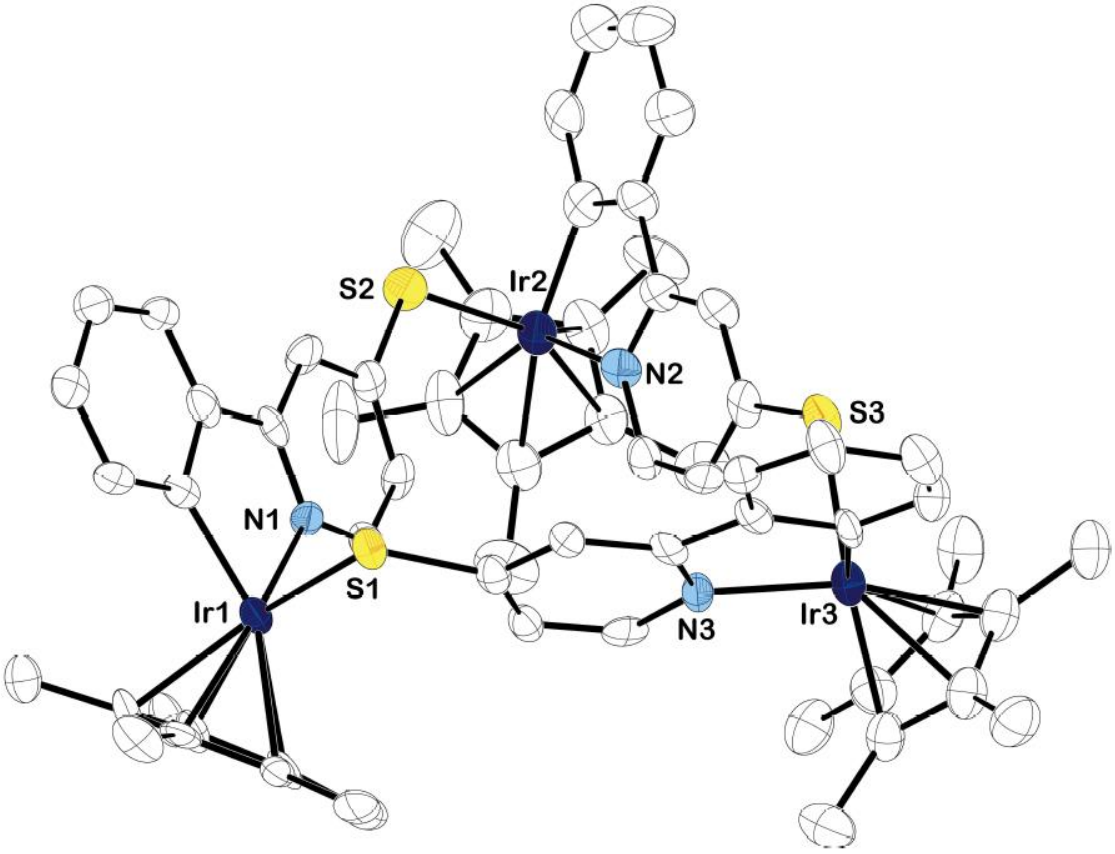

Figure 4.25. Solid-state structure of [Cp*Ir(2-phenylpyridine-4-thiol)]$_3$ (**C3**) as determined by single-crystal X-ray diffraction. Thermal ellipsoids are set at the 50% probability level. Non-coordinating ortho-dichlorobenzene molecules and carbon bound hydrogens were omitted for clarity.

Table 4.4. Crystal data and structure refinement for complex **C3**

Empirical Formula	$C_{85.66}H_{81.11}Cl_{7.46}Ir_3N_3S_3$
Formula weight	2089.84
Temperature/K	100.0
Crystal system	monoclinic
Space group	C2/c
a/Å	45.563(8)
b/Å	18.693(3)
c/Å	21.023(4)
α/°	90
β/°	90.978(4)
γ/°	90
Volume/ $Å^3$	17902(5)
Z	8
ρcalcg/cm^3	1.551
μ/mm 1	4.784
F(000)	8175.0
Crystal size/mm3	0.3 × 0.1 × 0.1
Radiation	MoKα (λ = 0.71073)
2θ range for data collection/°	3.04 to 48.828
Index Ranges	$-52 \leq h \leq 52$, $-21 \leq k \leq 21$, $-24 \leq l \leq 24$
Reflections Collected	104645
Independent reflections	14729 [Rint = 0.1623, Rsigma = 0.1008]
Data/restraints/parameters	14729/72/955
Goodness-of-fit on F2	1.027
Final R indexes [I>=2s (I)]	$R_1 = 0.0491$, $wR_2 = 0.1018$
Final R indexes [all data]	$R_1 = 0.0910$, $wR_2 = 0.116$
Largest diff. peak/hole / e Å -3	2.33/-1.19

4.7.7 X-ray Photoelectron Spectroscopy

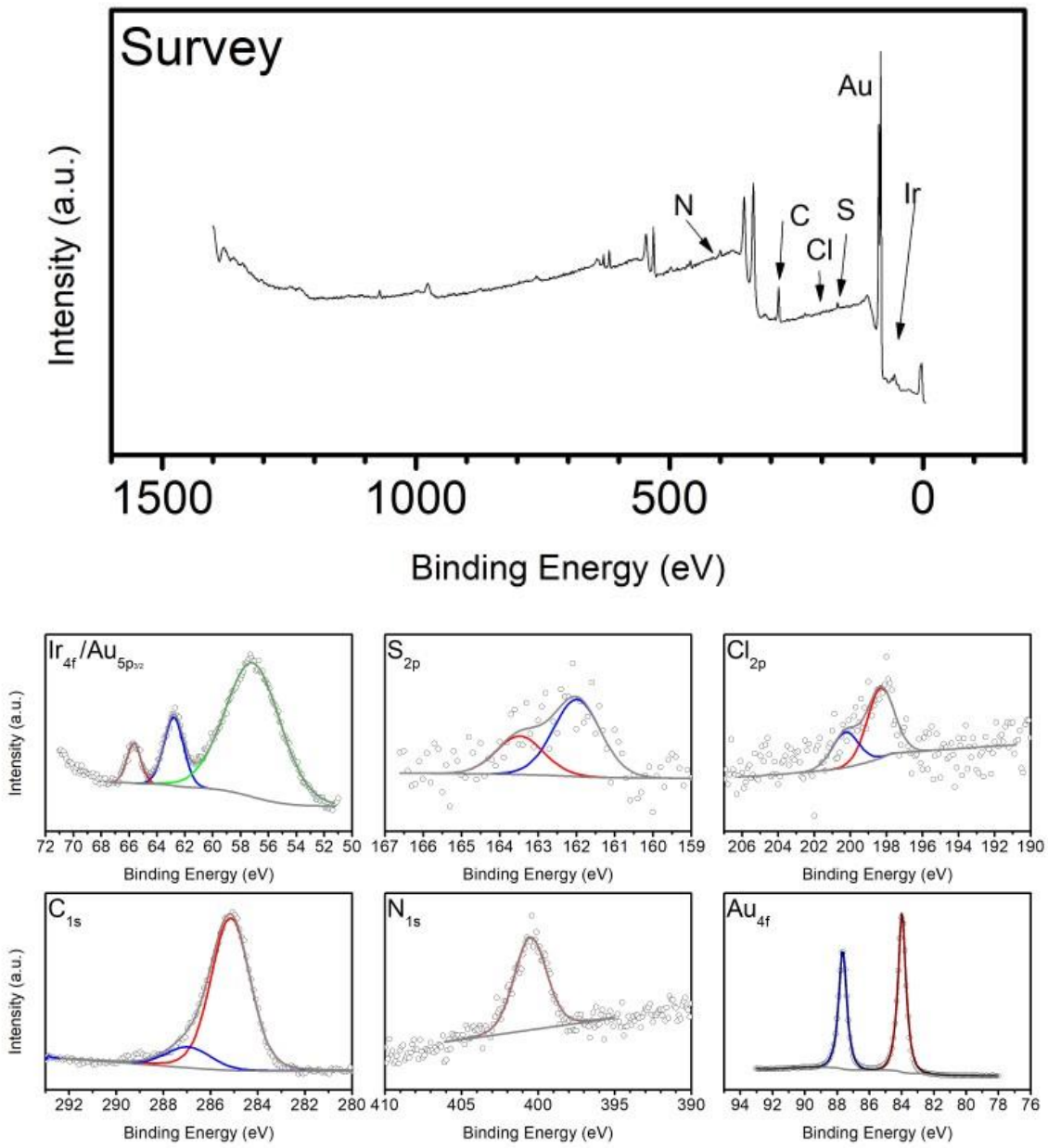

Figure 4.26. Survey (top) and high-resolution XPS of the C1m monolayer on Au. XPS peak positions of relevant elements (in eV) Ir (65.6, 62.7) S (163.5, 162.0), Cl (200.3, 198.3).

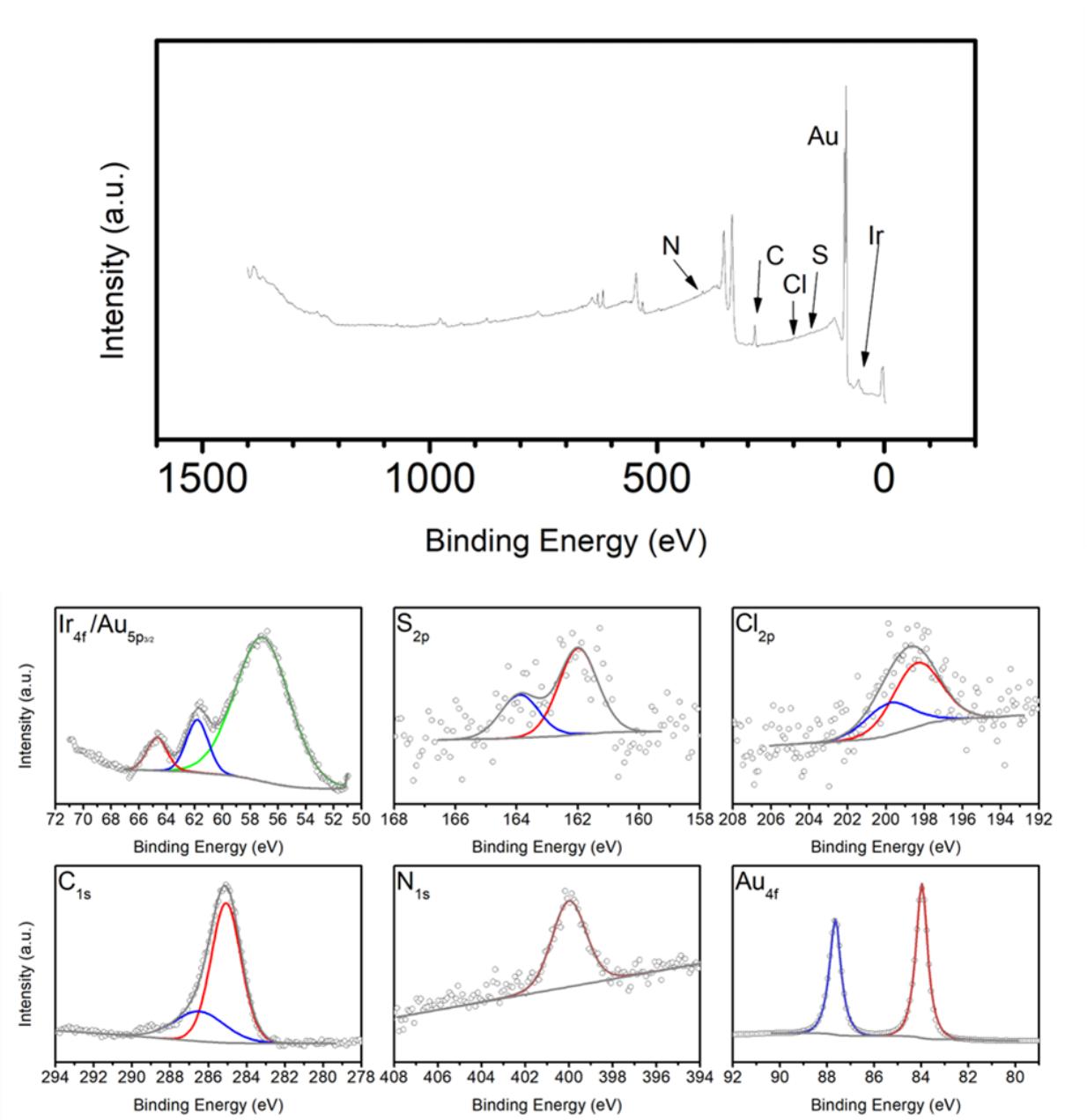

Figure 4.27. Survey (top) and high-resolution XPS of the C2m monolayer on Au. XPS peak positions of relevant elements (in eV) Ir (64.7, 61.8) S (163.9, 162.0), Cl (199.9, 198.4).

4.7.8 Quantification of Cl and Ir for C1m

ELEMENT	PEAK	% CONCENTRATION	RATIO
Ir	$4f_{7/2}$	19.82	1 Ir : 2.55 Cl
Ir	$4f_{5/2}$	8.27	
Cl	$2p_{3/2}$	47.94	
Cl	$2p_{1/2}$	23.96	

The peaks of the high-resolution Ir 4f spectra for both C1m and C2m correspond to Ir being in the 3+ state. While there is overlap from Au 5d, there appears to be no lower energy Ir 4f signals, indicating that Ir is only in the 3+ state and there is no Ir 1+. Using the fitting analysis in CasaXPS and correcting for the relative sensitivity factors for each element, it was determined that there is about 1 Ir atom per 2.55 Cl. This demonstrates that there the C1m monolayer co-packs with the Cl anion to balance the charges on the surface.

4.7.9 Reported Densities of Ir piano-stool complexes

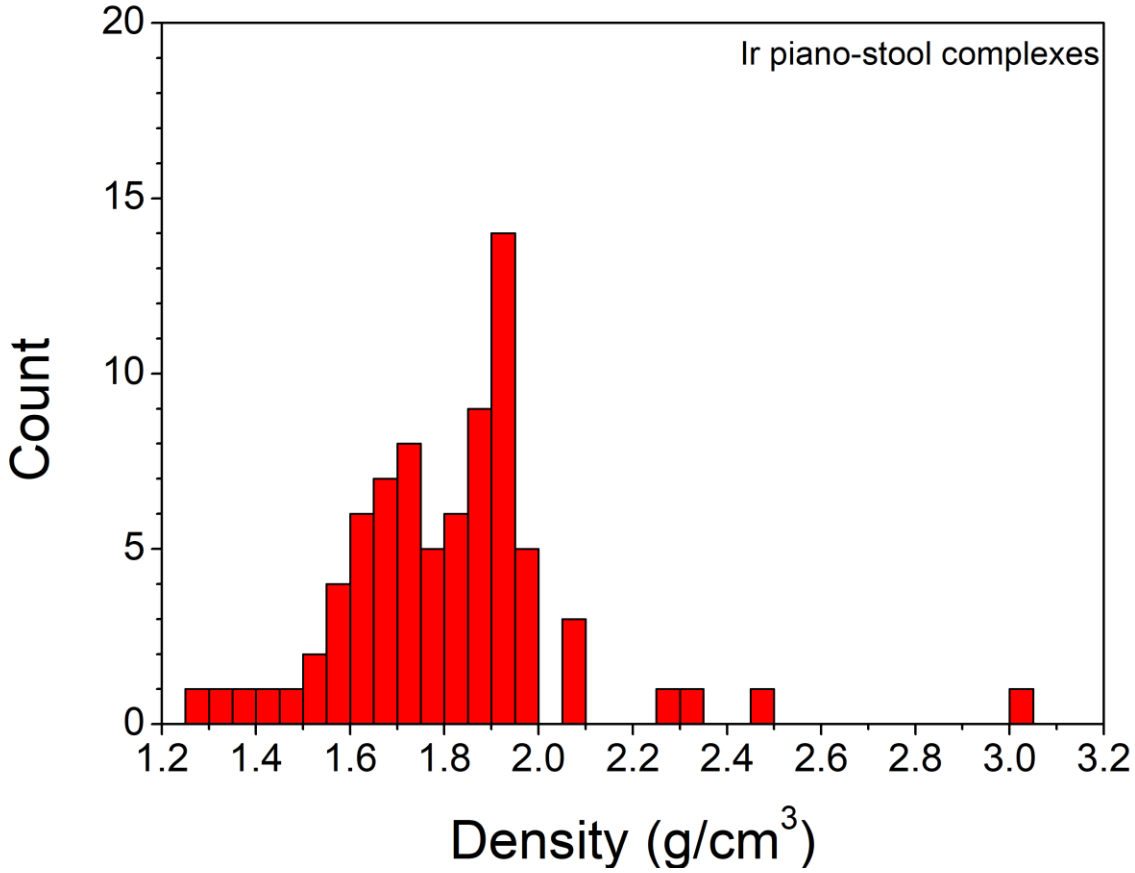

Figure 4.28 Histogram showing the reported density of Ir piano-stool complexes containing a halide and either a bipyridine or phenylpyridine moiety deposited in the Cambridge Structural Database (78 structures).